THE UNIVERSITY *of* EDINBURGH

Instrumentation development for magneto-transport and neutron scattering measurements at high pressure and low temperature

Weiwei Wang

For the degree of Doctor of Philosophy

School of Engineering

University of Edinburgh

2012

Declaration

This work described in this thesis was carried out at the School of Engineering and Centre for Science at Extreme Conditions (CSEC), the University of Edinburgh during the period September 2007 to September 2011. This thesis represents the author's original work, except where otherwise stated, and no part of it has been submitted for a degree at any other university. Prior to the submission of this thesis, some work has been published as described in the relevant chapters herein.

Weiwei Wang

Acknowledgements

Firstly, I would like to express my deepest gratitude and respect to my supervisor, Dr.Konstantin Kamenev for his outstanding guidance, constant support, encouragement and extraordinary patience in the pass four and half years. I am also very grateful to Professor Andrew Huxley who gave me guidance and support at all the stages of my research.

I wish to express my thanks to all the members in the quantum ordering group. In particular, I would like to thank Alex Holmes and Marie-Aude Méasson for introducing me to the high-pressure resistivity measurements, thank Dmitry Sokolov for growing single crystals and teaching me some relevant physics, and thank Edward Yelland for testing the two-axis rotating stage at the University of St Andrews. Big thanks are given to Andrew Downie and Paul Aitken from Physics and Engineering workshops for machining all the components of my design.

Finally, I would like to thank Minghui Yang and Junwei Fang for their friendship. I would also like to thank my family for their great confidence in me and constant support through all these years.

Abstract

High pressure, high magnetic field and low temperature techniques are required to investigate magnetic transitions and quantum critical behaviour in different ferromagnetic materials to elucidate how novel forms of superconductivity and other new states are brought about. In this project, several instruments for magneto-transport and neutron scattering measurements have been designed and built. They include inserts for a dilution refrigerator and pressure cells for resistivity, magnetic susceptibility and inelastic neutron scattering measurements. The technical drawings of the low temperature inserts and pressure cells were produced with Solid Edge computer-aided software and the performance and safety assessments were evaluated with the ANSYS finite element analysis package. The pressure cells developed include diamond anvil cells, piston cylinder cells and some auxiliary equipment. Pressure effects on the physical properties such as the electrical resistivity and magnetic ordering of some ferromagnetic materials were studied with the equipment developed.

A two-axis rotating stage was developed and deployed with a dilution refrigerator combined within a superconducting magnet to measure various physical properties as a function of the orientation of the sample with respect to applied field at sub-Kelvin temperature. The rotating stage is made of Beryllium Copper (BeCu) alloy. In order to avoid the entanglement of the wires, custom-designed “flexi cables” - copper tracks printed on a Kapton foil with a yield of nearly 100% - to work with the rotating stage were manufactured. The performance of the rotating stage has been demonstrated by a quantum oscillation in the electrical resistivity study of a high field ferromagnetic superconductor URhGe.

A miniature diamond anvil cell based on the turnbuckle principle has been designed.

The cell, made of BeCu alloy, is 7mm in length and 7mm in diameter. It has been shown to reach a maximum pressure of 10 GPa with diamond anvils with 800 μm culets. The small dimensions of the cell allow it to fit into the existing sample environment such as Physical Properties Measurement System (PPMS) and Magnetic Properties Measurement System (MPMS) from Quantum Design, USA, and onto the customized two-axis rotating stage built for the dilution fridge. It also thermalizes rapidly allowing rapid cooling and heating during the experiments. The cell can be used to make both resistivity and magnetic susceptibility measurements. To ensure the hydrostaticity of the pressure around the sample in the turnbuckle cell, a gearbox was designed for cryogenic loading of liquid argon and room temperature gas loading of either helium or argon at a loading pressure of up to 0.3 GPa.

Pressure effects on the Curie temperature of a PrNi ferromagnet were studied in a diamond anvil cell. Four-probe resistance measurements under pressures up to 9 GPa were carried out in a PPMS. The possibility of tuning the physical properties of the material by altering the pressures has been demonstrated. By analysing the results of the electrical resistivity measurements under pressures, it was concluded that the Curie temperature of PrNi increases with pressure at the rate of 0.85 K per GPa. The quantity $\Delta(\frac{\partial \rho}{\partial T})$ which reflects some part of the entropy change also increases with pressure. The expected quantum critical point has not been observed in this material up to 9 GPa.

A large volume high-pressure piston-cell for inelastic neutron scattering measurements has been designed and can reach a pressure of up to 1.8 GPa with a sample volume in excess of 400 mm^3. The dimension of the part of the cell exposed to the neutron beam has been optimized to minimize the attenuation of the neutron beam. The novel design of the piston seal also eliminates the use of a sample container, which makes it possible to accommodate larger samples and reduces the

absorption. The pressure in the cell is measured by a manganin pressure gauge placed next to the sample. The performance of the cell was illustrated by an inelastic neutron scattering study of UGe_2.

Table of contents

Chapter 1 Introduction

1.1 Motivation

To better understand the physics of quantum criticality, studying simple real systems where theory and experiment can be compared is desirable. Recent discovery of the new ground states that are both ferromagnetic and superconducting in UGe_2[1] and URhGe[2] occurring at accessible temperatures under the application of either magnetic field or pressure makes it possible to explore their phase diagrams encompassing the quantum critical point (QCP). The formation of new superconducting states in ferromagnets and their relationship to quantum criticality is of great importance and could shed light into many other physical systems. As the technology grows out of science, a better understanding of ferromagnetic superconductors could also allow new applications to be developed beyond those based on their very high critical fields.

The work presented in this thesis forms a part of Field Induced Quantum Ordering project funded by U.K. Engineering and Physical Sciences Research Council (EPSRC) which has the objective to establish how novel forms of superconductivity and other new states can be brought about through an accurate experimental investigation of the magnetic transitions and quantum critical behaviour of different ferromagnetic materials including URhGe and UGe_2 and to look for novel behaviour relevant for future applications. To tune materials to the QCP where new state formation is anticipated usually requires working at extreme conditions of high pressure and high magnetic field.

1.2 Sample environment and Instrumentation development

Onsite facilities include a customized cryomagnet, Physical Property Measurement System (PPMS) and Magnetic Property Measurement System (MPMS). PPMS and MPMS can be used to study the physical properties of materials such as the resistivity, heat capacity and magnetization at temperatures between 400 K and 1.8 K and in fields up to 7 Tesla. The customized cryomagnet consists of an Oxford Kelvinox 400 dilution refrigerator and a superconducting magnet, which can cool a sample down to temperatures as low as 10 mK and subject it to the magnetic fields of up to 17 Tesla. In order to measure the low energy magnetic transition that may bring about or be a result of new state formation, neutron scattering studies are carried out at central facilities on stations equipped with some cryogenic equipment.

However, high-pressure instruments and low-temperature inserts used to perform specialised measurements such as Quantum Oscillations (QO) in the electrical resistivity and neutron scattering at extreme conditions need to be custom-designed. The aim of this project is to develop the sample environment for enhance studies of the ferromagnetic superconductors at low temperatures and high magnetic fields.

Instrumentation development is done in two major areas – laboratory measurements and neutron scattering. The effort was mainly focused on developing inserts into the customized cryomagnet for making magneto-transport and QO measurements at high pressures, magnetic fields and sub-Kelvin temperatures, as well as designing diamond-anvil high-pressure cells and auxiliary equipment for use in the low temperature and high field measurement system such as PPMS and MPMS.A large-volume non-magnetic pressure cell has been designed for inelastic neutron scattering experiments. Design process involves reviewing previous designs, creating a prototype using Computer Aided Design (CAD) software and verifying the performance and the safety of use of the proposed design using Finite Element

Analysis (FEA) software. The technical drawings are produced based on the finalized design and passed onto the workshop for manufacturing. The instruments are assembled and tested before they are used in measurements.

1.3 Introduction of high-pressure cells

1.3.1 Diamond anvil cells and piston-cylinder cells

Since most of the instrumentation development presented in this thesis is concerned with high-pressure devices, a brief introduction of two major classes of high-pressure cells is given below.

Pressure is equal to the normal force over the area, which means that applying a moderate force to a tiny area can generate high pressures. The diamond anvil cell (DAC) is a common example of the idea described above. The DAC was invented in 1959 by Wier[3] and the basic parts of the opposed diamond anvil device are shown in Figure 1.1. The cell consists of a pair of opposed diamond anvils and a metal gasket. When the gasket is compressed between two diamond anvils, high pressure is generated in the gasket hole. The maximum pressure generated is based on the size of the diamond culet and the backing plates used to support the diamond anvils. David simplified the shape of diamond anvils and derived the maximum pressure as a function of the culet diamond[5]

$$P_{max}(GPa) = \frac{12.5}{(d(mm))^2} \tag{1.1}$$

He also pointed out in experiments the maximum pressure should be lower than the value calculated from equation 1.1, such as 0.8 $P_{\max.}$

There are a number of various modifications of the DACs but here we will consider just three widely used devices such as National Bureau of Standards (NBS) cell, Bassett cell and Mao-Bell cell. NBS DAC developed by Piermarini and Block in 1975 makes use of a lever-arm system to transfer the applied load to the diamond anvils and a maximum pressure of 50 GPa has been achieved.[6] Force is applied using a threaded driving piston cylinder assembly in the Bassett cell developed in 1967 and 40 GPa is reached in it with 300 μm culet diamond anvils by Jayaraman in 1972.[7,8] The first DAC that generated pressure exceeding 100 GPa is Mao and Bell cell.[9] Mao and Bell cell consists of two parts: a Belleville spring-loaded lever arm and a detachable piston-cylinder assembly, which combines the features of both NBS cell and Bassett cell.

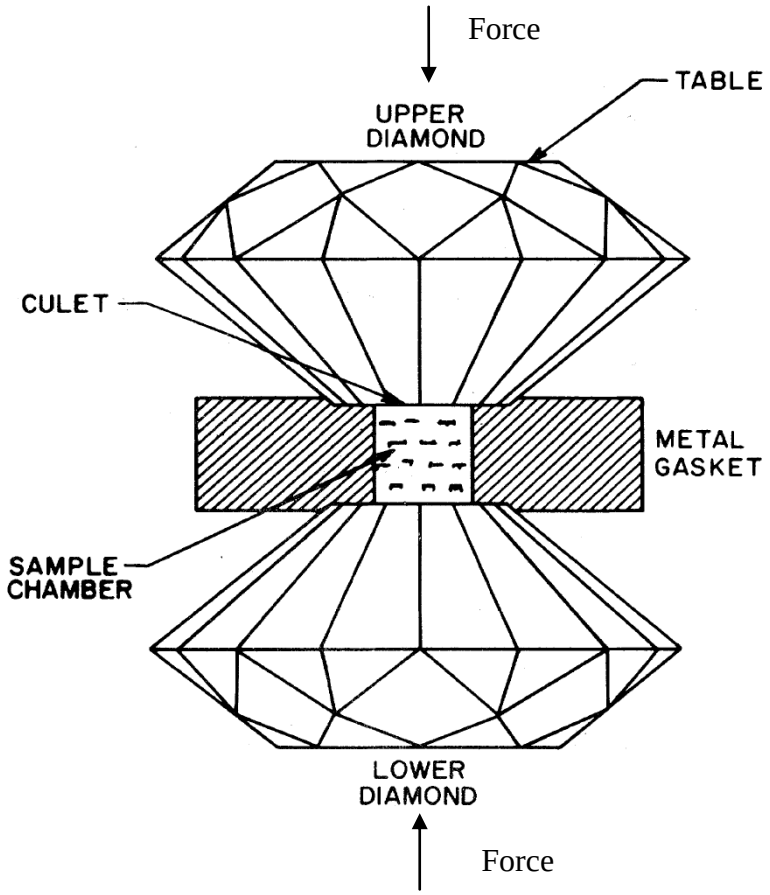

Figure 1.1 A schematic drawing of the DAC.[4]

Piston-cylinder cells are another type of high-pressure devices. Pressure is generated by compressing a medium in a cylinder. Due to the limitation of the yield strength of materials that are used to make the cylinder, the pressure limit for piston-cylinder cell is about 5 GPa.[10] In order to reach 5 GPa at room temperature, Lavergne and Whalley used a hybrid clamped cell made of 350 and 300 grades of maraging steels. Although the maximum achievable pressure is far lower than that in the DAC, the substantial sample volume is the advantage. A schematic drawing of a two-layered piston-cylinder cell is shown in Figure 1.2. A typical double layered piston-cylinder cell usually consists of locking nuts, inner cylinder, outer cylinder, a piston, an electrical feed-through, sealing rings, etc.

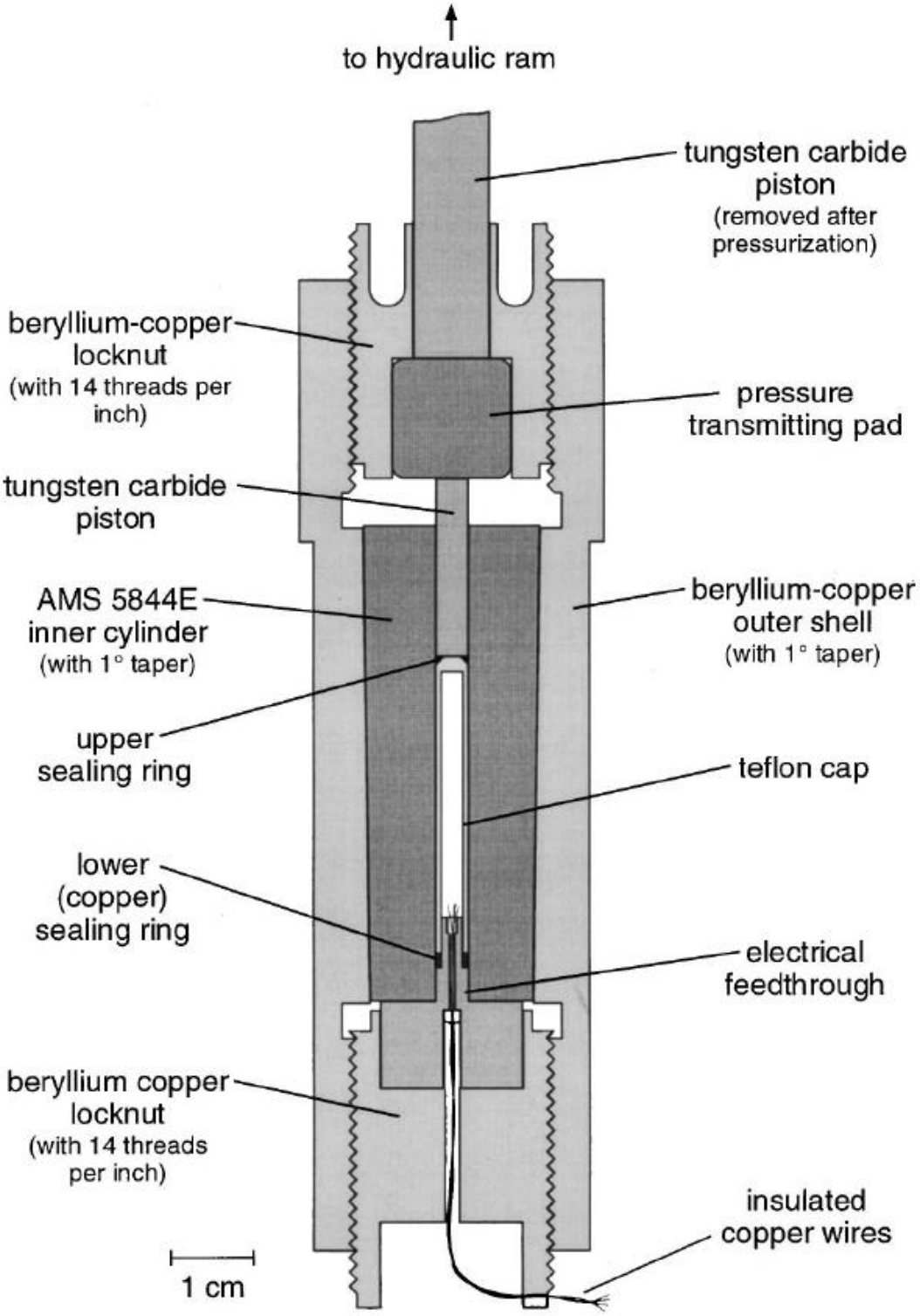

Figure 1.2 A cross-section view of a typical piston-cylinder cell.[11]

1.3.2 Pressure transmitting medium

The hydrostaticity of the pressure medium is of great importance in high pressure research since the sample can be broken by the shear stress developed during the solidification of the pressure transmitting medium, or the appearance of the measured property can change leading to the inaccuracy in the obtained experiment results. Therefore, a hydrostatic pressure environment is a highly desirable feature in high-pressure devices. Fluorinert^{TM}, noble gases and Daphne oil are often used as pressure-transmitting medium in high-pressure experiments.

Fluorinert (FC) is a 3M trademark for a series of perfluoro-carbon liquids and is popularly used as a pressure transmitting medium in high-pressure neutron scattering measurement since it exhibits very small incoherent scattering of neutrons.[12] The commercially available FCs are FC70, FC75, FC77, FC84 and FC87. As the FC grade increases, the average molecular weight, density and kinematic viscosity of the FCs decrease but its vapour pressure increases.[13] The hydrostatic limit of FC72, FC77, FC75, FC40 and FC70 was reported by Varga *et al.* in 2003 and it was shown that FC 75 exhibit the highest hydrostatic limit (1.2 GPa).[14] In 2005, Sidorov and Sadykov discovered that a mixture (1:1) of FC84 and FC 87 at room temperature shows the highest hydrostatic limit (2.3 GPa) compared to other mixtures of FCs.[12]

Among the noble gases, helium is the best available pressure transmitting medium (up to 40 GPa at room temperature),[15] even though it freezes at 12.1 GPa at room temperature.[15] The hydrostatic limit of nitrogen was found to be 13 GPa but above 13 GPa, it becomes very non-hydrostatic.[17]Argon is almost hydrostatic at up to 20 GPa, but above that pressure the pressure gradient increases dramatically.[15]

Daphne 7373 has been developed by Idemitsu company. It is a mixture of several olefins, which means it contains plenty of hydrogen atoms. Therefore it is not

suitable for neutron scattering measurements. Compared with the FC77/70, Daphne 7373 shows almost no discontinuous pressure drop during the solidification and has a higher hydrostatic pressure limit of 2.2 GPa at room temperature.[18,19]

1.4 The Thesis layout

Chapter 1 begins with the motivation and objectives of the project and an introduction of two types of high-pressure cells is provided.

Chapter 2 explains the concepts of magnetism, superconductivity and quantum critical points followed by a brief review of two ferromagnetic superconductors (UGe_2 and URhGe).

Chapter 3 discusses the design of a two-axis rotating stage for use in a customized cryomagnet. FEA is used to optimize the shape of the rotator and the calculations on how to reduce the heating by Eddie currents are presented. The setup of the experiment and the results of the quantum oscillation measurement conducted on URhGe single crystal are shown and discussed.

Chapter 4 presents the design of a miniature diamond anvil cell based on the turnbuckle principle and the gearbox for loading the noble gases either at ambient temperature or at 77 K.

Chapter 5 demonstrates how pressure can be used to tune in the property of a material. A high-pressure resistivity study conducted on a PrNi single crystal in a DAC is presented. It also includes the description of the setup for high-pressure resistivity measurements in a diamond anvil cell and the discussion of the results.

Chapter 6 presents the design of a two-layered piston-cylinder clamped cell for inelastic neutron scattering measurements. The challenges to design such a pressure cell are discussed and the use of FEA to optimize the neutron transmission of the pressure cell as well as to ensure its safe use is described.

1.5 References

1. S. Saxena *et al*., Nature **406**, 587 (2000).

2. D. Aok *et al.*, Nature **413**, 613 (2001).

3. C. E. Wier *et al*., J. Res. Nat. Bur. Stand. **63A**, 55 (1959).

4. A. Jayaraman, Rev. Mod. Phys. **55**, 65 (1983).

5. D. Dunstan *et al*., J. Phys. E: Sci. Instrum. **22**, 913 (1989).

6. G. J. Piermarini *et al*., Rev. Sci. Instrum. **46**,973 (1975).

7. W. A. Bassett *et al*., Rev. Sci. Instrum. **38**, 37 (1967).

8. A. Jayaraman, Phys. Rev. Lett. **29**, 1674 (1972).

9. H. K. Mao *et al*., in Carnegie Institution of Washington Year Book **77**, 904 (1978a).

10. A. Lavergne *et al*., Rev. Sci. Instrum. **49**, 923 (1978).

11. I. R. Walker, Rev. Sci. Instrum. **70**, 8 (2000).

12. V. A. Sidorov *et al*., J. Phys. Condens. Matter. **17**, S3005 (2005).

13. G. J. Piermarini *et al*., J. Appl. Phys. 106 889 (1973).

14. T. Varga *et al*., Rev. Sci. Instrum. **74**, 4564 (2003).

15. S. Klotz *et al*., J. Phys. D: Appl. Phys. **42**, 075413 (2009).

16. W. L. Vos *et al*., Phys. Rev. B **42**, 6106 (1990)

17. R. LeSar *et al*., Solid State Commun. **32** 131 (1979).

18. K. Murata *et al*., Rev. Sci. Instrum. **68**, 2490 (1997).

19.K. Yokogawa *et al*., Jpn. J. Appl. Phys. **46**, 6A, pp.3636 (2007).

Chapter 2 Literature review

2.1 Introduction

Until the discovery of the ferromagnetic superconductors, superconductivity and ferromagnetism were thought of as two competing states that cannot coexist because it was believed the magnetic field produced by aligned moments in ferromagnets can destroy the superconductivity. The coexistence of superconductivity and ferromagnetism reported in three uranium compounds UGe_2, URhGe and UCoGe[1-3]attracted a lot of interest but the microscopic pairing mechanism that drives the superconductivity in those compounds is still unclear. To probe and better understand such a complicated mechanism, custom-designed instruments for high pressure, high filed and low temperature measurements are required. In order to study UGe_2 and URhGe thoroughly, instruments, developed for carrying out physical property measurements such as inelastic neutron scattering and quantum oscillations, are described in the following chapters. In this chapter, a brief introduction of the magnetism, superconductivity, Fermi surface and quantum critical point is presented below and followed by a review of previous studies on UGe_2 and URhGe.

2.2 Magnetism

Magnetism is a property of materials and is produced by the nuclear spin, the magnetic spin of an electron and the motion of electrons around their orbitals in the atoms. The motion of the electrons around the nuclei and themselves produces the orbital angular and spin momentum, respectively. When a material is placed in a magnetic field (H), it acquires a magnetic moment. The dipole moment per unit

volume is defined as the magnetization (M) and the magnetic susceptibility (χ) is a dimensionless constant, which is used to indicate the degree of magnetization and defined by the relationship[1]

$$\chi = \frac{M}{H} \tag{2.1}$$

Diamagnetism exists in all materials and is the weakest form of magnetism. Electrons are paired up in diamagnetic materials so the magnetization originates only from the motion of the electrons around the nuclei. This leads to a small magnetic moment which is opposed to an applied field and that explains why diamagnetic materials are repelled by a magnet. The magnetic susceptibility for diamagnetic materials is negative and is weakly dependent on temperature and magnetic field.

Unpaired electrons existing in paramagnetic materials can align their magnetic moments in any direction. In the presence of external magnetic field, those unpaired electrons tend to align their magnetic moments towards the direction of the field. The magnetic susceptibility for paramagnetic materials is positive and is considered to be independent from the magnetic field. However, it decreases with the increasing temperature and obeys the Curie law:

$$\chi = \frac{C}{T} \tag{2.2}$$

Where C is the material-specific Curie constant and T is the absolute temperature measured in Kelvins.

Unpaired electrons also exist in ferromagnetic materials but ferromagnetic materials have a spontaneous magnetization even without the presence of the externally applied field. Within ferromagnetic materials the magnetic moments have strong

interactions with their neighbouring moments and align in the same direction only below the critical temperature known as the Curie temperature (T_C). The magnetic susceptibility of ferromagnetic materials is positive and depends on the temperature and magnetic field. In the paramagnetic region, the magnetic susceptibility is well described by the Curie-Weiss law:

$$\chi = \frac{C}{T - T_C} \tag{2.3}$$

Where *C* is the material-specific Curie constant.

Similarly to ferromagnetic materials, within which the magnetic moments line up in the same direction only below the Curie temperature, the magnetic moments in an antiferromagnetic material only align in a regular pattern with neighbouring spins pointing in opposite directions below a critical temperature known as the Néel temperature (T_N). The magnetic susceptibility of anti-ferromagnetic materials rises with the increasing temperature and is field-dependent. Antiferromagnetic materials become paramagnetic above T_N like that ferromagnetic materials do when the temperature is above T_C. For the antiferromagnetic materials, the Curie –Weiss law is derived and given by

$$\chi = \frac{C}{T - T_N} \tag{2.4}$$

Magnetic materials with localized magnetic moments or spins interacting through competing exchange interactions that cannot be satisfied simultaneously are called frustrated magnets. A spin glass is a typical phase existing in the frustrated magnets. The magnetic field dependence distinguishes it from other magnetic phase. Above the spin glass transition temperature (T_g), the spin glass follows the typical magnetic

behaviour that the magnetisation increases with the decreasing temperature. When it reaches T_g, the magnetisation freezes and remains nearly constant with further cooling. The magnetisation of the spin glass drops rapidly to a certain value known as the remanent magnetisation when the field is removed and it decays rather slowly towards zero.

2.3 Superconductivity

The electrical resistivity is a property of materials and it changes with temperature. Many metals and alloys show a sudden drop of the electrical resistivity to zero when the material is cooled to a sufficiently low temperature (T_C). This phenomenon is called superconductivity. It was observed first by Kamerlingh Onnes in Leiden in 1911.[5]

According to their behaviour in magnetic field, conventional superconductors are divided into two categories, known as the type I superconductors and type II superconductors. The superconductivity of type I superconductors can be destroyed by a relatively low external magnetic field. The value of the magnetic field where the superconductivity vanishes is called the critical field (H_C). H_C decreases with temperature increasing and becomes zero at the superconducting transition temperature. Most of the elements exhibiting superconducting behaviour are type I superconductors and all alloys are type II superconductors. Unlike type I superconductors change from a superconducting state to a normal conducting state at a single critical field, type II superconductors change from one state to the other over the range of fields between H_{C1} and H_{C2}. H_{C1} and H_{C2} is known as the lower critical field and the upper critical field, respectively.

Between H_{C1} and H_{C2}, a material is in a mixed state where some parts of it are in

the superconducting state and the rest is behaving like a normal conductor. The value of H_{C2} can be 100 times higher than that of H_{C1}.

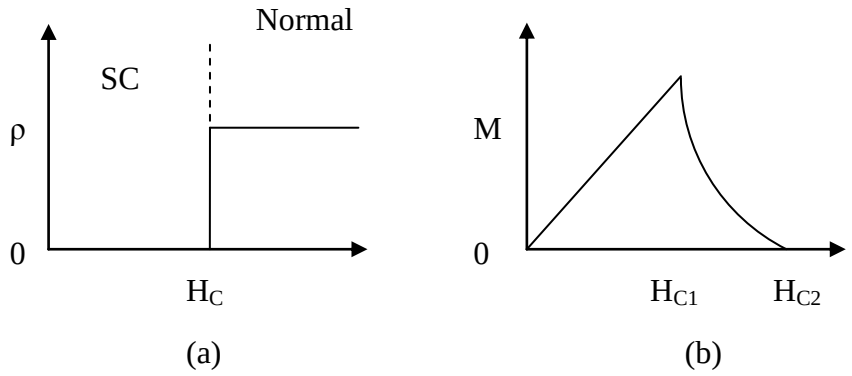

Figure 2.1 (a) Field–dependence of electrical resistivity in Type I superconductor (b) Field-dependence of magnetisation in Type II superconductor.

Besides the zero electrical resistivity, the magnetic properties of superconductors are also unusual. Levitating a small magnet above a superconductor is widely used in labs to demonstrate the phenomenon of superconductivity. This is based on the Meissner effect[6] which states that a superconductor will repel magnetic flux when it is cooled below the T_C. External magnetic field induces electric currents on the surface of the superconductor and the magnetic field created by this current is opposed to the field that created it. Above the T_C, the magnetic flux can penetrate the superconductor as illustrated in Figure 2.2.

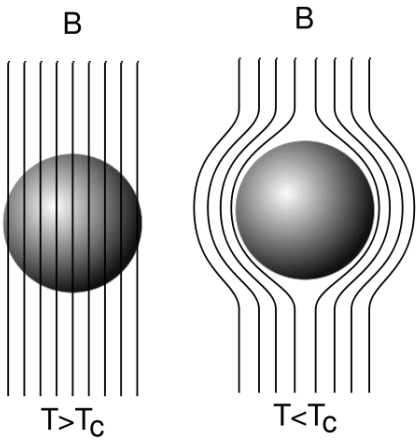

Figure 2.2 The illustration of the Meissner effect.[7]

Superconductors behave like perfect diamagnets, which also produce a magnetic field opposed an external magnetic field.[8] However, the Meissner effect is solely produced by the electric currents flowing on the surface of the superconductor, which indicates that electrons in superconductors may behave in a collective manner.[9] For type I and type II conventional superconductors the theory is very well developed and agrees well with the experiment. However, there are still some problems with theory for high temperature and newly discovered unconventional superconductors. BCS theory[10], developed by American physicists John Bardeen, Leon Cooper, and John Schriefferin 1957, is widely used to explain the mechanism of the superconductivity in the conventional superconductors. The theory assumes electrons with opposite spins become pairs, forming so-called Cooper pairs. A current is produced when Cooper pairs move through a superconductor without encountering any resistance. At the lowest energy state, all the electrons within a superconductor will form Cooper pairs at $T = 0$ K. This simplified explanation suggests that the electrons in a Cooper pair are bound closely.

The discoveries of unconventional superconductors such as heavy-fermion superconductors[11,12], cuprates[14,15],iron-based superconductors[15] etc challenge the

BCS theory. Magnetic 4f and 5f ions were assumed incompatible with superconductivity because those magnetic impurities can break the Cooper pairs.[16]However, they exists in heavy-fermion superconductors. Cuprates has violated the rules set by Bernd Matthias, which are based on the cubic transition metal alloys but in Cuprates carriers are doped into an insulating magnetic oxide. Although Cuprates and Iron-based superconductor have different chemical compositions, they have many properties in common. Some people believe the superconductivity is mediated by quantum critical fluctuation in those exotic forms of superconductors.

2.4 Fermi surface and Quantum critical Point

The Fermi surface is the surface of constant energy in the reciprocal or *k* space and separates the unfilled orbitals from the filled orbitals at absolute zero temperature.[7] The shape of the Fermi surface determines the thermal electrical, magnetic and optical properties of the metal. In order to determine electronic Fermi surface, oscillation of physical properties such as magnetic susceptibility and resistivity are measured in high magnetic fields, which are also known as the de Haas-van Alphen effect (dHvA) and the Shubnikov–de Haas effect (SdH), respectively.

Quantum critical point (QCP) is formed by using some external parameter such as high pressure, high magnetic field and chemical doping to tune the critical temperature of a phase transition to absolute zero. Thermal fluctuations usually drive the phase transition but the critical fluctuations at QCP are quantum mechanical rather than thermal. As shown in Figure 2.3, the red cone indicates new quantum phase that is very fragile and can be easily destroyed by the imperfections in crystals. Nowadays scientists have been working hard to grow the high-quality crystals and with the help of state-of-the-art high-field and low-temperature system, they can

better understand the quantum criticality.

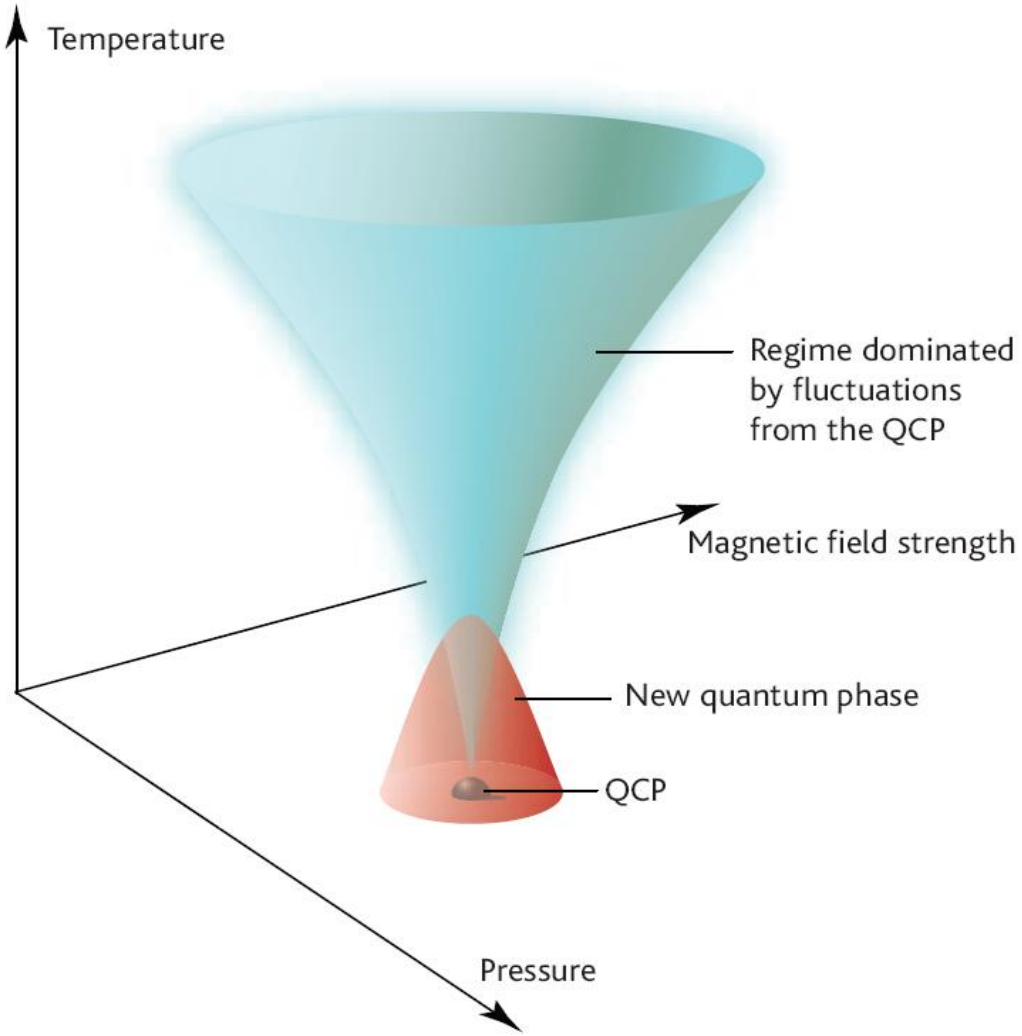

Figure 2.3 A schematic quantum critical phase diagram.[17]

2.5 Ferromagnetic superconductors UGe_2 and URhGe

The BCS theory is able to explain the mechanism for conventional superconductors but the precise mechanism for the new metallic compounds and high temperature superconductors is controversial. New theory or model for the new types of superconductors suggests the superconductivity is a result of the Coulomb interaction together with the subtle effects of quantum correlations.[1] $UGe_2$was the first

experimental confirmation although the prediction for the coexistence of superconductivity and ferromagnetism has been present for quite a few years.[18]The coexistence of the two competing phases in UGe_2 is pressure induced. The schematic pressure-temperature phase diagram of UGe_2 shown in Figure 2.4 is determined by the resistivity and susceptibility measurements. The superconductivity exists below 1 K within a limited pressure range between 1 and 1.6 GPa on the border of ferromagnetic region.[1] It can be seen that the whole superconducting dome lies within the ferromagnetic region (FM1) and at 1.2 GPa the superconducting transition temperature is ~ 0.7 K which is the maximum while the ferromagnetism is still strong with $T_C \approx 30$ K.

A second ferromagnetic (FM2) region present in Figure 2.4 is identified in resistivity measurements within the ferromagnetic state and T_x is the characteristic temperature of this transition. The value of T_x is pressure dependent that it decrease with pressure and totally suppressed at a pressure called P_x where the superconductivity is about the strongest. Inelastic neutron scattering studies at ambient pressure experimentally verified the prediction of the dynamical critical phenomena[20] but magnetic fluctuation under high pressure, especially where the superconductivity is at its maximum, is unknown. To clarify this, high pressure inelastic neutron scattering study is required.

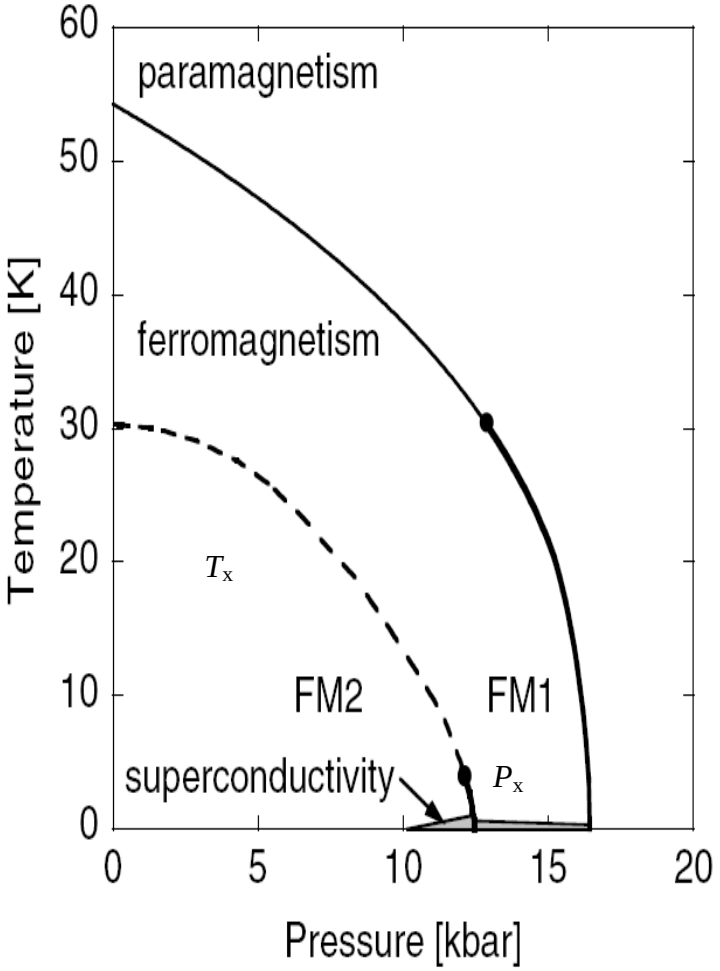

Figure 2.4 The schematic temperature -pressure phase diagram of UGe_2.[19]

Unlike UGe_2, the superconductivity in URhGe occurs at ambient pressure[2], which means more characterization measurements, such as the specific heat and magnetization, can be conducted since they are easier to perform than under pressure. URhGe orders ferromagnetically below T = 9.5 K with a spontaneous moment M_C = 0.4 μ_B parallel to the crystal c-axis and enters a bulk superconducting state deep within the ferromagnetic state at T_C = 275 mK in the cleanest crystal.[2] Magnetic field applied along b direction first destroys the superconductivity but it reappears between 8 Tesla and about 12.5 Tesla with a higher T_C than at zero field.[21]

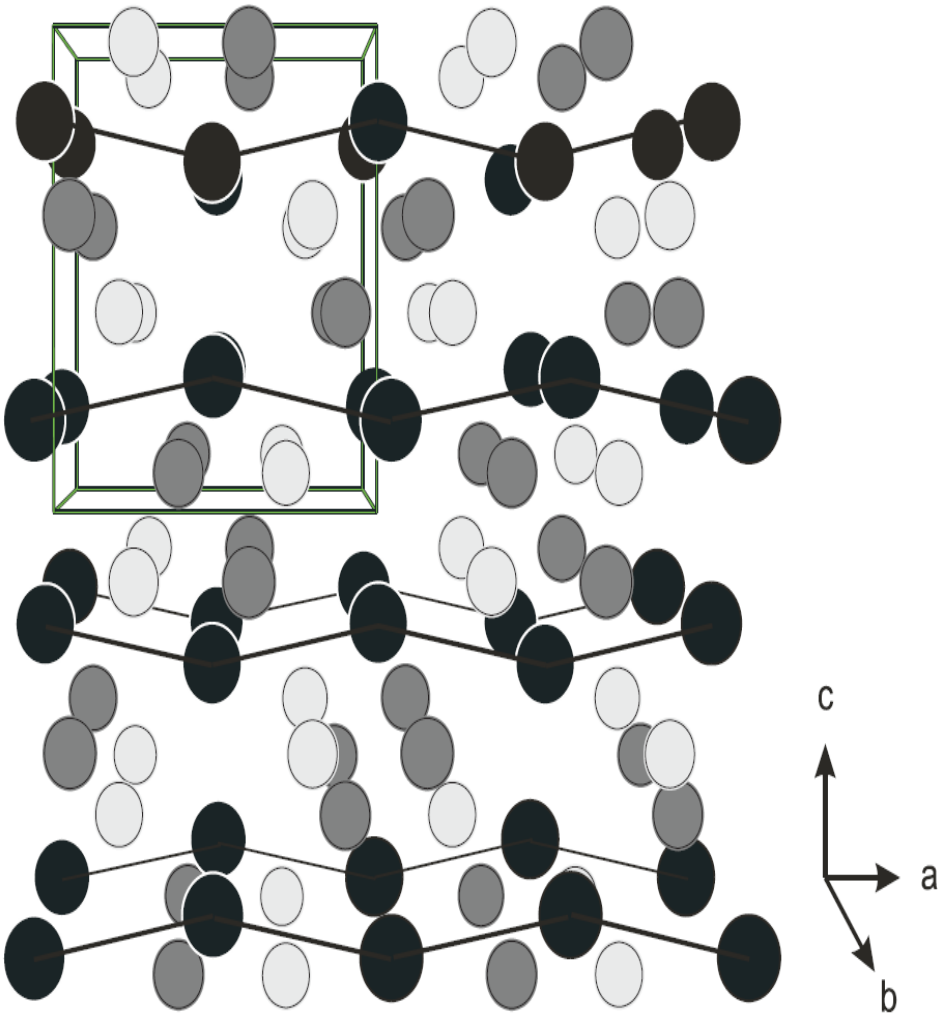

Figure 2.5 The TiNiSi type orthorhombic structure of URhGe.[22] (Uranium atoms are black, rhodium atoms light gray and germaniums are dark gray.)

As shown in Figure 2.6, the first-order transition bifurcates into two spurs at a field of about 12 T at a tricritical point (TCP) where the continuous transition lines separate. The QCP is known as a special class of continuous phase transition occurring at the absolute zero temperature driven by the magnetic field, pressure or chemical doping, and the formation of superconductivity is found to be close to the magnetic QCPs.[21] In the case of URhGe though, it seems that the field along the c axis which replaces the pressure as the parameter which in the case of UGe_2 was

driving the transition.

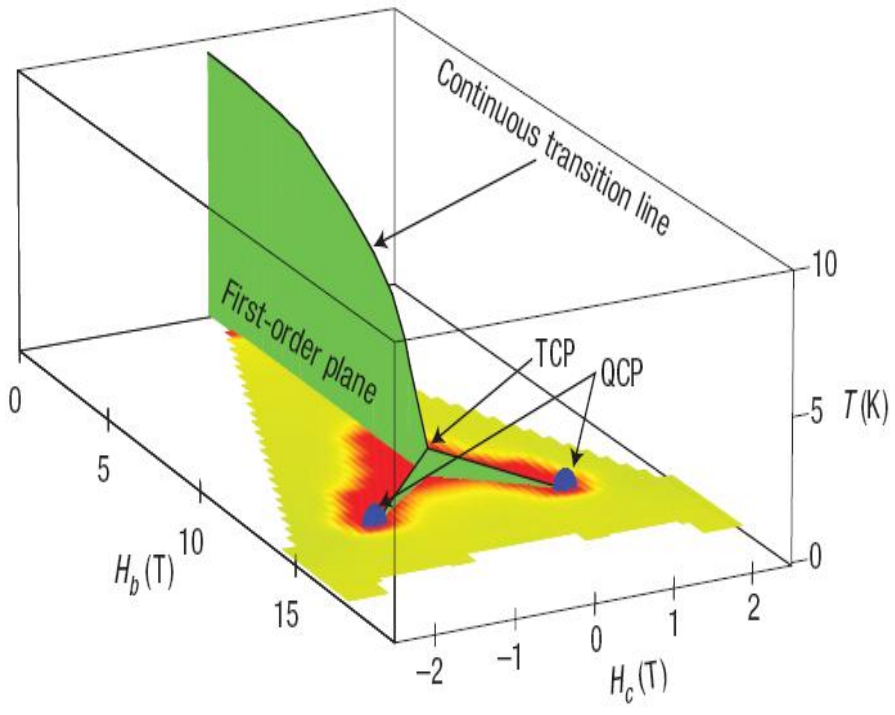

Figure 2.6 The schematic field-temperature phase diagram of URhGe for magnetic fields in the bc plane. The low temperature resistivity at 50 mK for fields in the bc plane is shown by the colour shading on the lower face of the axis frame: yellow corresponding to a resistivity of approximately 5 μΩ cm and red to superconductivity.[23]

Therefore, the motivation to study the URhGe is that the emergence of its superconductivity is close to the QCP, which affords a powerful means to identify the mechanism that drives the formation of unconventional superconductivity in heavy fermion materials.

2.6 References

1. S. S. Saxena *et al*., Nature **406**, 587 (2000).

2. D. Aoki *et al.*, Nature **413**, 613 (2001).

3. N. T. Huy *et al.*, Phys. Rev. Lett, **99** 067007 (2007).

4. A. Aharoni, Introduction to the Theory of Ferromagnetism, 2nd edition. Oxford Science Publications, Oxford (2000).

5. H. Kamerlingh Onnes, Leiden Comm. 120b, 122b, 124c (1911).

6. W. Meissner *et al*., Naturwissenschaften**21**, 787 (1933).

7. C. Kittel, Introduction to Solid State Physics, 8th edition. Willey &Sons, New York (2005).

8. S. Holgate, Understanding Solid State Physics. Taylor & Francis Group, Boca Raton (2010).

9. F. London, *Superfluids.*Vol. 1.Wiley, New York, (1950).

10. J. Bardeen *et al*., Phys. Rev. **108**, 1175-1204 (1957).

11. F. Steglich*et al*., Phys. Rev. Lett. **43**, 1892 (1979).

12. G. R. Stewart, Rev. Mod. Phys. **56**, 755 (1984).

13. J. G. Bednorz *et al*., Z. Phys. B **64**, 189 (1986).

14. N. E. Bickers *et al*., Int. J. Mod. Phys. B **1**, 687 (1987).

15. F. Wang, *et al*., Science **332**, 200 (2011).

16. A. A. Abrikosov *et al*., Sov. Phys. JETP **12**, 1243 (1961).

17. A. P. Mackenzie *et al*., Science **309**, 1330 (2005).

18. D. Fay *et al*., J. Appel, Phys. Rev. B **22**, 3173 (1980).

19. A. D. Huxley *et al*., Phys. Rev. Lett, **91** 207201 (2003).

20. S. Raymond *et al*., Physica B, **350**, 33 (2004).

21.F. Lévy *et al*., Science **309**, 1343 (2005).

22. S. Sakarya, Magnetic properties of uranium based ferromagnetic superconductors. IOS Press (2006).

23. F. Lévy *et al*., Nature Physics **3**, 460 (2007).

Chapter 3 The development of a two-axis rotating stage for studying quantum oscillations in cryomagnets

3.1 Introduction

Rotating a single crystal with respect to the axis of the magnetic field at low temperature is desirable for scientists who would like to study the angular and temperature dependence of the magnetic and electronic properties in low dimensional and orientation sensitive samples. To perform such experiments, either a spinning magnet or a rotatable sample stage is needed. Commercially available 3-axis or 2-axis superconducting magnet developed by Oxford Instruments Inc. and American Magnetics Inc. can only generate magnetic fields up to 3 Tesla rotating the vector using a combination of x, y, z-axis magnets at a temperature range between 30 mK and 300 K. The limitations of those rotatable magnets are the operating temperatures being limited by 30 mK and the low amplitude of the magnetic field.

In anisotropic URhGe, superconductivity coexists with the ferromagnetic state at T_{SC} = 275 mK.[1] The superconductivity disappears when magnetic field is applied along the crystal b axis but it reappears between 8 T and ~ 12.5 T.[2] In order to study the quantum oscillations (QO) in the high field and low temperature superconductors such as URhGe, a customized cryomagnet shown in Figure 3.1 is used. It consists of a Kelvinox 400 dilution refrigerator (Oxford Instruments Inc.) that can cool down a sample below 10 mK and a superconducting magnet which can generate a magnetic field (B) up to 17 Tesla.

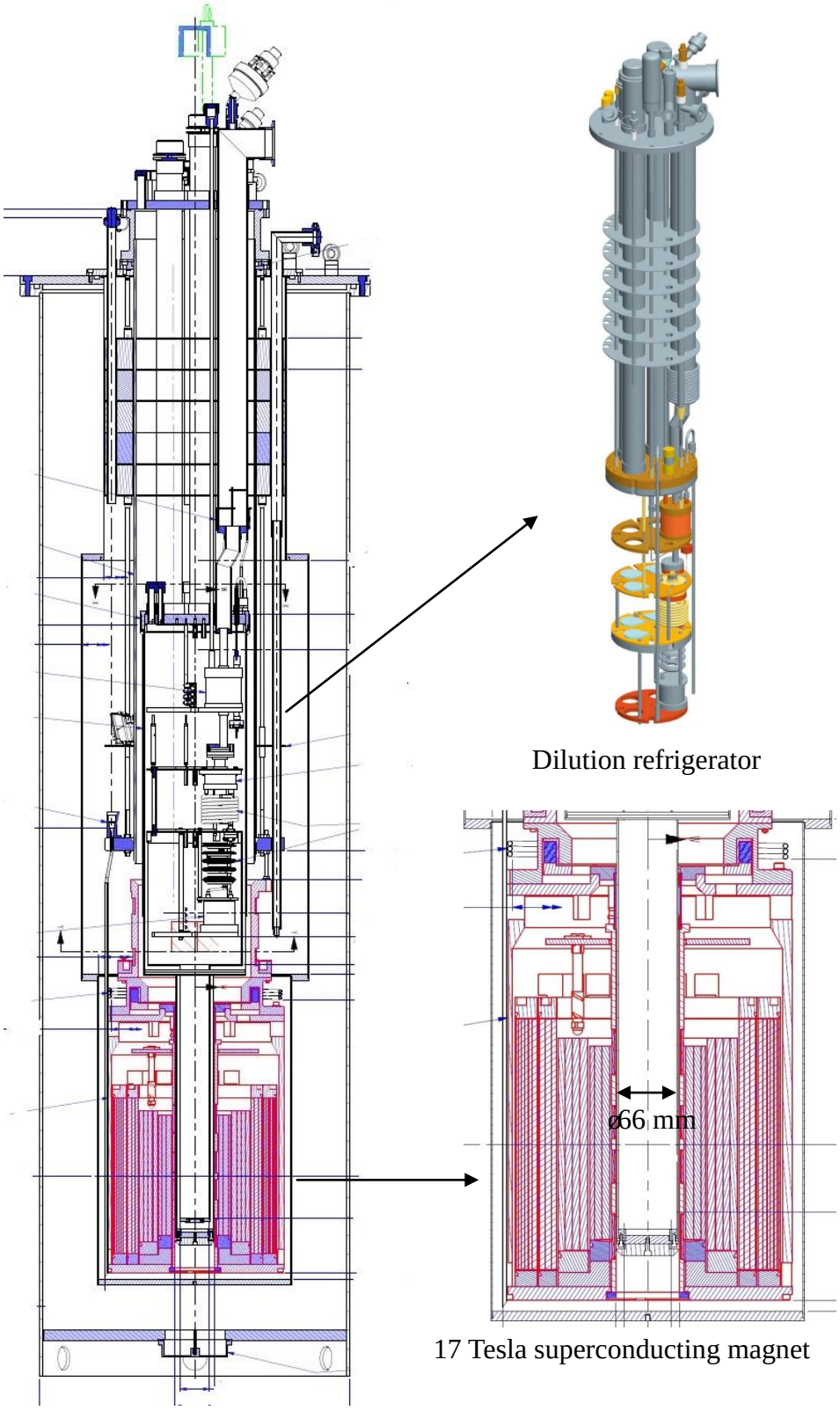

Figure 3.1 The customized cryomagnet.[3]

In the following section, the existing rotating stages built for the cryomagnets are reviewed and the challenges one has to face when designing such a device are discussed.

3.2 Design challenges

The main challenges in designing a rotating stage that works at very low temperatures and in high magnetic fields are the friction heating while rotating a sample, eddy current heating from either fast ramping of the field or from rotating the sample and the limited space in the bore of the superconducting magnet. In order to study unconventional superconductors, the use of high resolution angular sensor is of great importance since they are more likely to exhibit strong anisotropy in the upper critical field.[2]

Several rotating stages that work at low temperature and high magnetic field have been reported in the literature. The first type of the rotating system requires mechanical linking between the controls at room temperature and the rotator in the sample space. The worm-gear mechanism rotators driven by an external motor developed by Bhattacharya *et al.* for Quantum Design MPMS SQUID could operate at temperature of 2 K but substantial heat is introduced to the sample environment due to the friction.[4] The rotator that makes use of sapphire vee jewels and matching pivots from Swiss Jewel has been developed by Palm and Murphy to reduce the heat from the friction.[5] With a rather slow rotating speed of 0.33 deg/s, the temperature increases by 8 mK at 30 mK, which means the friction is reduced dramatically.

The second type of rotating mechanism utilises piezoelectric actuators which eliminate the need in mechanical linking to controls outside the cryostat. The actuators also provide higher angular resolution. A rotating stage with the angle

resolution better than 0.01° based on piezoelectric rotators has been developed by Ohmichi *et al.* and tested down to 100 mK and up to 33 Tesla.[6] The heat generated by the rotation is lower than 100 μW but the disadvantage of this rotator is that the rotating angle is limited to ±10 °. LaReine *et al.* recently reported a piezoelectrically driven sample rotation system built to work with an Oxford Instruments Kelvinox 100 dilution refrigerator. In their system, the sample can be rotated by more than 100 ° but around a single axis only.[7]

So far, all the rotating stages built for high field and low temperature environments can only rotate the sample along one single crystallographic axis with respect to the direction of the magnetic field, which means they cannot be used to study anisotropic samples if more than one axis needs to be examined. Existing systems require changing the orientation of the sample manually, which means that the cryo-magnet needs to be warmed up to ambient temperature for the orientation to be changed. This is very time consuming, wastes a lot of cryogenic resources and might introduce errors into the measurements.

In the following section, the design of a two-axis rotating stage for studying quantum oscillations in URhGe at sub-Kelvin temperatures and magnetic fields up to 17 Tesla and its integration into the customized cryomagnet is presented.

3.3 Design of the rotating stage and materials selection

3.3.1 The design and materials selection

The construction of the rotating stage is shown in Figure 3.2. This two-axis rotating stage consists of two rotators, one top and one bottom bracket, three supporting brackets, two flexi-cable mounting pads, one guarding bracket and one pivot. The

main components of the assembly are two piezoelectric motors ANRv101/RES and ANR101/RES (Attocube Systems AG) and the supporting brackets. The working principle of rotators is based on so called slip-stick inertial motion. The rotation of two motors is controlled by the Attocube ANC350 controller unit at room temperature. The program controlling the two motors was written using Labview™.

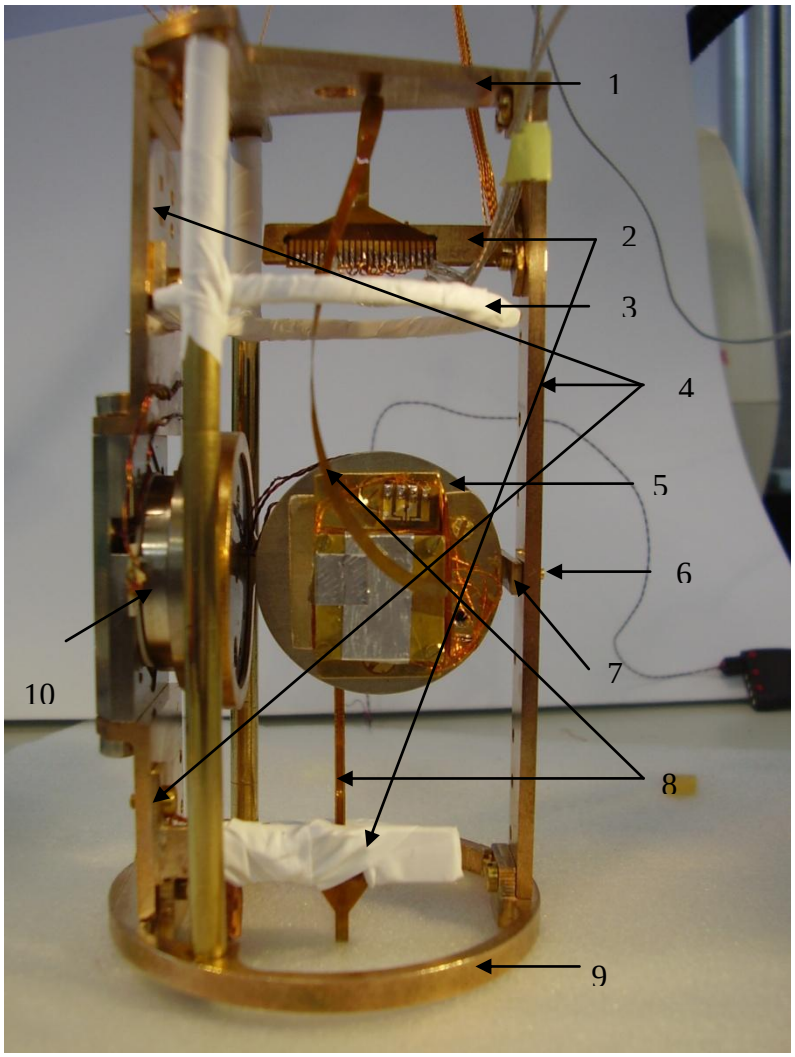

Figure 3.2 The assembly of the two-axis rotating stage. (1) the top bracket, (2) the flexi-cable mounting pad, (3) the guarding bracket, (4) the supporting brackets, (5) the vertical-axis rotator, (6) the pivot, (7) the bridging bracket, (8) the flexi-cables, (9) the bottom bracket, (10) the horizontal-axis rotator

The function of the two rotators is to rotate the sample around two perpendicular axes with respect of the direction of the magnetic field. Both motors have a ø30 mm rotating base for mounting samples and each motor can carry a maximum weight of100 g. The bridging bracket is used for connecting two rotators, and the pivot is used to support the bridging bracket during the rotation. The top bracket, the bottom bracket and three supporting brackets hold the two rotators in place. The guarding bracket is used to confine the movement of the flexi-cables to a ø52 mm diameter. In order to attach this rotating system to the mixing chamber plate an M5 thread hole is drilled in the top bracket. The whole assembly is roughly a cylindrical shape with dimension of ø54 mm × 101 mm and can fit into the 60 mm bore of many commercially available superconducting magnets.

To avoid the entanglement of the wires connected to the sample and the motors during rotation, flexi-cables shown in Figure 3.3 are used to supply power to the motors and wire samples. The flexi-cables are specifically designed and manufactured for this experimental setup. They are based on a 50 μm thick Kapton tape and the individual track made of copper coated with nickel and gold at the end of each track that is just 25 μm wide. Two flexible cable mounting pads are integrated into the design of the rotating system. One with 24 tracks is positioned on the top of the rotating system, the other with 10 tracks is positioned at the bottom to power the rotators and the built-in angle sensors.

In order to minimize the interference with the magnetic field around the sample, both rotators and supporting brackets should be manufactured from the non-magnetic materials. In order to verify the magnetic property of materials, direct current (DC) magnetic susceptibility measurements are carried out on several candidate materials in magnetic properties measurement system (MPMS). The comparison of magnetic susceptibility of those materials is shown in Figure 3.4. The BERYLCO-25 alloy[8]

shows the minimum magnetic susceptibility thus it is selected to make the supporting brackets and rotators.

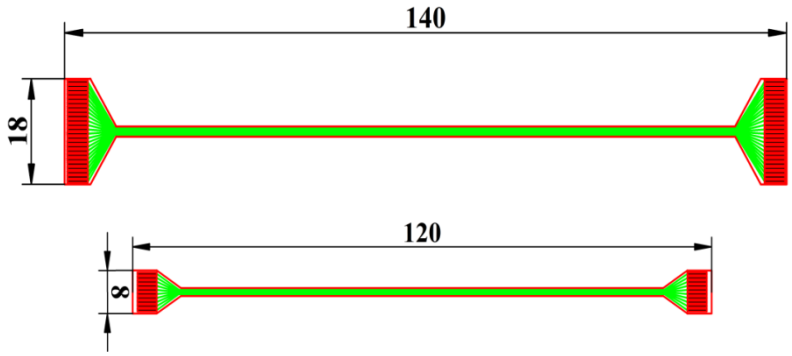

(a) A schematic drawing of the customized flexi-cables (units in mm)

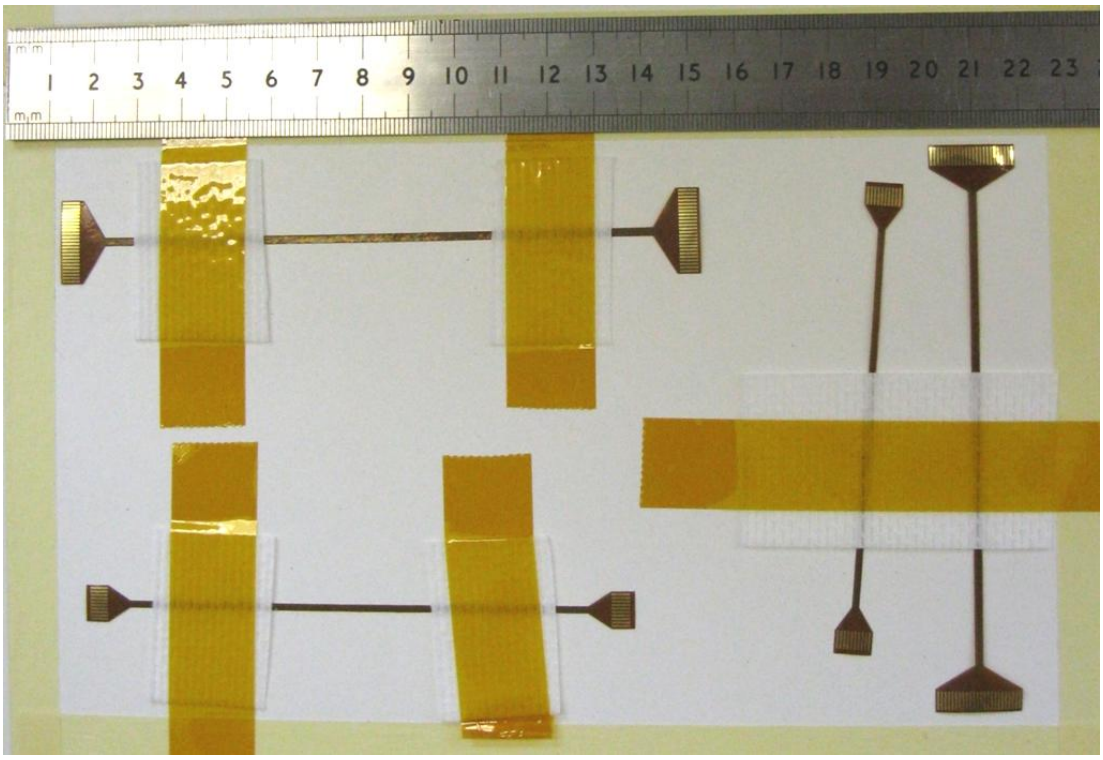

(b) Flexi-cables.

Figure 3.3 Flexi-cables.

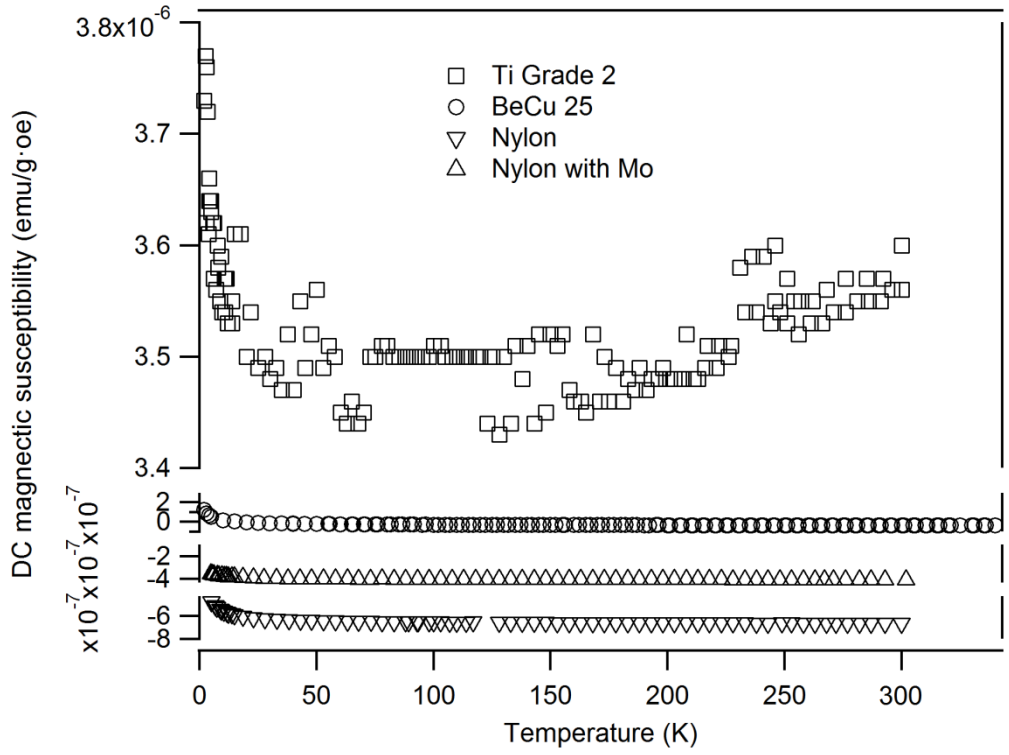

Figure 3.4 The DC magnetic susceptibility of a selection of materials considered for use in the constructions of the rotator.

10 pairs of 25 μm twisted copper wires are used as thermal link from the plate of mixing chamber of the dilution fridge to the sample. RuO_2 thermometer is calibrated for a variety of the magnetic fields and used to monitor the temperature of the sample mounted on the rotating system. The angle of rotation is measured by a resistive sensor with a sliding contact that is built into the rotators. The resistive sensor consists of a fixed arc of resistive track with a moving wiper contact. The resistance between one end of the fixed resistor and the wiper is proportional to the length of the arc up to the wiper contact and therefore proportional to the platform angle. This angle sensor can produce a resolution of 0.02 °.

3.3.2 Reduction of the vibration and heating effects in the sample environment

Vibration sources in the dilution refrigerator can be originated from the boiling of liquid nitrogen, 1 K pot mechanical pump, the ^{3}He gas-handling system and mechanical ^{3}He pump. The main source of the vibrations is from the roots and rotary pumps used for circulating the ^{3}He but Oleg *et al.* has pointed out that using the dilution refrigerator with ^{3}He cryogenic cycle circulation can significantly to reduce the vibrations from the pumps.[9]

There are different mechanisms which can cause heating at low temperature such as radio frequency (RF) power, blackbody radiation and eddy current effects. The RF power originating from the electrical oscillations at room temperature propagates down along the surface of the wires from outside the cryomagnet but can be eliminated by extensive filtering at room temperature. To reduce the radiation from the 4 K inner vacuum chamber (IVC) can of the dilution refrigerator, the lambda coil is used to cool the IVC can to 2.2 K and there is no change in base temperature.

The third source of heating is the eddy current heating. In order to reduce it, a number of slots have been cut in the supporting brackets to prevent the circulation of the current. However, the eddy current heating on the rotating system in an alternating current induced magnetic field is ineligible. The estimation of such heating is discussed as follows. The power absorbed by a sphere in an alternating magnetic field uniform in space is known to be

$$N = \tau\, \pi \int_0^{\pi} \int_0^{a} i^2 r^2 \sin\theta \; dr \; d\theta \qquad (3.1)$$

where $i = i\,(r, \theta)$ is the density of the current and τ is the electrical resistivity.[10]

By integrating equation 3.1

$$N = 3\pi\, aH^2\tau F_1(x) \tag{3.2}$$

with $F_1(x) = \frac{x(\sinh 2x + sin2x) - \cosh 2x + cos2x}{cosh2x - cos2x}$

where H is the magnetic field intensity, τ is the electrical resistivity, $x = \frac{a}{\delta}$, with a equal to the radius of the sphere, and $\delta = 1/(\pi\mu f\gamma)^{1/2}$ is the penetration depth where f is the frequency of the alternating current (AC), μ is the permeability and γ is the electrical conductivity.[11]

The equation 3.2 can be transformed into the following form

$$N = 3\pi\, a^2H^2\tau F_2(x) \tag{3.3}$$

with $F_2(x) = \frac{1}{a}F_1(\mathrm{x})$

E. Fromm and H. Jehn reported that when the ratio of the radius of a sphere to the penetration depth "*x*" is greater than 10, $F_2(x)$ can be simplified to:

$$F_2(x) = \frac{x}{a} = \frac{1}{\delta} \tag{3.4}$$

Inserting equation 3.4 in equation 3.3, N becomes

$$N = \frac{3\pi\tau a^2H^2}{\delta} = 3(\pi^3\mu)^{1/2}(f\tau)^{1/2}\, a^2H^2 \tag{3.5}$$

As the radiation power is proportional to the surface area of the conductor, it is useful

to divide the power absorption by the surface of the sphere which is given by

$$N_s = \frac{3\tau H^2}{4\delta} = \frac{3}{4}(\pi\mu)^{1/2}(f\tau)^{1/2}H^2 \qquad (3.6)$$

Equation 3.6 shows for sufficiently high frequencies the ratio of the absorbed power to the surface of the sphere becomes independent of the radius. A similar consideration can be applied to cylinders. According to the theory of induction heating the power absorbed by cylindrical specimen with a constant ratio of radius to length (a/l) is also proportional to a^2.[12] Therefore, the power absorbed by a cylindrical bracket can be calculated using equation 3.4 when x > 10. In our case, the value of x is verified by using a = 0.027m, $\mu = 1.26\times10^{-6}$ H/m, f = 30 Hz and $\gamma = 9.86\times10^{6}$, which gives the value of x equal to 411.4.

In order to use the equation 3.5, the whole assembly are assumed to be a cylindrical structure with a = 27 and l = 101mm. Because the frequency and amplitude of the eddy current in the AC field is typically between 1 and 30 Hz and 0 and 10 mT, the power absorbed by the whole assembly at f = 30 Hz and H = 10 mT is 238.4 μW. Although the calculated heating power from the eddy current effect is smaller than the cooling power of the dilution refrigerator below 100 mK, the temperature still goes up when the field is sweeping due to other heating effects. With all these efforts we made to the rotating system, the rotator can reach the base temperature of 50 mK, 80 mK and 120 mK at a static magnetic field of 0 T, 10 T and 15 T, respectively.

3.3.3 Stress and deformation analysis

Rotating a pressure cell in a cryomagnet is not novel since Bangura *et al.* performed angle-dependent magneto-transport measurements under pressure in field of up to 33 Tesla at temperatures between 0.5 K and 4.2 K.[13] However, no one has ever rotated a

pressure cell around two axes. Our rotating system is also designed to rotate a pressure cell with respect to two axes at temperatures down to 100 mK and magnetic fields up to 17 T. In order to reduce the thermal mass of the rotator its dimensions were optimised using FEA. The analysis has been conducted to assess the deformations in the rotating stage carrying a 46 gram diamond anvil high pressure cell, D-Cell[14], mounted on the vertical axis rotator.

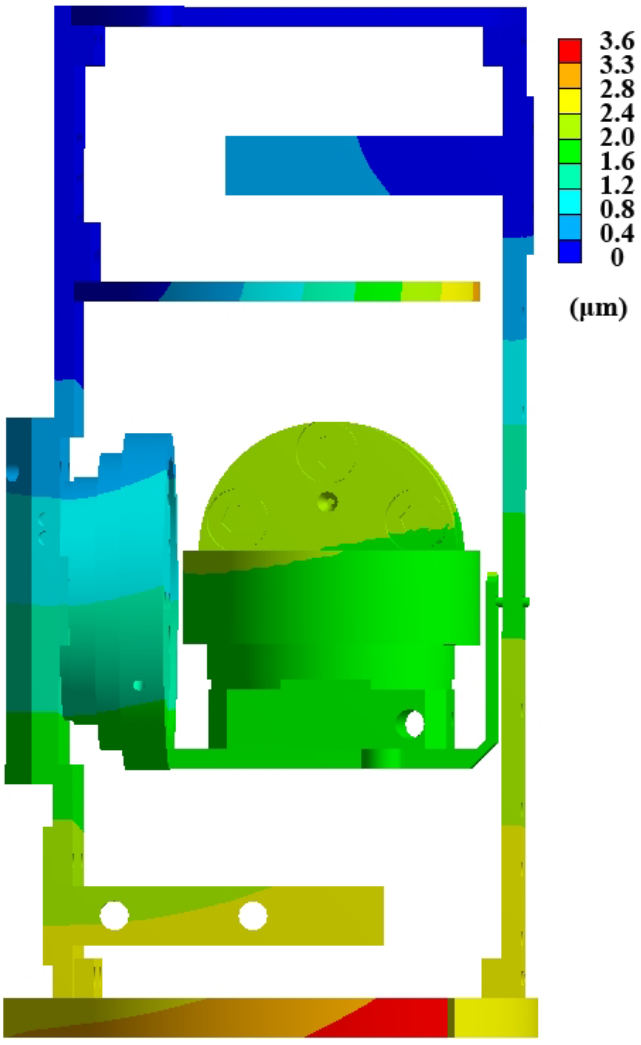

Figure 3.5 The FEA result of the total deformation of the suspended rotator under its own weight.

The supporting brackets and rotators and the pressure cell are connected using

miniature bolts and nuts so the connection between each component in the FEA model is defined as bonded, which means the connections are solid linked and the assembly behaves as one part. Fixed support is applied to the top bracket due to its attachment to the plate of the mixing chamber is done by 3 stainless steel tubes that hold it in place. Standard Earth gravity of 9.8 m/s^2 is applied to all the parts. Therefore, the total deformation to the system is mainly due to the weight of each part. The maximum deformation of 3.6 μm occurs at the slotted opening in the bottom bracket. Similarly slotted opening has been made to the flexi-cable guarding bracket, on which a transitional deformation can be seen. The FEA results prove the deformation of the whole system is acceptable since it does not lead to the bracket colliding with the bore of the magnet.

3.4 Experimental set-up and results

QO studies of URhGe for different field directions are performed in the two-axis rotating system described above. The angle dependent magnetoresistance measurements around two axes are made on a single crystal of URhGe with residual resistance ratio (RRR) ≈ 130 for $T \geq 20$ mK and $B \leq 17$ T with a field-calibrated RuO_2 resistance thermometer mounted next to the sample. A standard AC lock-in technique is used to give sensitivity to QO signals of amplitude ≥ 60 nΩ ≈ 3 pV. The measurement current is always below ≤ 100 μA. To verify the in-field thermometry of the set-up on the rotating system, the aligned sample by Laue diffraction is mounted to a stage that was strongly thermally coupled to a zero-field thermometer, which allows the temperatures down to 20 mK. The following data presented were collected and analysed by Dr. Edward Yelland.

Angle dependence of *R(B)* is shown in Figure 3.6 (a) as *B* is rotated from [010] ($\theta = 0°$) towards [001] with $T \approx 100$ mK. On rotating *B* towards [001], the *B*-width

of the zero-resistance regions shrinks continuously to zero at $\theta = 5.5°$. Figure 3.6 (b) shows that by $\theta = 6°$, a Fast Fourier transform (FFT) in 1/*B* of *R(B)* reveals a sharp peak at *F* = 555 T that reaches a maximum amplitude at $\theta = 10°$ where it is visible as a ripple in the raw data.

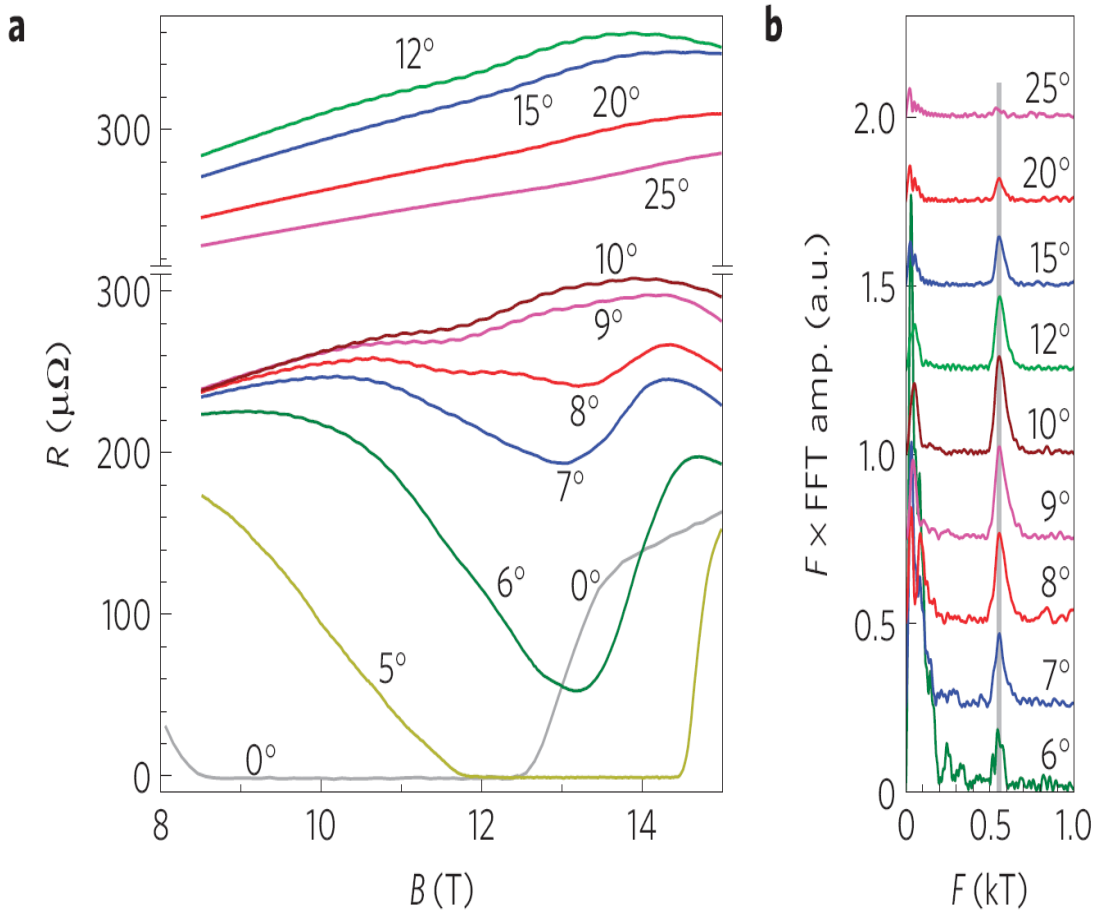

Figure 3.6 (a) Field angle dependence of *R(B)* at $T \approx 100$ mK. (b) Fast Fourier transform of *R(B)* after subtracting a linear background. The oscillations give a shaper peak marked by the vertical line at *F* = 555 T. This reaches maximum amplitude at 10°, where *R* is also maximum before disappearing at higher angles.

A *B*-induced superconducting pocket exists for 8.5 T ≤ *B* ≤ 12.5 T.[2] On rotating *B*, initially the pocket narrows and shifts to higher B; as the SC is suppressed. The

periodicity and *T* dependence of the oscillations are characteristic of QO that occur in clean samples due to the quantization of electronic motion in cyclotron orbits at high magnetic field. QO in resistivity is also called Shubnikov-de Hass (SdH) oscillations and it is principally from the modulation of the electronic scattering rate.[15] A quantum mechanical treatment of electron scattering in high magnetic fields[16] leads to a result that is largely insensitive to the scattering mechanism:

$$\frac{|\tilde{\rho}|}{\rho} \approx \frac{\tilde{\sigma}}{\sigma} = \alpha R_T |\tilde{n}(\epsilon_F)|/n(\epsilon_F)|$$

$$R_T = \frac{2\pi^2 k_B m^* T/e\hbar B}{\sinh(2\pi^2 k_B m^* T/e\hbar B)} \tag{3.7}$$

where $\tilde{\rho}$ and $\tilde{n}(\epsilon_F)$ are the oscillatory parts of the resistivity ρ and Dos $n(\epsilon_F)$ arising from quantization of cyclotron orbits on a single external FS cross-section, α is a number ~ 1 depending on the scattering mechanism and R_T is a damping factor due to thermal broadening of Laudau levels. m^* is the orbit-averaged quasiparticle mass enhanced by the same interactions that enhance the heat capacity. The fundamental component of $\tilde{n}(\epsilon_F)$ is given by the Lifshitz-Kosevich (LK) formula[15]

$$\tilde{n}(\epsilon_F) \propto \frac{B^{\frac{1}{2}} R_D}{\sqrt{\partial^2 \mathcal{A}/\partial k_{||}^2}} \cos[\frac{2\pi F(B)}{B} + \emptyset] \tag{3.8}$$

where $\mathcal{A}$ is the area of the orbit in k-space, *B* is the magnetic induction, R_D is the Dingle factor describing damping due to scattering and $F(B) = \left(\frac{\hbar}{2\pi e}\right)\mathcal{A}(B)$ is the QO frequency. The curvature factor $\partial^2 \mathcal{A}/\partial k_{||}^2$ accounts for the number of k-states that coherently contribute to the oscillatory amplitude at that frequency. For ferromagnets like URhGe opposite spins give rise to QOs with distinct frequencies so the spin interference factor that applies to paramagnetic metals is not present here.

The T dependence of *R(B)* is shown in Figure 3.7 (a,b) at $\theta = 8° \; and \; \theta = 10°$. Figure 3.7 (c) shows the *T* dependence of QO amplitude for the $10°$ data at selected values of *B* is fit by LK formula. The *T*-dependent amplitude at fixed B then gives the quasiparticle mass $m^*(B)$ shown in Figure 3.7 (d). The quasiparticle mass decreases from ~22 m_e at 8 T to ~12 m_e at 15 T. Applying the floating-power fit yields the exponents shown in Figure 3.7 (e): n = 2.0 at zero field but n increase to ~ 2.4 at 8 T before jumping sharply to ~ 3.4 at 13 T and then decreasing again beyond the magnetic crossover field.[4]

Magnetic field dependence of *R* at $T \approx 20$ mK is shown in Figure 3.8 (a) up to 17 T. Figure 3.8 (b) shows the QO component centred on 555T that has been isolated from the B dependent background by subtraction of a smooth function. The observed QO frequency is shown in Figure 3.8 (c). Figure 3.8 (d) shows forms of *F(B)* that are consistent with F_{obs}, different from each other only in the value of the undetermined *B*-linear term.

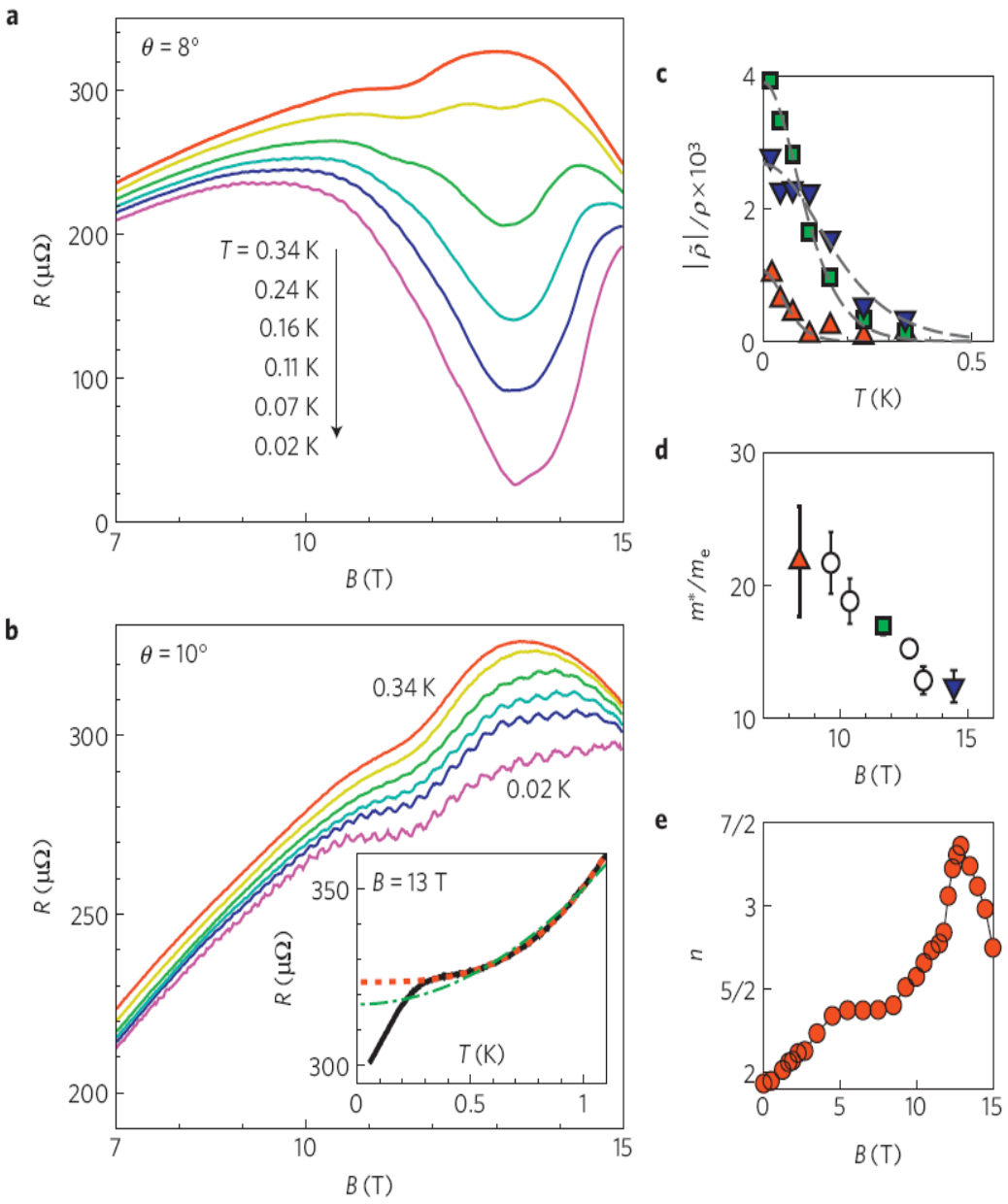

Figure 3.7 Temperature dependence of QO. (a,b): *R(B)* at $\theta = 8°$ and $\theta = 10°$ for various *T*. Inset: *R(T)* at $10°$ and 13 T (solid curve) with fits described in the text. (c) QO amplitude versus *T* for the $10°$ data at selected values of *B* (symbols) and fits to the Lifshitz-Kosevich form (dashed lines). (d) The *B*-dependence of the quasiparticle mass *m** from the fits in (c). (e) Exponent n from fits of *R(T)* to $\rho = \rho_0 + AT^n$ for $0.4 \leq T \leq 1.1$ K at $\theta = 10°$.

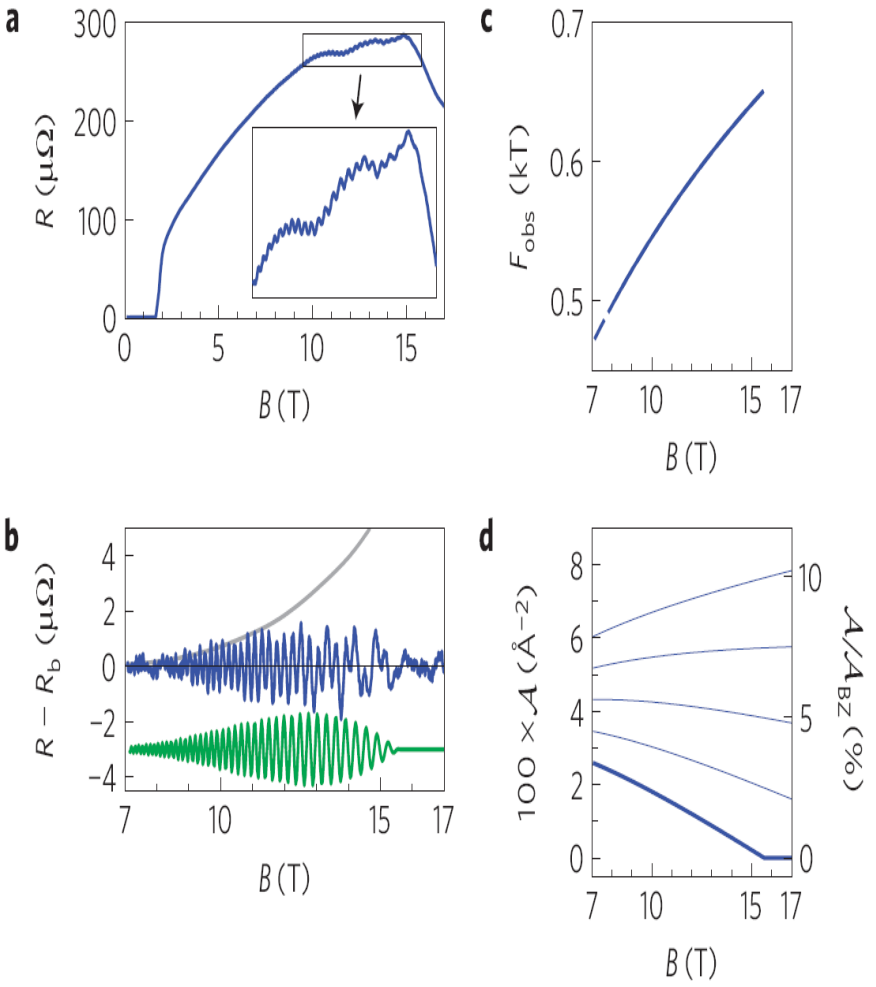

Figure 3.8 Magnetic field dependence of the QO. (a) $R(B)$ at $T = 20$ mK for $B \leq 17$ T and $\theta \approx 10°$. The oscillations disappear suddenly at $B \approx 15.5$ T where the non-oscillatory part of R also drops sharply. (b) Residual after subtracting a smoothly varying background (blue curve) and Lifshitz-Kosevich model calculations for a Fermi surface orbit that shrinks to zero size (green curve) and the amplitude envelope expected for a constant orbit size (grey curve). (c) Observed quantum oscillation frequency $F_{obs}(B)$. (d) Forms of the B dependent Fermi surface area that are consistent with $F_{obs}(B)$. The bold line shows $\mathcal{A}(B)$ vanishing at 15.5 T corresponding to a Lifshitz transition (LT) where a Fermi pocket shrinks to a point or a neck pinches off.

3.5 Conclusions and future work

The novel two-axis rotating system can rotate a sample or a pressure cell about two axes with respect to the direction of the magnetic field. The rotating system has been successfully used to measure the field-angle dependence of *R(B)* and temperature and magnetic field dependence of the quantum oscillations in URhGe. Our results on URhGe provide the first example where the presence of a LT enables phase formation in the vicinity of a QCP, in this case by creating conditions favourable for high-field superconductivity. It remains an open question whether the LT also plays a role in shaping the spectrum of magnetic fluctuations responsible for superconducting pairing in URhGe. This highlights the need for a theory of superconductivity in URhGe that includes the effects of a LT alongside quantum criticality, addressing both the changes to the spectrum of magnetic fluctuations[17] and the existence of critically slow fermionic quasiparticles. More generally, topological transitions of the Fermi surface may be more common than presently thought in narrow-band metals and may offer a route to quantum phase formation that deserves more attention.

In future, in order to reduce the heat from the friction, the pivot material will be replaced by a precision jewel. To study the QO in UGe_2, a miniature pressure cell will be mounted on the rotating system that carries UGe_2 single crystal for angle dependent magneto-resistance measurements under high pressure and low temperature.

This research has led to the following publication:

E. A. Yelland , J. M. Barraclough, W. Wang, K. V. Kamenev and A. D. Huxley, Nature Physics **7**, 890 (2011).

3.6 References

1. D. Aoki *et al*., Nature **413** 613 (2001).

2. F. Lévy *et al*., Science **309**, 1343 (2005).

3. Oxford Instruments provides the technical drawings of the cryomagnet.

4. A. Bhattacharya *et al*., Rev. Sci. Instrum. **69**, 10 (1998).

5. E.C. Palm *et al*., Rev. Sci. Instrum. **70**, 237 (1999).

6. E. Ohmichi *et al*., Rev. Sci. Inst. **72**, 1914 (2001).

7. L. A. Yeoh *et al*., Rev. Sci. Instrum. **81**, 113905 (2010).

8. *NGK Berylco U.K. Ltd*.; web-site: http://www.ngkberylco.co.uk/.

9. O. Kirichek *et al*., Physica B **329-333** 1604 (2003).

10. W. R. Smythe, Static and Dynamic electricity, New York: McGraw-Hill (1950).

11. E.Fromm *et al*., Br. J. Appl. Phys. **16**, 653 (1965).

12. W. Brunst, Die induktive Wärmebehamdlung, Berlin p.42 (1957).

13. A. F. Bangura *et al*., Synth. Met. **153**, 449 (2005).

14. K. V. Kamenev *et al*., High Pressure Res. **27**, 1-189 (2007).

15. D. Shoenberg, *Magnetic Oscillations in Metals*, Cambridge University Press (2009).

16. E. N. Adams *et al*., J. Phys. Chem. Solids **10**, 254 (1959).

17. Y. Yamaji *et al*., J. Phys. Soc. Jpgn. **76**, 063702 (2007).

Chapter 4 The development of a miniature non-magnetic turnbuckle diamond anvil cell

4.1 Introduction

Pressure (*P*) like other thermodynamic parameters such as the temperature (*T*) and the magnetic field (*H*) is a powerful tool that can be used to alter the state and microstructure of the materials. The outcome from this kind of research usually sheds light into the ways of tuning a material to the desired phase such as superconductive state under certain conditions.

There are several commercially available low-*T* and high-*H* systems, for example the Magnetic Property Measurement System (MPMS) and Physical Property Measurement System (PPMS) from Quantum Design (USA) but a versatile high-pressure cell that can be used universally with the existing systems is hard to find, which means custom high-pressure cells need to be designed. Magnetic susceptibility and electrical resistivity are the properties that are often used to detect and study changes of state in materials. Therefore, a universal high-pressure cell is required to be designed which can be used to conduct magnetic susceptibility and resistivity measurements in the MPMS, PPMS and the two-axis rotating stage built for the customized low-*T* and high-*H* systems discussed in chapter 3.

Between all the low-*T* and high-*H* systems mentioned above, the available sample space varies. Therefore, the dimension of the pressure cell becomes crucial because it needs to fit into the rest of the sample environment. Of the three systems mentioned above the MPMS has the smaller sample space of 9 mm in diameter and, therefore,

the pressure cell should be built to match this dimensional restriction.

As it has been mentioned in the Introduction, pressure cells can be divided into two generic categories, piston-cylinder cells and opposed anvil devices. Most of the pressure cells designed for the MPMS are of piston cylinder type[1-8] because relatively large sample volume can be accommodated in them but the main disadvantage of the piston-cylinder type cells is that the maximum pressure achievable in them is under 2 GPa. In order to reach the pressure of more than 2 GPa, opposed anvil devices are often a good choice although the sample volume in them is significantly smaller. The following chapter will briefly explain the working principle of a Diamond Anvil Cell (DAC) and review the existing miniature opposed anvil devices.

4.2 Review of existing miniature opposed anvil devices for use in the low-*T* and high-*H* system

DAC, a typical example of an opposed anvil device, is a good application of technique and is used to generate very high pressures on a small volume sample. The working principle of DAC has been described in Chapter 1. The pressure measurement in DAC by using ruby fluorescence is introduced below. A ruby chip placed next to the sample is used to measure the pressure on the sample. The pressure is determined by detecting the change in the position of the R_1 peak in the spectrum of ruby which shifts almost linearly with pressure, with the coefficient $dP/d\lambda = 0.2746$ GPa $Å^{-1}$.[9]

In order to avoid the interference from the body material of high-pressure cells, the DAC for magnetic susceptibility measurements is made of non-magnetic materials. Non-magnetic copper beryllium (CuBe) alloy was used building construction of the first diamond anvil cell for MPMS magnetometer in 2001 by Mito *et al.*[10] The

diamond anvils of this DAC can be adjusted in X and Y directions and the dimension of the cell is 8.5mm in diameter and 35mm in length. The pressure capability of the cell depends on the culet size of the diamond and measurements at pressures of up to 15 GPa have been reported. A similar design of MPMS DACs have been proposed by Alireza *et al.*[11,12] The major difference between Alireza's and Mito's designs is the alignment mechanism. Alireza's design can only align the diamond anvils in X and Y direction and there is no rocking support. In order to improve the signal-to background noise of the magnetic susceptibility measurements, Alireza's pressure cell is made of ultralow susceptibility materials such as ultrapure CuBe and copper titanium (CuTi) alloy and the amount of the cell material around the sample has been kept to a minimum. The diameter of this DAC is 8.4 mm and the length is 64mm, i.e. almost twice the length of the Mito's cell. Recently non-magnetic anvils made of a composite ceramic material have been used in the construction of a miniature opposed anvil PRESSURE cell for SQUID measurements.[13] The cell can reach the maximum pressure of 7.6 GPa with 0.6 mm culet. The length of the cell is over 70mm and the diameter is 8.7mm. Because the space on the two-axis rotating stage is about 30mm in diameter by 20mm in height, all the cells designed for MPMS discussed above are too long to fit on it.

Several miniature DACs have been developed for ^{3}He PPMS. In 2007, Kamenev *et al.* reported a miniature diamond anvil cell designed for ^{3}He insert into PPMS.[14] The cell is made of non-magnetic CuBe alloy and capable of reaching 10 GPa. The shape of the cell resembles the uppercase letter 'D', a half cylinder with 26 mm in diameter and 18mm in height. The dimension of the cell makes it possible to use with the two-axis rotating stage that is built for the customized low-*T* and high-*H* system but it is too large to be used with the MPMS because the bore of the sample space in MPMS is smaller than 9 mm in diameter. Miniature DACs designed for broad range of high pressure measurements was reported by Gavriliuk *et al.* in 2009.[15] The cell is

made of hardened non-magnetic nickel chromium aluminium (NiCrAl) alloy and the wide-angle side windows provide the possibility to use this cell in synchrotron measurements. Albeit this cell is claimed to reach more than 100 GPa, the smallest version of this cell is about 12.7 mm in diameter, which means this cell is also too big to fit into MPMS. The commercially available pressure cells sold by easyLab Ltd. for use in MPMS also do not meet the selection criteria due to the dimensional limitations.

It seems that the existing pressure cells designed for MPMS are too long to fit to our two-axis rotating stage while the pressure cells designed for PPMS are too big to fit into MPMS. Yet, it is highly desirable for high-pressure characterisation of the material to measure several of its physical properties at exactly the same pressure, i.e. in the same pressure cell. The design and operation of a versatile miniature pressure cell is described in the following chapter, which can fit in MPMS, PPMS and the two-axis rotating stage built for the customized low-*T* and high-*H* systems and described in Chapter 3.

4.3 The Design and operation of the pressure cell

In order to minimize the dimensions of the DAC, the design of the pressure cell is based on the turnbuckle principle, which was applied to build cells for electrical resistivity measurements, some of which are made of hard plastic material for use in pulsed magnetic fields.[16-19] The construction of the pressure cell is shown in Figure 4.1. The cell is 7 mm long and approx. 7 mm in diameter. It consists of a body and two end-nuts and is made of fully heat-treated CuBe alloy. The body of the cell is a cylinder with flats made for ease of gripping. The end-nuts are identical except that one has a right-hand external M5 × 0.5 thread and the other – the left-hand thread. Four 0.8 mm diameter holes are machined in the sides of the cylindrical body for

viewing the anvils and the gasket. Guiding holes are drilled at the outer ends in both end-nuts and diamond anvils are attached to the other end by means of Stycast epoxy (2850 FT with catalyst LV 7).

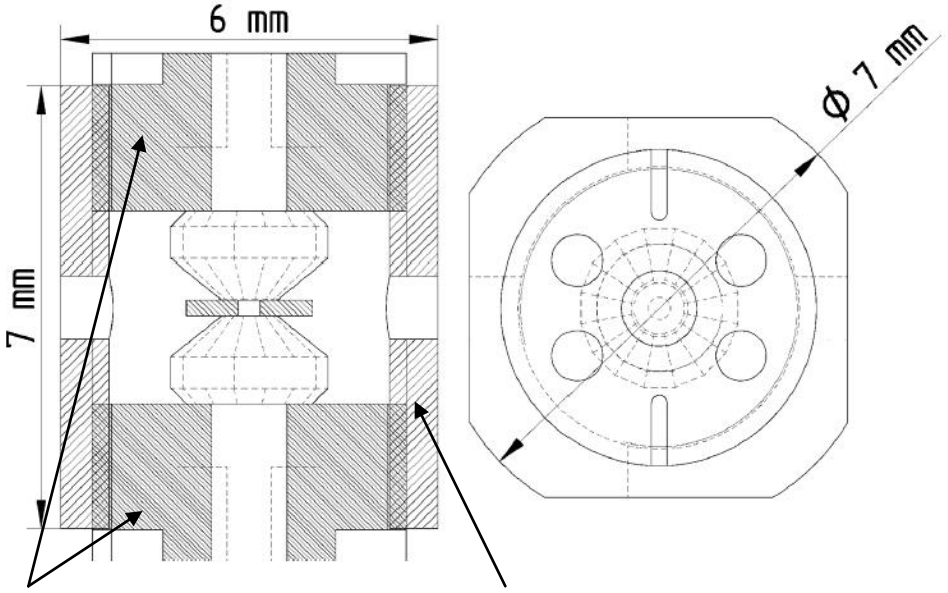

Figure 4.1 The construction of the pressure cell for magnetization measurements

The parts of the cell are shown in Figure 4.2. During the assembly of the pressure cell the culets of the diamonds are made coaxial with the viewing hole in the nut. The alignment relies on the precision machining of the end-nuts and the body of the cell, and there is no additional alignment mechanism.

The gasket material for use in this pressure cell is annealed BERYLCO 25 foil. In order to achieve pressure in excess of 10 GPa, the diamonds with 800 μm culets is used. To reach a pressure around 10 GPa, the gasket is usually pre-indented from 250 to 100 μm. With a hole of 350 μm in the gasket, the initial sample volume is about 0.01 mm^3.

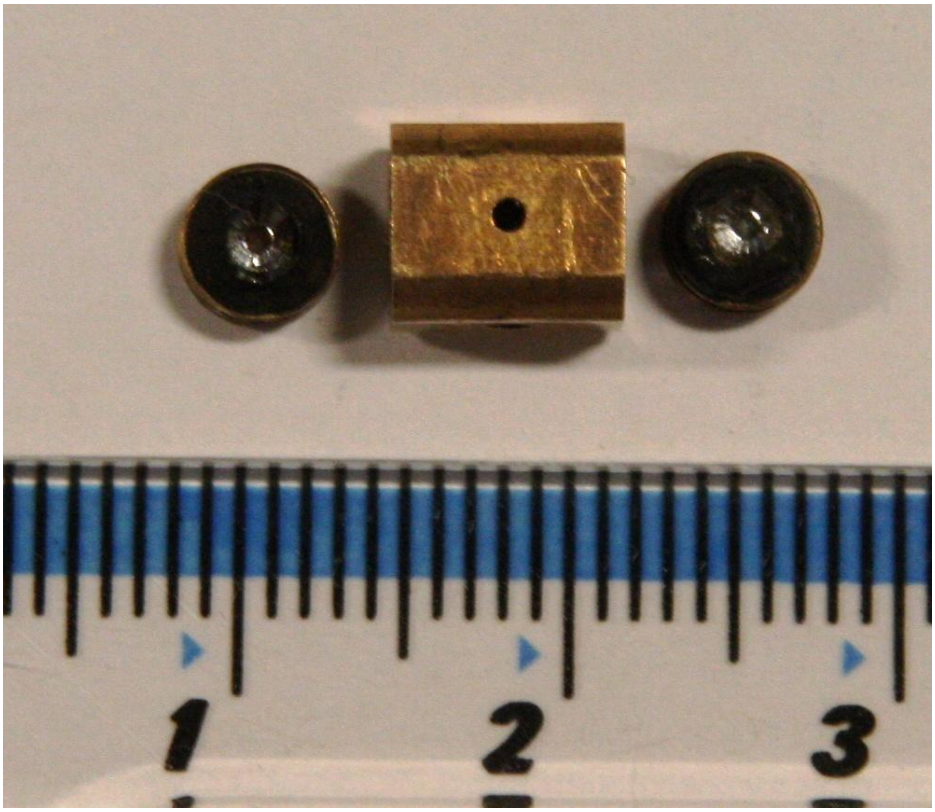

Figure 4.2 Parts of the pressure cell

To make the pressure cell suitable for electrical resistivity measurements two additional features have been introduced. Two feed-through holes of 0.5 mm in diameter are made in each end-nut as shown in Figure 4.3. It allows the electrical connection wires originating on the sample to reach the connectors of the measurement system when the cell is used for resistivity measurements. In order to mount the cell onto the two-axis rotating stage, two M1.6 thread holes replaced two out of four side holes (Fig. 4.3.(a)).

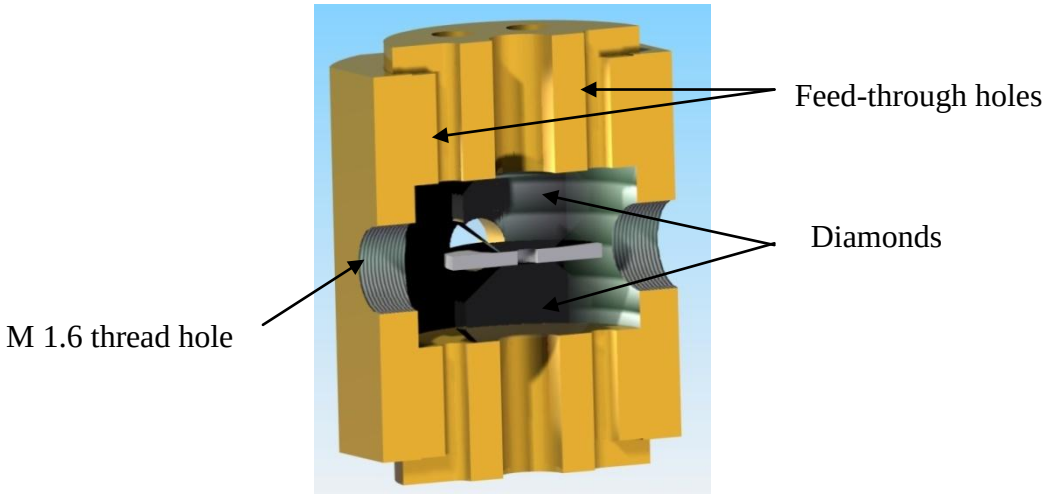

(a)

(b)

Figure 4.3 (a) Section view of the pressure cell for resistivity measurements, (b) the photo of the pressure cell.

Once the sample, pressure medium and manometer is loaded, the pressure cell is placed into a customized bracket shown in Figure 4.4(a) for changing the pressure. The bracket has four pins that engage into the four holes in both end-nuts. The top pins can slide vertically to allow the pressure cell to be put into the bracket as well as making sure the pins are fully engaged into the guiding holes of the end-nuts. When the pins are engaged, the end-nuts can only move vertically when the body of the cell is rotated. Lower pressure can be obtained by simply rotating the body of the cell

while it is mounted in the bracket. However, for higher pressures, a hydraulic press is required to overcome the friction on the thread between the cell body and the end-nuts. To make sure that the load can be increased in fine steps, a sensitive load cell is used to monitor the force acting on the end-nuts. Once the desired pressure that can be checked by using ruby fluorescence method is reached, the cell is ready to be mounted onto the standard sample holder in the measurement system. Figure 4.4 (b) shows the cell fit into an MPMS straw.

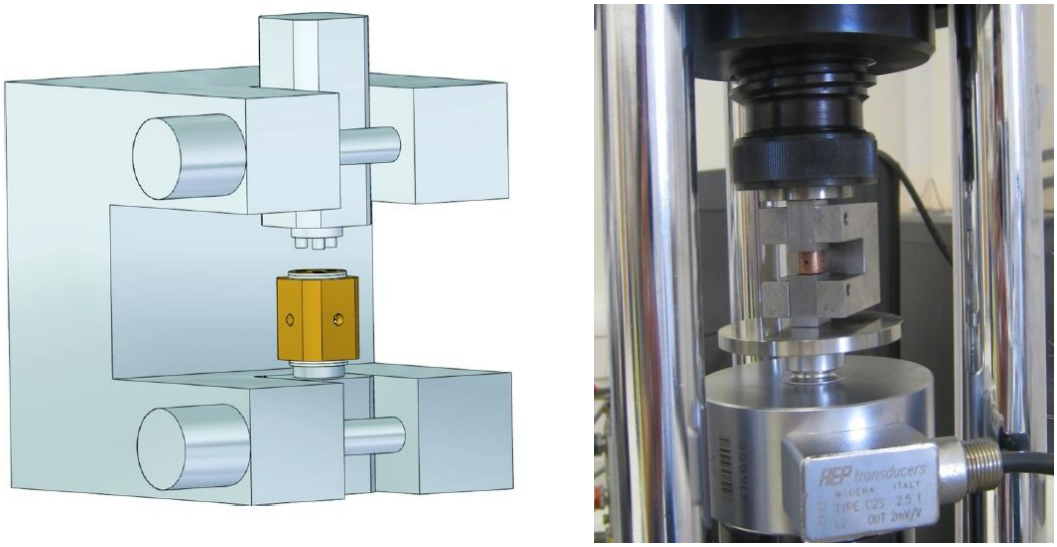

(a)

(b)

Figure 4.4 (a) CAD drawing of the bracket for applying load to the pressure cell and the cell is loaded into the press. (b) The assembled cell is adapted in a standard plastic straw for use in MPMS.

4.4 The design and tests of the universal gearbox

Daphne 7373 oil is often used as the pressure-transmitting medium but it becomes non-hydrostatic above 2.3 GPa.[20] According to Klotz's research, argon and helium can remain hydrostatic up to 10 GPa.[21] Therefore, a universal gearbox has been designed for loading either helium gas or liquid argon into the sample chamber to achieve more hydrostatic conditions on the sample. The gas-loading system available at the University of Edinburgh is shown in Figure 4.5.

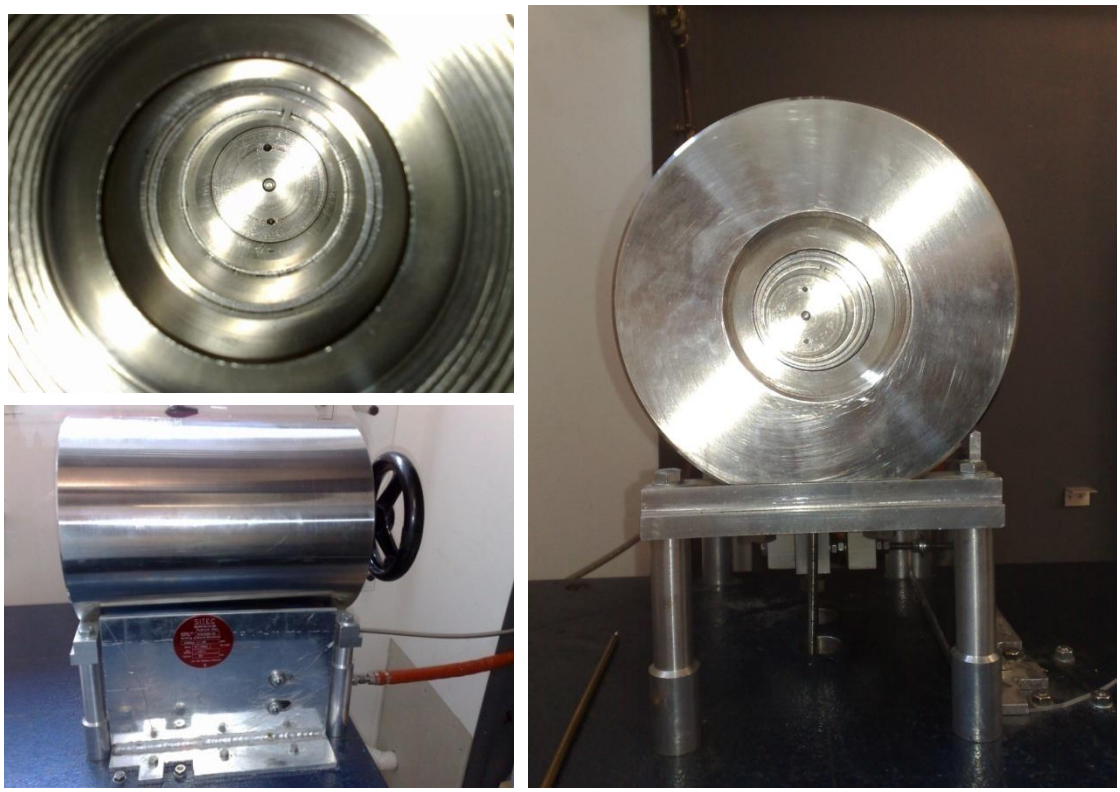

Figure 4.5 The gas-loading system.

The gas loading device is a pressure chamber connected to a single-stage gas compressor, which can generate pressures of up to 2 kbar.[22] Once the desired pressure has been achieved inside the gas loader, the pressure cell can be closed and then taken out of the apparatus. Figure 4.5 shows there is a sealed shaft through one

end of the cylindrical body of the gas loader. At one end it has a wheel mounted on it (Fig. 4.5, bottom left) which terminates with a hexagonal shaft on the inside of the gas-loading system (Fig. 4.5, bottom right). There are also two guiding pins which are symmetrically located on either side of the shaft. The two pins are used to hold the body of a pressure cell with which it is used in place and the shaft rotates a nut on the cell pushing one anvil inside the cell against the other.

In order to engage with those two features in the gas-loading system described above, a gearbox with the gear ratio of 3.2:1 has been designed. The assembly of the gearbox and pressure cell is shown in Figure 4.6. The idea of this gearbox is to turn the cell body by using gears and to lock the gas as the pressure medium inside the gasket between the diamonds. The gearbox consists of the body, two holding brackets, one pinion, one gear, 4 spacers and a shaft. The square slot is made in the centre of the gear, which allows the gear to grip the flats on the cell body. A hexagonal profile is cut in the centre of the pinion for gripping the shaft tightly. Spacers are used to stop the gear and pinion moving out of plane of rotation. The shaft is not shown in Figure 4.6 (a) since the setup for cryo-loading and gas-loading is different. Therefore, the size of the shaft differs but the hexagonal part that inserts into the pinion remains the same.

The principle of the cryo-loading is based on the difference of the boiling temperature between argon (87.3 K) and nitrogen (77 K). The gearbox designed for the gas-loading system can also be used in the cryo-loading system shown in Figure 4.7. The operation of the cryo-loading consists of three steps. Firstly, the cryo-loading system sitting into a high sided foam box is cooled by liquid nitrogen until the temperature reaches 77 K, which can be known when the liquid nitrogen stops boiling and no frost is formed on the gearbox assembly. The liquid argon is then poured into the gearbox assembly. Finally, the shaft is turned by a spanner to

trap the argon in the gasket hole. This step should be finished within 2 minutes because the argon usually starts to boil after that.

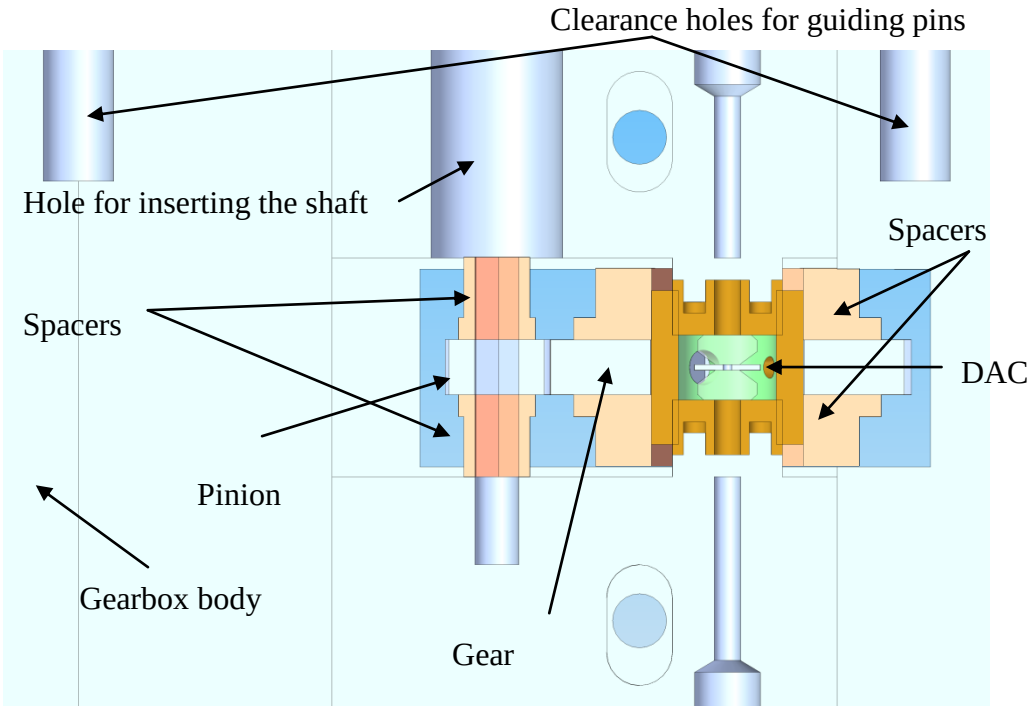

(a) Section view of the assembly.

(b) The parts of the gearbox.

Figure 4.6 A universal gearbox for gas and cryogenic liquid loading.

Figure 4.7 shows the assembly of the gearbox for gas-loading and cryo-loading, respectively.

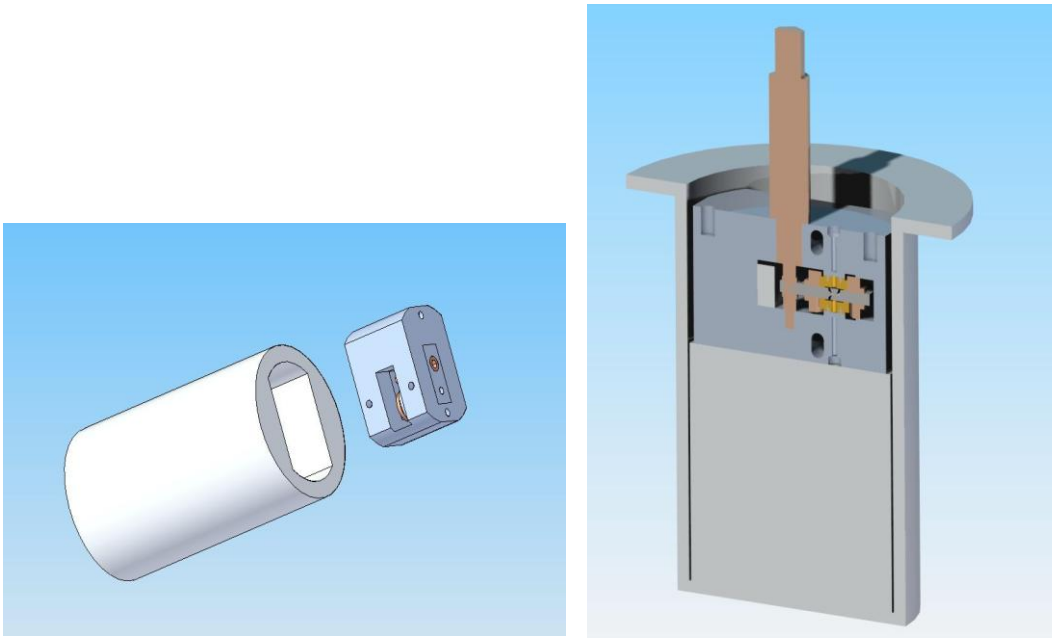

Figure 4.7 CAD drawings (a) The assembly of the gearbox for gas-loading. The large aluminium can on the left is used as the gas displacer inside the gas loader. (b) The assembly of the gearbox for cryo-loading.

In order to demonstrate the function of the gearbox we show the results of the test in which gaseous argon was loaded into the DAC using the gas-loading system and the pressure was then increased to 6.3 kbar. Figure 4.8 shows the shift in the intensity of the ruby excitations vs. the wavelength of 3 series data.

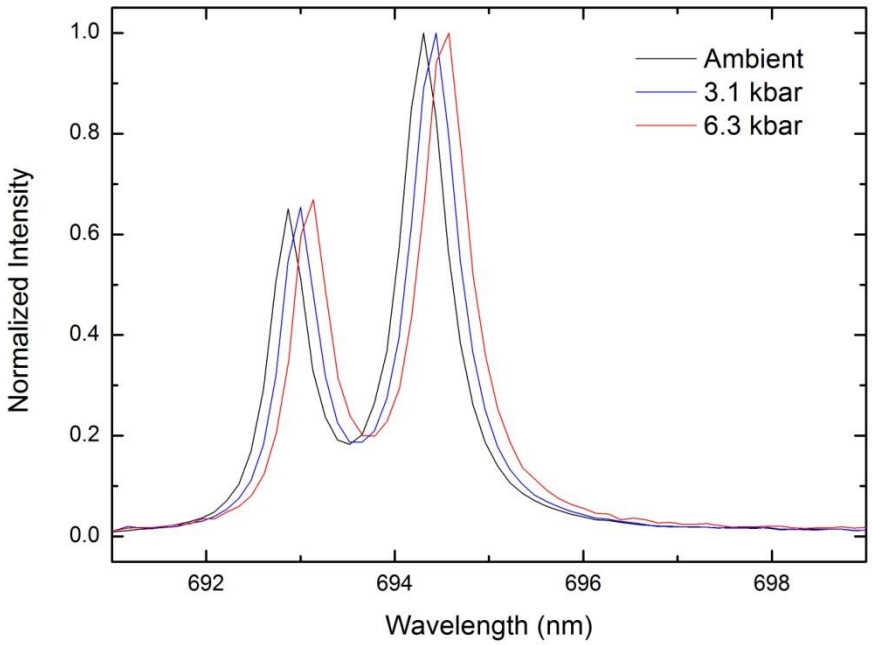

Figure 4.8 The normalized intensity vs. wavelength for argon pressure medium at 0, 3.1 kbar and 6.3 kbar.

As can be seen in Figure 4.8, as the pressure increases, the peak does not get broadened, which indicates the pressure is hydrostatic. This demonstrates the performance of the gearbox.

4.5 Tests and results

The cell for magnetization measurement is symmetric with respect to the sample. The dimensions of the cell are also similar to those of a standard MPMS sample, which means the cell can produce a symmetric response of the voltage measured through the SQUID element as shown in Figure 4.9. The resulting integrated

magnetization calculated by the MPMS software is 1.07×10^{-5} emu. The symmetric response remains true for all applied magnetic fields.

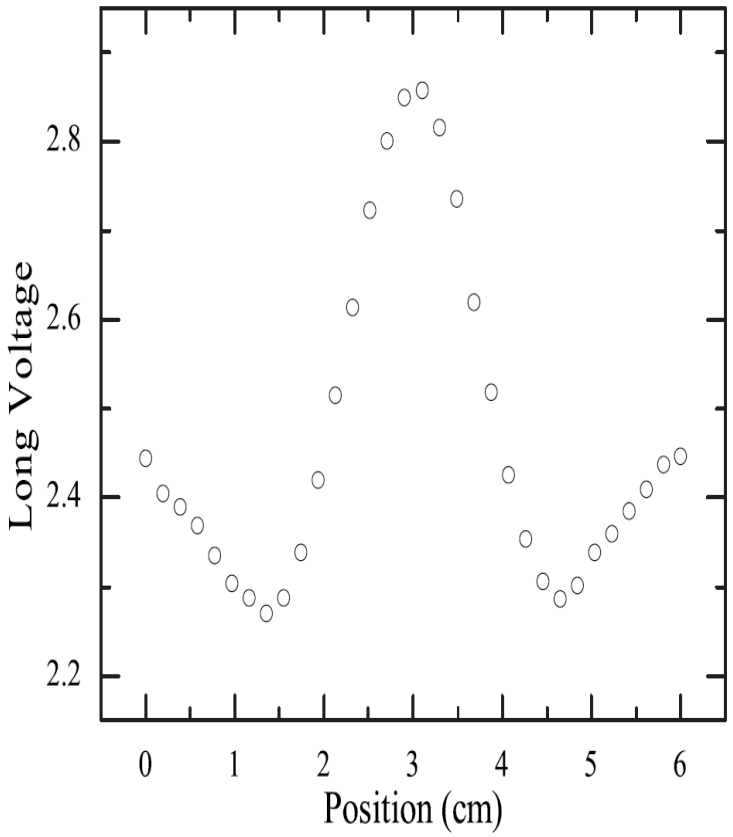

Figure 4.9 Raw MPMS data generated by a scan of the empty pressure cell over a 6 cm distance in an applied field of 20 Oe at 300 K.

The cell weighs about 1.5 g and it can be cooled at a rate of 1 K per minute and thermal equilibrium can be reached in 2 minutes in the MPMS. The magnetization of the empty cell as a function of temperature at different magnetic fields is shown in Figure 4.10. Those curves are smooth and follow the features of the known trend for BERYLCO-25 alloy. Those curves are recorded before the measurement with the sample and the data are used for background correction.

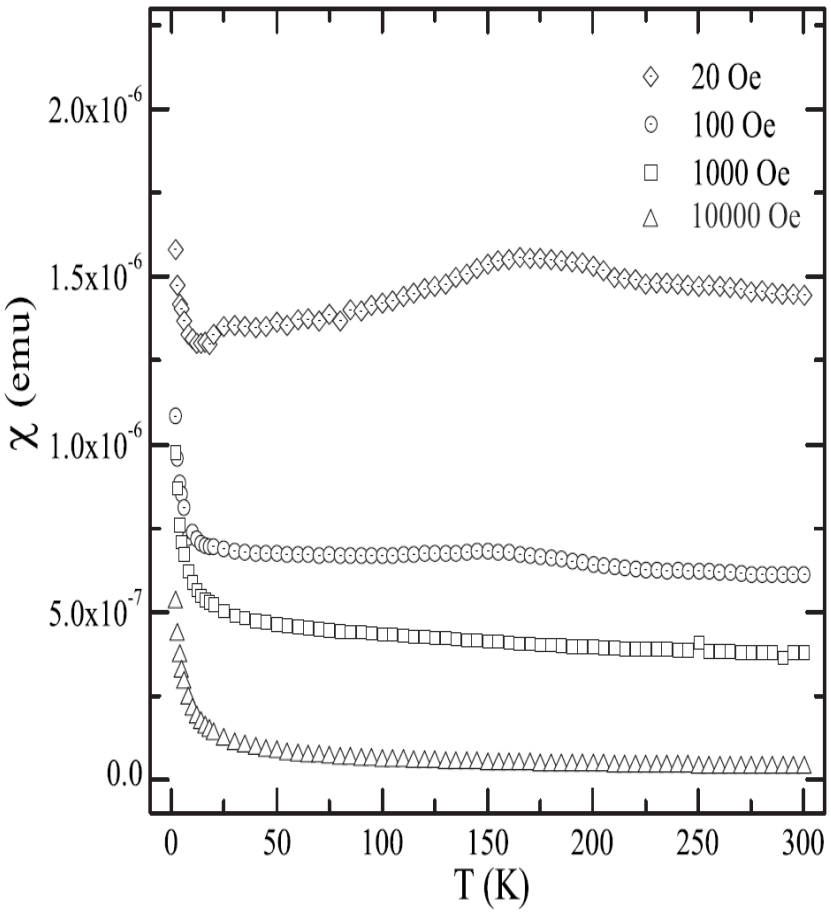

Figure 4.10 The temperature dependence of the magnetization of an empty pressure cell.

To check if the pressure changes in the cell during the cooling, ruby and lead were both loaded into the sample space. The pressure at room temperature was measured by means of ruby fluorescence and at low temperature (3-7 K) lead was used by following T_c for the same loading and taking the value of d T_c/dP = 0.365 K/GPa.[23] Figure 4.11 shows the pressure remains the same at low temperature as at room temperature. The solid line shows $P_{\text{lead}} = P_{\text{ruby.}}$ The errors in determining the pressure are $\pm$ 0.03 GPa for lead and $\pm$ 0.02 GPa for ruby. The error bars are not visible since they are smaller than the symbols on the graph.

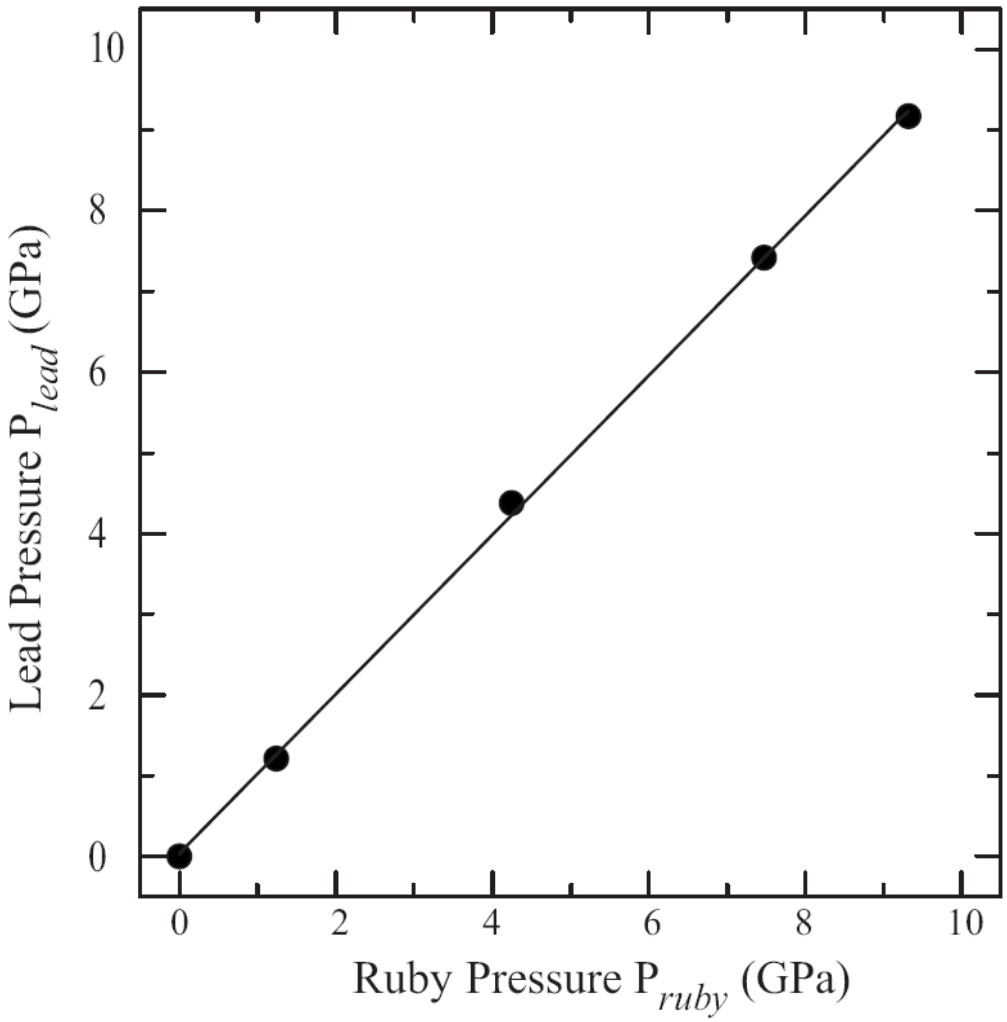

Figure 4.11 The pressure P_{lead} determined at the superconducting transition in lead at low temperature ($T \approx 3 - 7$ K) vs. the pressure P_{ruby} acquired from the ruby fluorescence at room temperature ($T \approx 295$ K).

In order to demonstrate the performance of the cell, Gaétan Giriat performed a high pressure study of a ferromagnetic material, $Mn_3[Cr(CN)_6]_2 \cdot xH_2O$ and the results are presented in the following paragraph. In this measurement, the value of x in the sample is 16. Pressure applied to the sample was increased in small steps. Figure 4.12 shows the magnetic susceptibility as a function of temperature. The data was

collected on warming after cooling down in field. The inverted triangle series data are collected finally after the release of the pressure. The curves presented in the graph are corrected for the cell background. To illustrate the sensitivity of the measurement the left axis shows the susceptibility in emu while the right axis shows the susceptibility normalized by the mass of the sample $m = 7.5 \times 10^{-6}$ g. The value of the mass is estimated from the comparison of the measurements performed at ambient pressure on the sample in a plastic straw and in the cell.

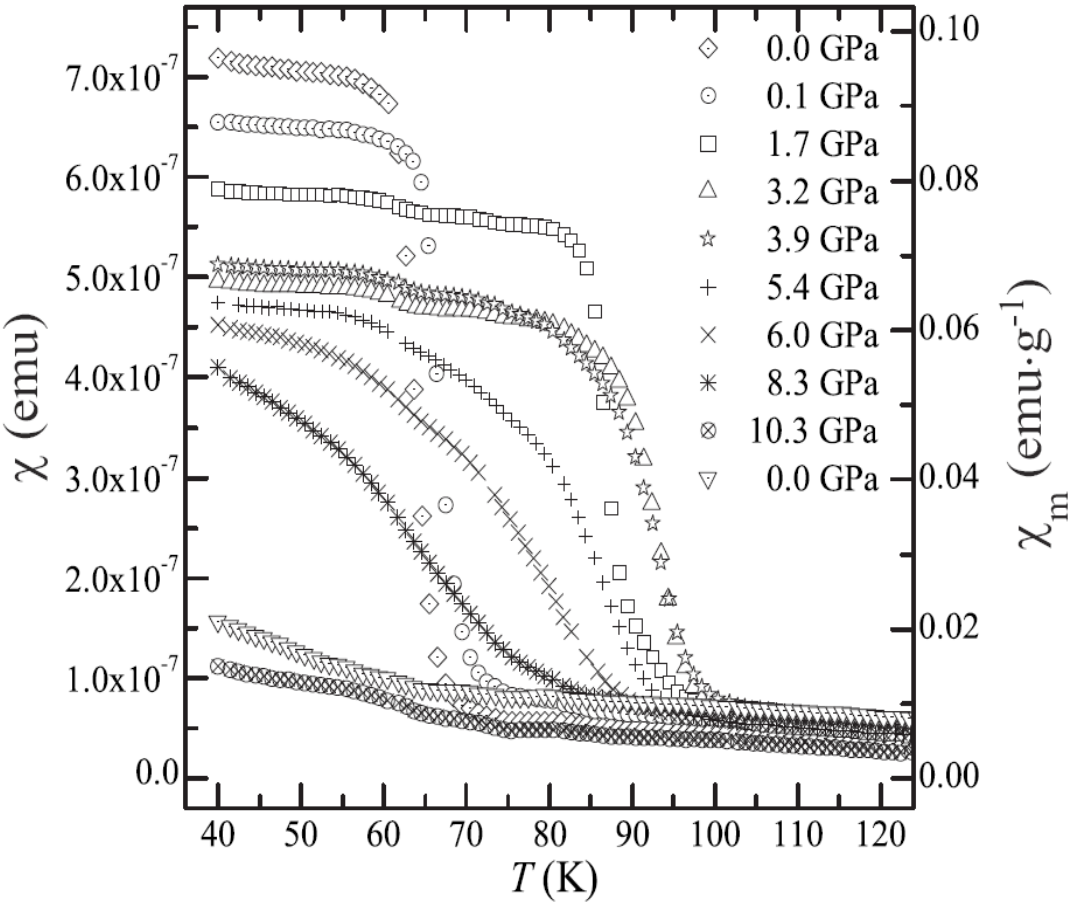

Figure 4.12 The temperature dependence of the magnetic susceptibility of $Mn_3[Cr(CN)_6]_2 \cdot xH_2O$ in a 100 Oe field at different pressures.

A small feature is noticeable around 60 K in all the data and its magnitude and

position are not affected by applied pressure and the temperature at which is observed corresponds to the Curie temperature T_c of the $Mn_3[Cr(CN)_6]_2 \cdot xH_2O$ at ambient pressure. Therefore we believe this feature is due to a small amount of the sample left outside the pressurized volume of the cell after loading into the gasket hole.

The pressure variations of T_c, derived from the maximum of dx/dT, and $\Delta x_m = x_m$ (40 K) - x_m (120 K), taken as being proportional to the ferromagnetic moment, are shown in Figure 4.13.

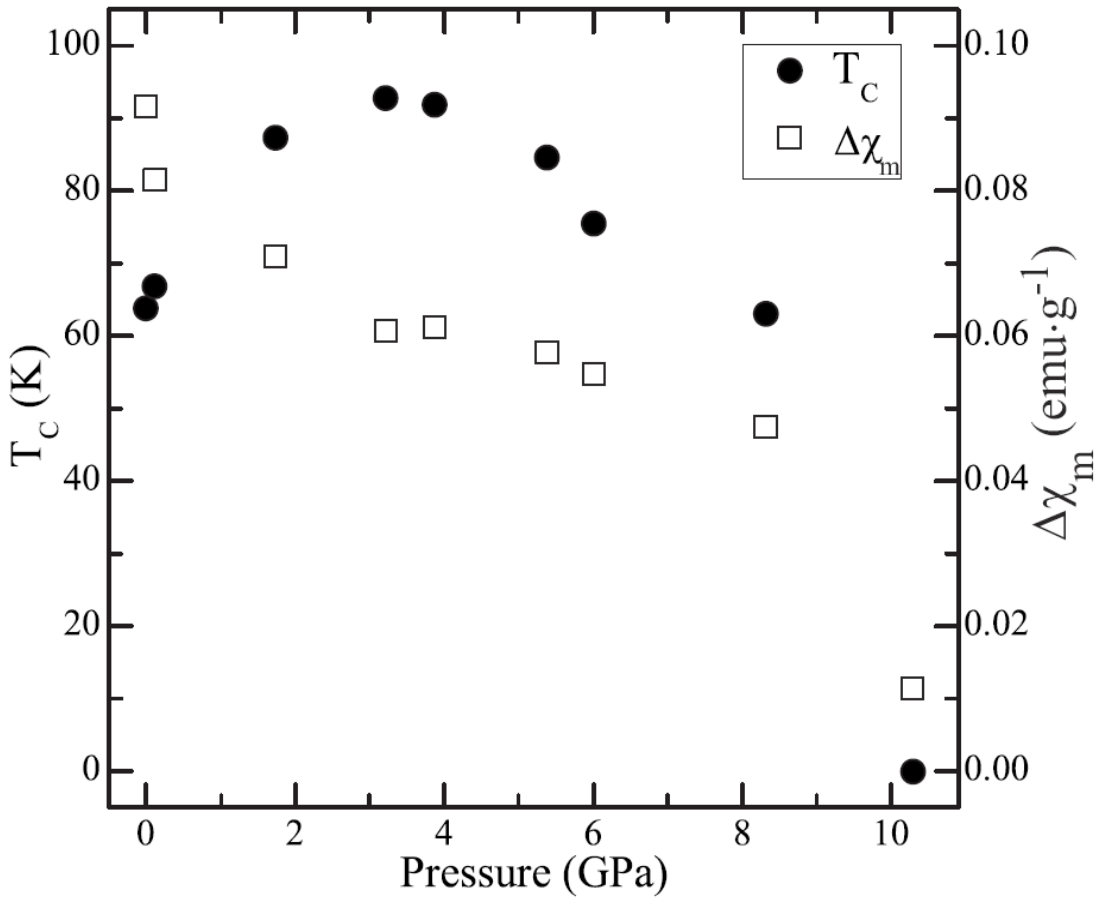

Figure 4.13 The pressure vs. temperature magnetic phase diagram of $Mn_3[Cr(CN)_6]_2 \cdot xH_2O$.

Below 1 GPa, dT_c/dP = 25 K/GPa is similar with the values reported in two previous studies.[24] At higher pressures, a large but non-linear increase in T_c from 63 K at ambient pressure to a maximum T_c = 93 K at 3.2 GPa pressure is discovered. An enhancement of the super-exchange interactions between the transition metal cations is reflected as the bonds to cyanide are shortened with pressure. The ferromagnetic moment decreases while T_c is enhanced, which shows the evidence of increased tilting of the $Mn(CN)_6$ and $Cr(NC)_6$ octahedra. The magnetic transition becomes even broader when the pressure is over 3.2 GPa. The T_c is suppressed to when the sample is subjected a pressure of about 10 GPa. A corresponding collapse of the ferromagnetic moment confirms the change of the T_c. This matches to a pressure-induced amorphization of the sample, as was observed in a similar PBA, $FeCo(CN)_6$ between 8 and 10 GPa.[25] They reports that the ferromagnetism of $Mn_3[Cr(CN)_6]_2 \cdot nH_2O$ does not recover when the pressure in the pressure cell is released from 10 GPa. The last zero pressure point in Figure 4.13 consolidate this conclusion. In future, a structural study of this sample up to 10 GPa will be required to confirm that conclusion.

4.5 Conclusions and future work

A miniature pressure cell based on the turnbuckle principle that can be used in PPMS, MPMS and a two-axis rotating stage built for a customized low-T and high-H system has been designed, constructed and tested. The pressure cell can reach a pressure in excess of 10 GPa which is demonstrated by the magnetization measurement of $Mn_3[Cr(CN)_6]_2 \cdot xH_2O$. The small size of the cell allows it to be cooled quickly and shows very low background in the magnetization measurements. The weight of the cell is only 7 g, which makes it perfect for use on the two-axis rotating stage for resistivity measurements since the maximum weight allowance of each rotator is 100

g. To ensure the hydrostatic pressure is applied to the sample, a gearbox that can be used for loading both liquid argon and helium gas has been designed and manufactured and tested.

In future, the pressure cell will be deployed for electrical resistivity measurements in the two-axis rotating stage built for the customized low-*T* and high-*H* system as shown in Figure 4.14. High pressure quantum oscillation study of UGe_2 will be performed in this measurement system.

Figure 4.14 A CAD drawing of the pressure cell mounted on the two-axis rotating stage for low-*T* and high-*H* measurements.

The work in this chapter leads to the following publication:

G.Giriat, W. Wang, J. P. Attfield, A. D. Huxley, K. V. Kamenev, Review of Scientific Instruments, **81**, 073905 (2010).

4.6 References

1. S. Reich *et al*., Meas. Sci. Technol. **7**, 1079 (1996).

2. J. Diederichs *et al*., Phys. Rev. B **54**, R9662 (1996).

3. Y. Uwatoko *et al*., Rev. High Pressure Sci. Technol. **7**, 1508 (1998).

4. K. Kamishima *et al*., Rev. Sci. Instrum. **72**, 1472 (2001).

5. J. Kamarád *et al*., Rev. Sci. Instrum. **75**, 5022 (2004).

6. See: http://www.easylab.co.uk/ for Mcell 10 and Mcell Ultra pressure cells manufactured by easyLab Technologies.

7. K. V. Kamenev *et al*., Rev. Sci. Instrum. **77**, 073905 (2006).

8. Y. Uwatoko *et al*., J. Phys.: Condens. Matter **17**, S1011 (2005).

9. J. D. Barnett *et al*., Rev. Sci. Instrum. **44**, 1-9 (1973).

10. M. Mito *et al*., Jpn. J. Appl. Phys., Part 1 **40**, 6641 (2001).

11. P. L. Alireza *et al*., J. Phys. Soc. Jpn. **76**, 216 (2007).

12. P. L. Alireza *et al*., Rev. Sci. Instrum. **80**, 023906 (2009).

13. N. Tateiwa *et al*., Rev. Sci. Instrum. **82**, 053906 (2011).

14. K. Kamenev *et al*., High Press. Res. **27**, 189 (2007).

15. A. G. Gavriliuk *et al*., Rev. Sci. Instrum. **80**, 043906 (2009).

16. M. Kano *et al*., J. Phys. Soc. Jpn. **76**, 56 (2007).

17. W. A. Bassett, High Press. Res. **29**, 163 (2009).

18. C. Martin *et al*., J. Low Temp. Phys. **138**, 1025 (2005).

19. L. Chen *et al*., J. Phys. Soc. Jpn. **76**, 58 (2007).

20. K. Yokogawa *et al*., Jpn. J. Appl. Phys. **46**, 6A, pp.3636 (2007).

21. S Klotz *et al*., J. Phys. D: Appl. Phys. **42** 075413 (2009).

22. A. Kurnosov *et al*., Rev. Sci. Instrum. **79** 045110 (2008).

23. A. Eiling *et al*., J. Phys. F: Met. Phys. **11** 623 (1981).

24. M. Zentková *et al*., J. Phys.: Condens. Matter 19, 266217 (2007).

25. J. Catafesta *et al*., Phys. Rev. B **77**, 064104 (2008).

Chapter 5 Calorimetric and high pressure resistivity study of PrNi

5.1 Introduction

A ferromagnetic transition in CrB-type orthorhombic single crystals of PrNi at ~20.5 K was discovered by magnetic susceptibility measurements in 1984.[1] Like other external factors such as the magnetic field, pressure is a powerful tool that is often used to probe the quantum phase transitions of some ferromagnetic materials such as UGe_2 and $CePd_2Si_2$.[2,3] High pressure resistivity studies on PrNi in a piston-cylinder high pressure cell by Matas *et al.* in 2008 suggest applied pressure up to 1 GPa can shift the Curie temperature (T_C) of PrNi to higher temperatures at the rate of 1 K/GPa.[4] However, the pressure (> 1 GPa) effects on the T_C and the magnetic properties of PrNi are unknown. If the trend could be reversed and T_C of PrNi could be suppressed to zero under some pressure above 1 GPa, it would be possible to access a quantum critical transition, which it would be of great interest to investigate.

The data from the heat capacity (C_p) measurement of solids provides comprehensive information about the lattice, electronic and even magnetic properties of materials. However, conducting precise heat capacity measurements under high pressure poses a lot of challenges mainly because of the presence of the pressure-transmitting medium. Resistivity measurements are somewhat easier to make and the data can be used to extract the information about C_p . Fisher and Langer reported the resistive anomalies that are known to occur in the rare-earth metals and can be related to the magnetic specific heat.[5] This has been confirmed by Stishov *et al*. in observing the phase transition in MnSi, in which the unified temperature dependence of C_p, the

temperature (T) derivative of resistivity ($d\rho/dT$) and the linear thermal expansion coefficient is presented.[6] Since the magnetic heat capacity can be extracted from the C_p and the methodology of conducting high pressure resistivity measurement is well established, the variation of high pressure magnetic specific heat and magnetic entropy in the ordered state of some rare earth compounds can be studied by investigating the change of $d\rho/dT$ under pressure. A high pressure up to 9 GPa resistivity measurements on a single crystal of PrNi in a diamond anvil cell (DAC) and heat capacity measurements at ambient pressure are reported in the following sections. The critical transition temperature of PrNi under different pressures up to 9 GPa is presented and the change of the magnetic heat capacity and entropy in the ordered state under pressure is estimated and discussed.

5.2 Experimental

5.2.1 Heat capacity measurement

A high purity single crystal of PrNi was grown by Dmitry Sokolov using the Czochralski method in ultra high vacuum. The ratio of residual resistance (RRR), which is usually used to describe the purity of the sample, is 125. The sample for both heat capacity and resistivity measurements was cleaved from a large PrNi single crystal. The heat capacity was measured in the Physical Property Measurement System (PPMS) from Quantum Design based on a pulse relaxation method and C_p versus temperature (T) was recorded between 0.35 and 121 K.

5.2.2 High pressure resistivity measurements

The resistivity of PrNi at ambient pressure was measured in a standard puck of the PPMS system. Electrical resistivity at high pressure was measured in the temperature

range of 1.8-300 K by means of a four probe method in the PPMS using a non-magnetic diamond anvil cell (DAC)[7] designed for use with the PPMS ^{3}He insert. In this apparatus, a direct current (DC) is used and the value of the excitation current is 5 mA. Daphne 7373 oil was used as a pressure-transmitting medium.[8] The pressure applied to the sample was measured by the ruby fluorescence method. Measuring electrical resistivity in DACs poses several challenges such as insulating the metallic gasket from the conducting sample and making contacts to a tiny sample. Details on how to setup the resistivity measurements are given below.

A pair of single-bevelled diamond anvils with 0.8 mm culet was used in the DAC. The diamond anvils are cleaned and aligned before loading the sample. A 250 μm thick stainless steel gasket is indented to 50 μm in a DAC. A hole of 200 μm in diameter is then drilled in the centre of the indentation by a electrical discharge drilling machine and a set of small mechanical drills with diameters in the range of 250-400 μm are used to enlarge the hole to 400 μm. The metallic gasket is cleaned in an ultrasonic bath afterwards to remove any metal burrs or powder. The next step is to insulate the metallic gasket from the samples and electrodes. A thin layer of the mixture of alumina powder of uniform 1 μm grain size and Stycast 1266 epoxy in a weight ratio of 3:2 is applied onto the surface of the pre-indented gasket. The gasket is placed into a furnace for 20 minutes at 70 ℃ for the coating to dry. After the initial curing, the gasket is placed into the DAC. In order to embed the alumina into gasket and create a uniform insulation layer on the gasket and the same force that used to indent the gasket is applied. Further curing of the mixture is done in a furnace for two hours at 70 ℃. Since the mixture also covers the 400 μm hole drilled earlier, a set of drills up to 350 μm in diameter are used to open up the filled hole but leave a thin layer of mixture that insulates the rim of the hole from the contacts wired to the sample.

The sample loaded into the DAC is 150 μm by 100 μm and 10 μm thick. Four 10 μm annealed gold wires are spot-welded to the single crystal sample and 10 μm thick gold foil is used as secondary leads. The gold foils are glued on the side of the diamonds using DuPont conductor paste 4929N. Insulated 170 μm copper wires are used as extension wires that are connected to the sockets on the PPMS ^{3}He insert. To record the pressure in the sample volume, ruby powder is placed next to the sample. When the arrangement shown in Figure 5.1 is reached, one can close the cell carefully.

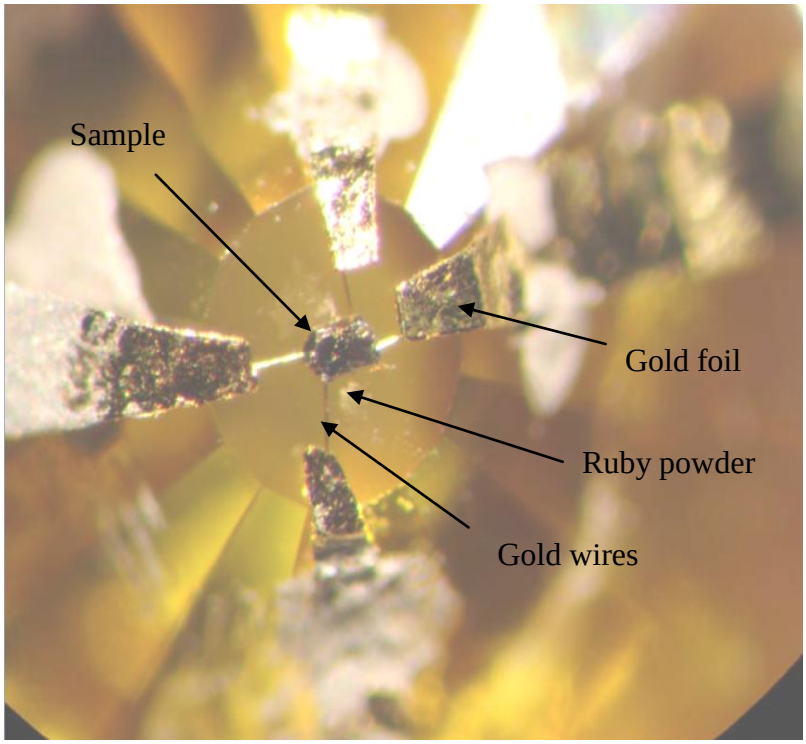

Figure 5.1 The arrangement of sample, gold wires and gold foil electrodes on a diamond anvil.

With the setup above, resistivity of PrNi up to 9 GPa is measured in the DAC.

5.3 Results

5.3.1 Heat capacity of PrNi single crystal at ambient pressure

The heat capacity as a function of temperature is plotted in the range of 1.8 K ~ 125 K in Figure 5.2. Above 20 K, the heat capacity of the sample increases with temperature. A sharp peak at 20 K corresponds to T_C of PrNi at ambient pressure. Below 20 K, the PrNi is in the ferromagnetic state. A large increase in heat capacity of the sample entering the ferromagnetic state indicates that the magnetic contribution to C_p becomes the dominant contribution in PrNi immediately below 20 K.

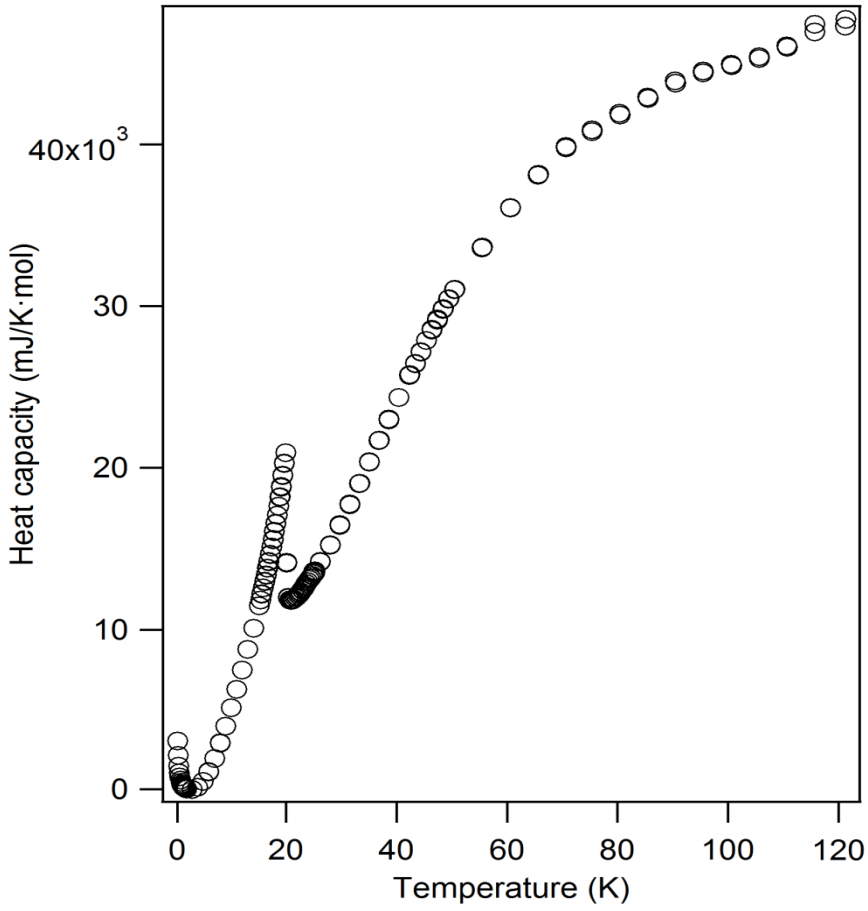

Figure 5.2 The temperature dependence of the heat capacity of PrNi.

A slight increase of C_p on cooling below ~3 K is probably the Schottky anomaly, which is an observed effect in solid state physics where the heat capacity of a solid at low temperature does not decrease with temperature but have a peak.[9]

A Debye model[10] expressed in equation 5.1 is used to calculate the lattice heat capacity of PrNi:

$$C_{phonon} = 9Nk_B(\frac{T}{\theta})^3 \int_0^{x_D} dx \, \frac{x^4 e^x}{(e^x - 1)^2} \tag{5.1}$$

where θ is the Debye temperature, $x_D = \frac{T}{\theta}$ and N is the number of atoms in the specimen. $k_B = 1.38 \times 10^{-23} \mathrm{J/K}$ is the Boltzmann constant.

In this case, the value of N is 2 since the chemical formula of PrNi is 1:1.To work out the lattice heat capacity, the value of the Debye temperature of PrNi is required. The Debye T^3 approximation[10] is expressed in equation 5.2:

$$C_p \cong 234Nk_B(\frac{T}{\theta})^3 \tag{5.2}$$

Therefore, the Debye temperature can be calculated by using the equation 5.2. Since the Debye temperature can be expressed in a form of T^3, the heat capacity data is plotted against T^3 and the slope of the linear part of the curve is fitted at low temperature above T_C. The value of the Debye temperature calculated using the approach mentioned above is 169 K.

The fitted lattice heat capacity is calculated based on the equation 5.1 and the total heat capacity of PrNi are plotted as a function of temperature in Figure 5.3. The lattice heat capacity decreases as the temperature decreases and the vibration of the

phonons becomes weaker.

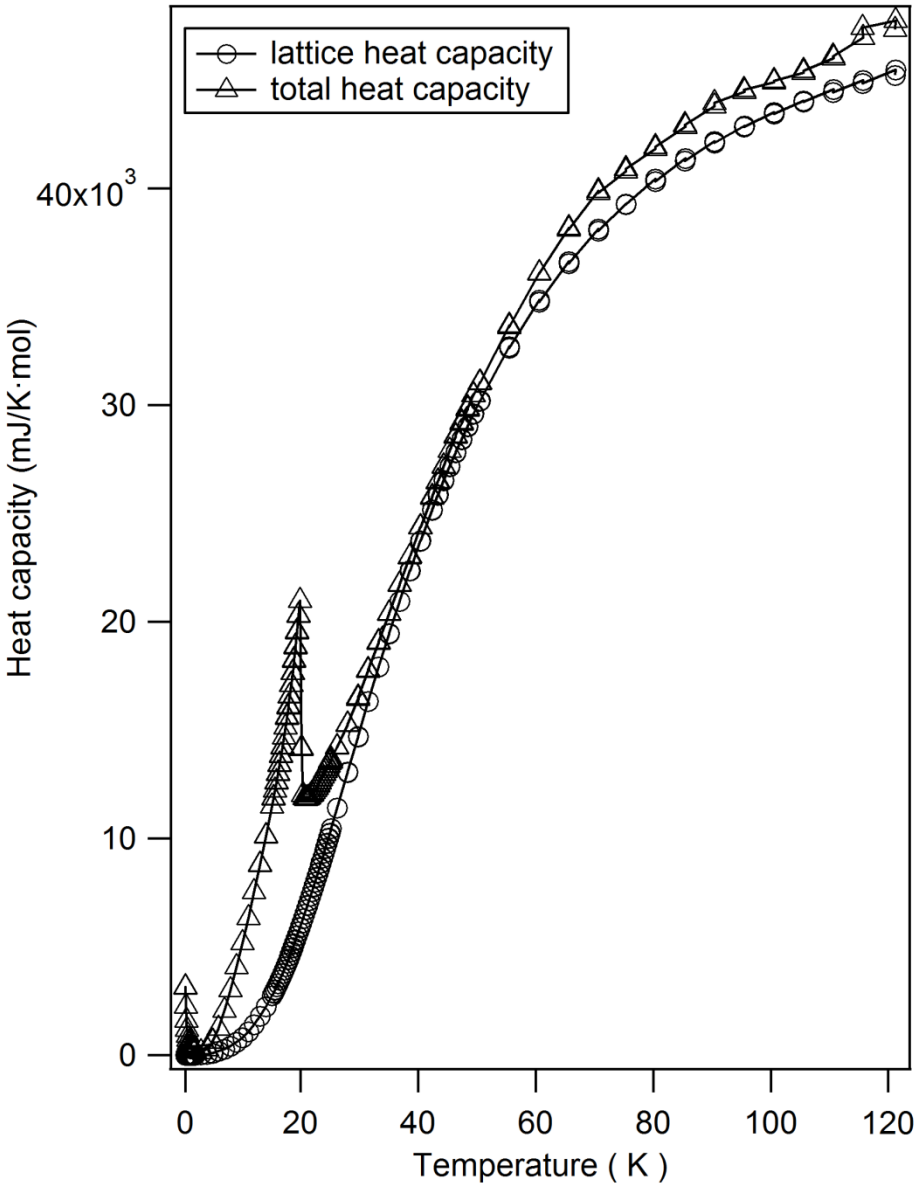

Figure 5.3 The lattice heat capacity of PrNi derived from the Debye model.

By assuming that the total heat capacity consists only of contributions from the lattice and magnetic excitations, the temperature dependence of the magnetic heat capacity can be derived as the difference between the two curves. It is shown in

Figure 5.4. Below 20 K, the magnetic heat capacity drops as the temperature decreases. The magnetic heat capacity is very small when the temperature is above 40 K. Above this temperature, the Debye model is only approximate and subtraction procedure to yield the magnetic heat capacity is no longer valid.

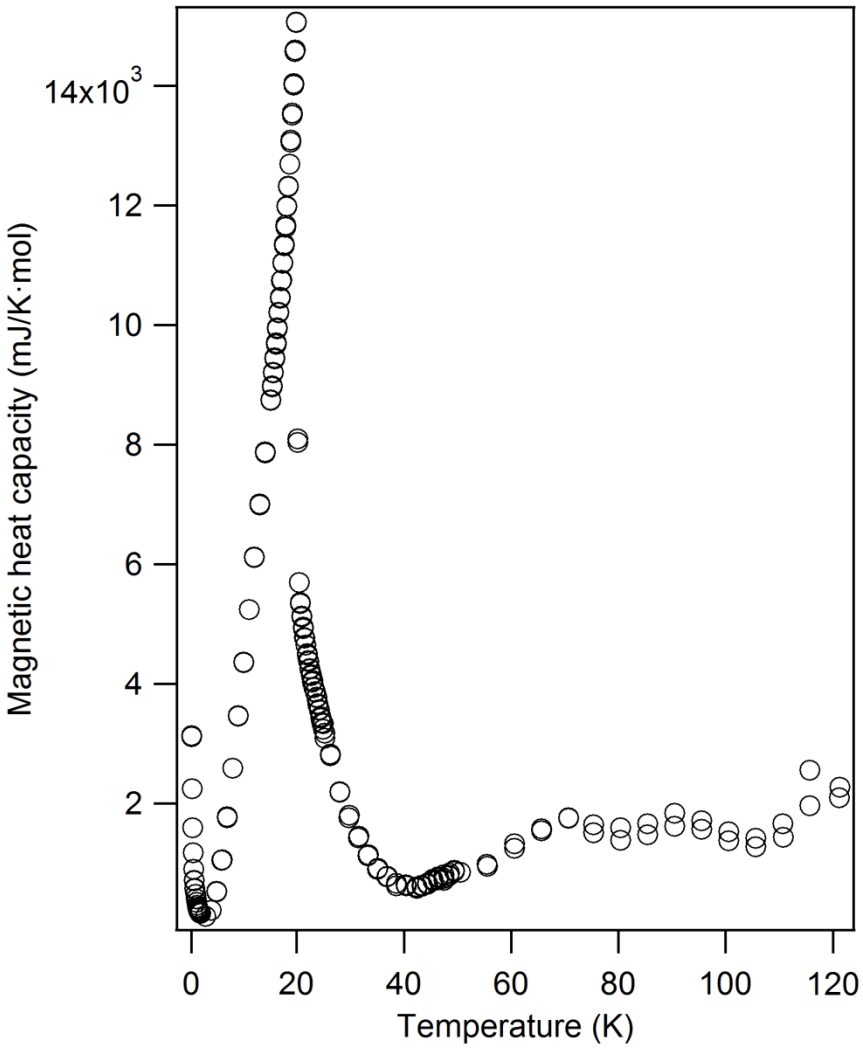

Figure 5.4 The temperature dependence of the magnetic heat capacity in PrNi.

5.3.2 Results of high pressure resistivity study on PrNi single crystal

The temperature dependence of the resistivity of PrNi at high pressure is shown in

Figure 5.5.

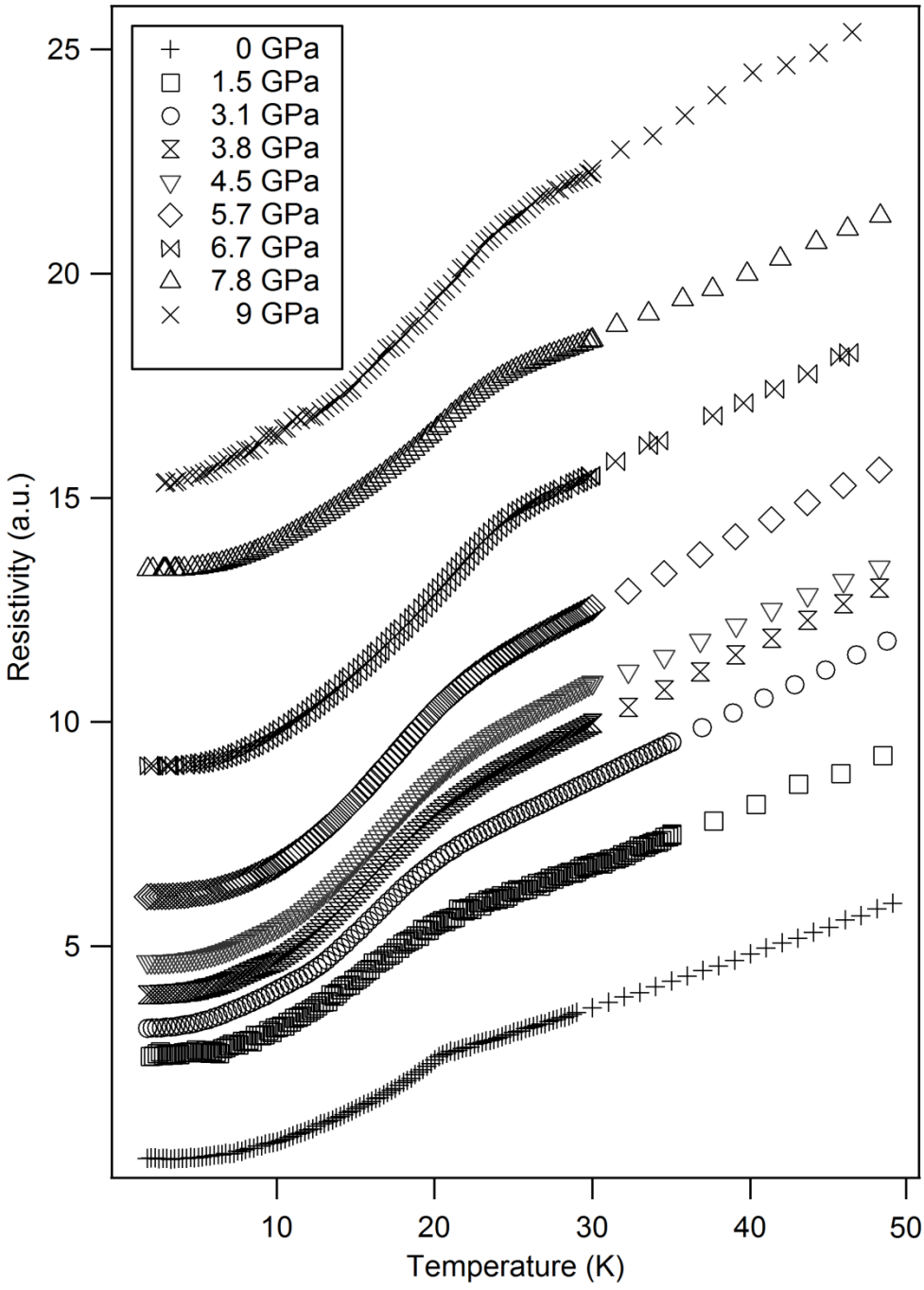

Figure 5.5 The temperature dependence of the resistivity under pressure up to 9 GPa in the temperature range between 1.8 K and 50 K. The data are offset for a better view.

In order to determine the Curie temperature of the transition, a linear fit is made to the high temperature data. The point at which the data diverge from the linear fit (as shown in the inset into Figure 5.6). Figure 5.6 shows the pressure dependence of the Curie temperature. dT_C/dP is about 0.85 K/GPa and this is smaller than the value 1 K/GPa reported by Matas *et al.* The anticipated quantum critical transition has not been observed since the T_C keeps on increasing with the pressure to the highest pressure measured.

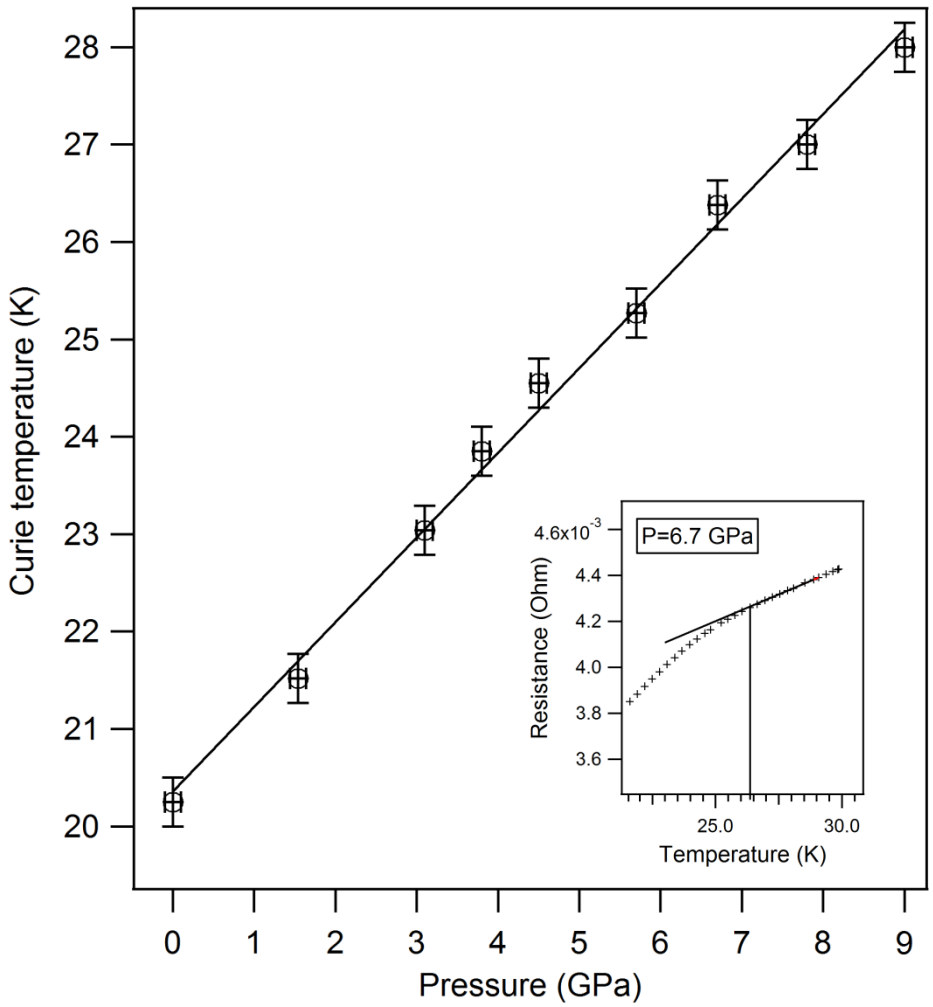

Figure 5.6 The pressure dependence of the Curie temperature. dT_C/dP = 0.85 K/GPa. Inset: The linear fit to high temperature data.

5.4 Discussion

Figure 5.7 shows the temperature derivative of the magnetic heat capacity (C_m/T) versus temperature and a change in the slope is visible at ~10 K, which might indicate the presence of a second excited state in the ferromagnetic phase.

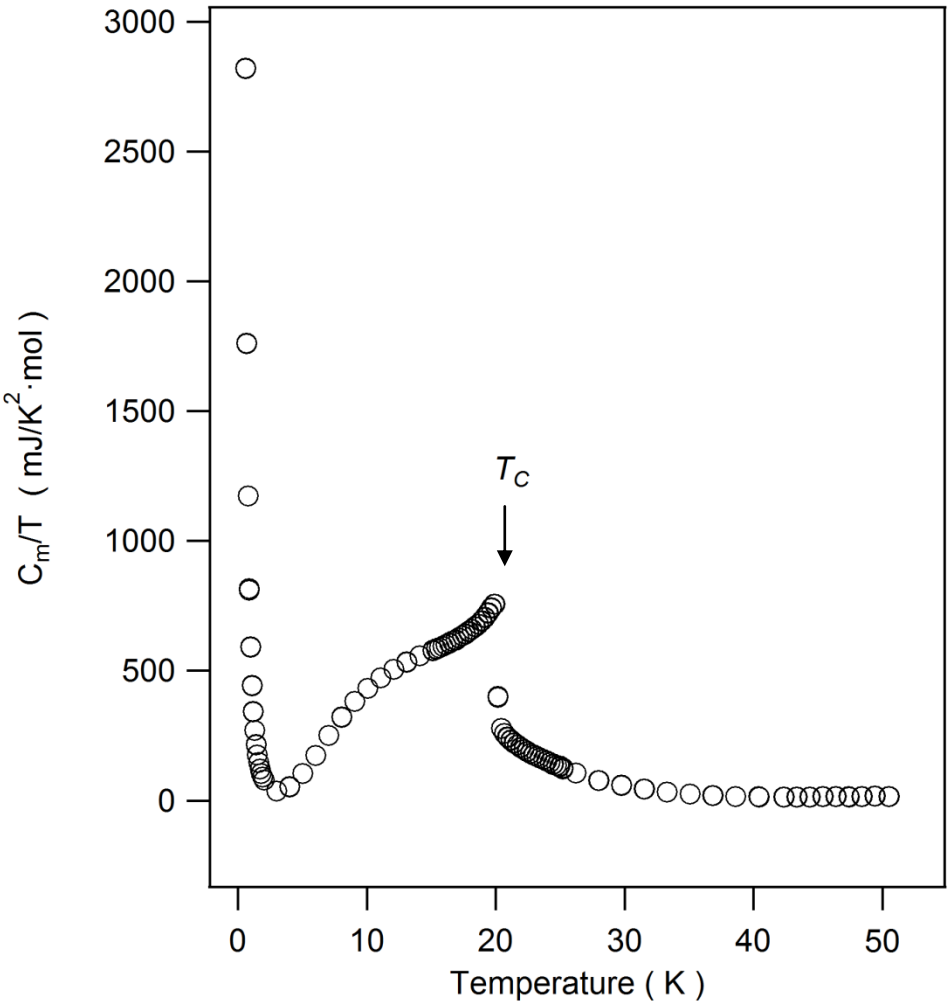

Figure 5.7 The temperature derivative of the magnetic heat capacity vs. temperature.

Since $S = \int \frac{C}{T} dT$, by integrating C_m/T as a function of temperature, the area under

the curve in Figure 5.7, of which is the magnetic entropy in PrNi at low temperatures, can be calculated. The magnetic entropy divided by Avogadro number R vs. temperature is shown in Figure 5.8.

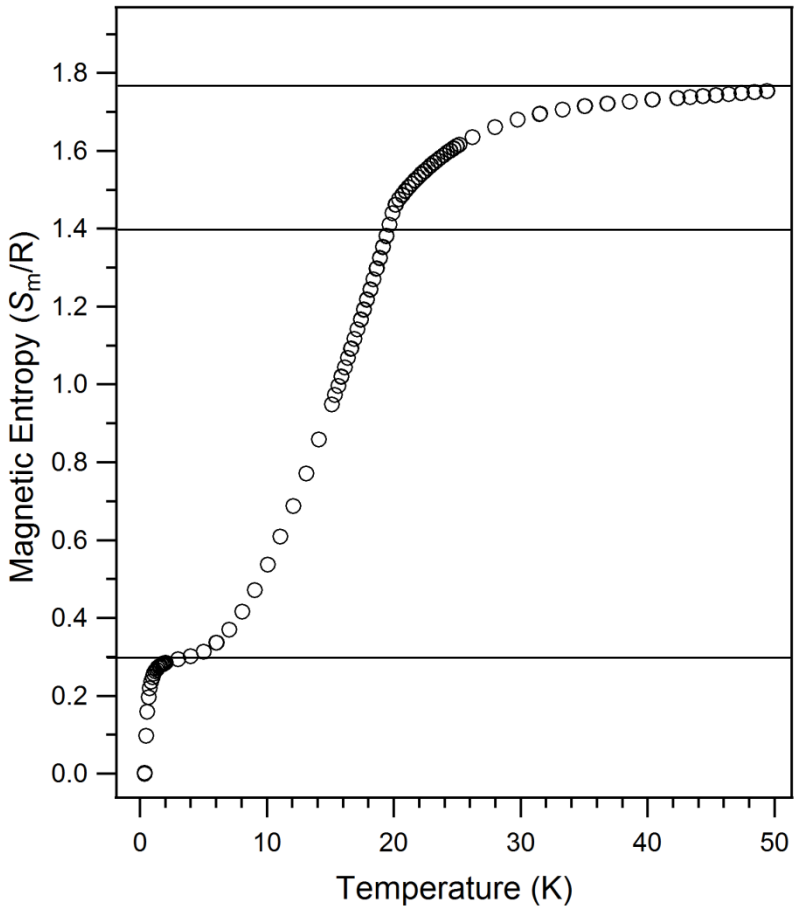

Figure 5.8 The temperature dependence of the magnetic part of entropy S_m/R in PrNi.

Because the 3d band of the nickel is filled up by the 3d electrons, the magnetic contribution from the nickel is negligible.[1] Therefore, only the magnetic contribution from the praseodymium is considered. Isolated Pr^{3+} has J = 4 but in the orthorhombic structure due to the crystal field interaction this is split into 9 singlet states as shown schematically in Figure 5.9. [11,12]

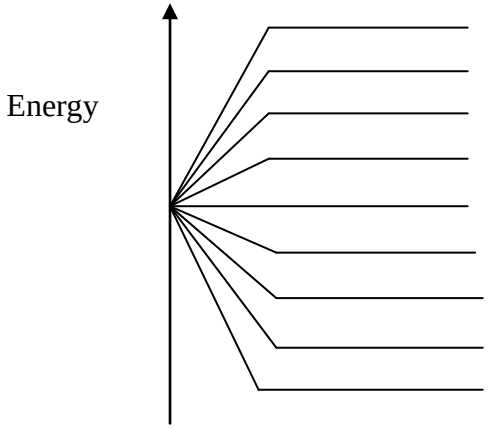

Figure 5.9 Group theory tells us that the 9 fold degenerate total angular momentum state of Pr^{3+} is split into 9 possible singlets.

The entropy[11] can be expressed in equation 5.4:

$$S = Nk_B ln(2J + 1) = Rln(2J + 1) \tag{5.4}$$

in which the value of $(2J+1)$ gives a measure of how many of these singlets there are at a given temperature. When calculating the change in entropy, the base value of S_m/R should be 0.3 since the value below 0.3 is created by the ordering of the nuclei. With the data from Figure 5.8, the calculated value of $(2J+1)$ is either 3.3 or 4.5 based on the two lines marked on the top of the graph, which correspond to the T_C and the saturation, respectively. One might usually expect the lowest two singlets to be mixed. However, for PrNi the data suggest that up to 5 singlets might lie in the energy range up to $2T_C$.

The resistive anomalies changing with the temperature derivative of the magnetic

specific heat at ambient pressure is shown in figure 5.10, which confirms Fisher and Langer's approach.

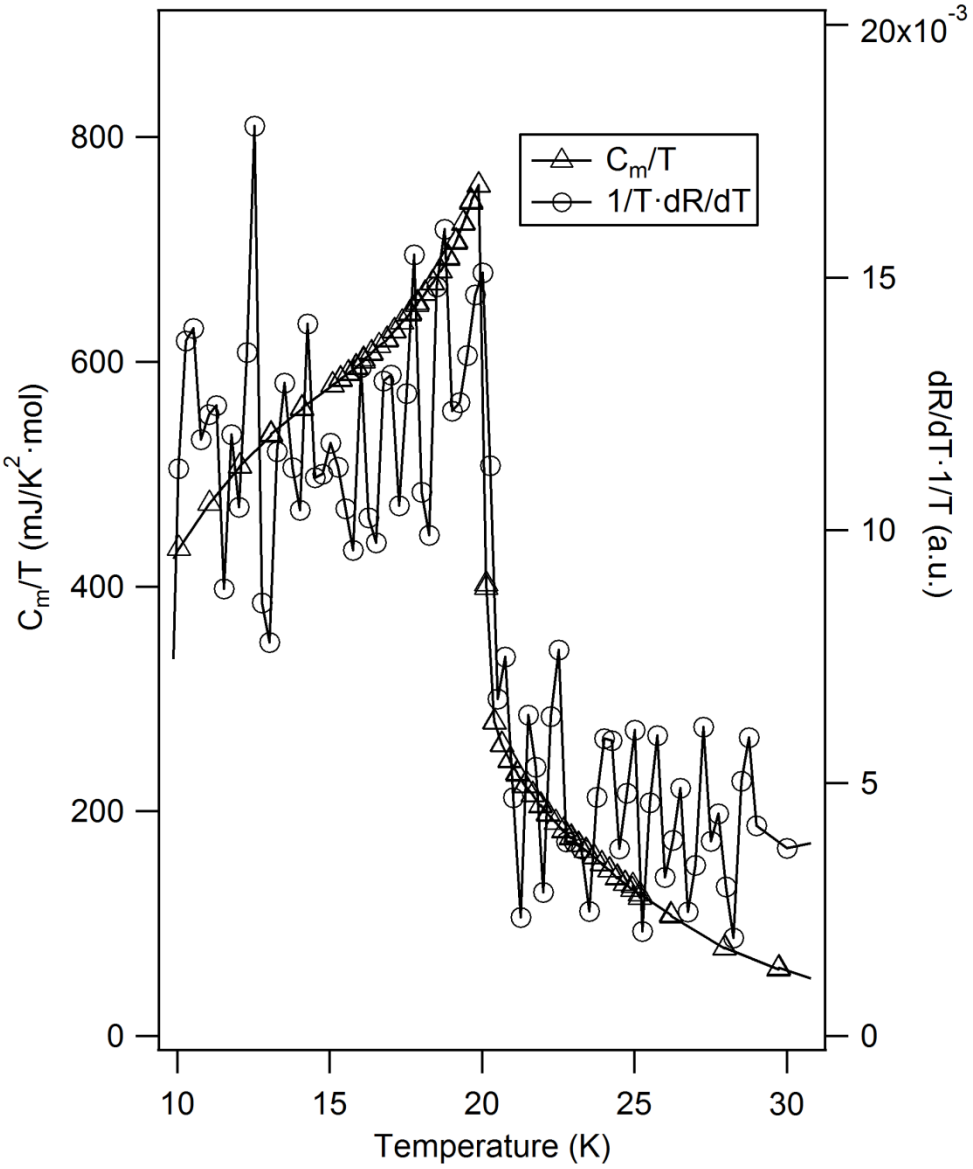

Figure 5.10 Unified temperature dependence of the magnetic heat capacity and temperature derivative of resistivity in the vicinity of the phase-transition region.

Figure 5.10 demonstrates a good match between $(\frac{\partial R}{\partial T})\frac{1}{T}$ and C_m/T in the vicinity of T_C, which makes it possible to use the resistivity data to analyse the heat capacity

behaviour at high pressure. However, the level of the noise in the differentiated resistivity data as can be seen in Figure 5.10 limits the analysis that can be done so $\Delta(\frac{\partial R}{\partial T})$ at T_C, the size of the jump in $(\frac{\partial R}{\partial T})$, is only considered. $\Delta(\frac{\partial R}{\partial T})$ versus T is plotted in Figure 5.11.

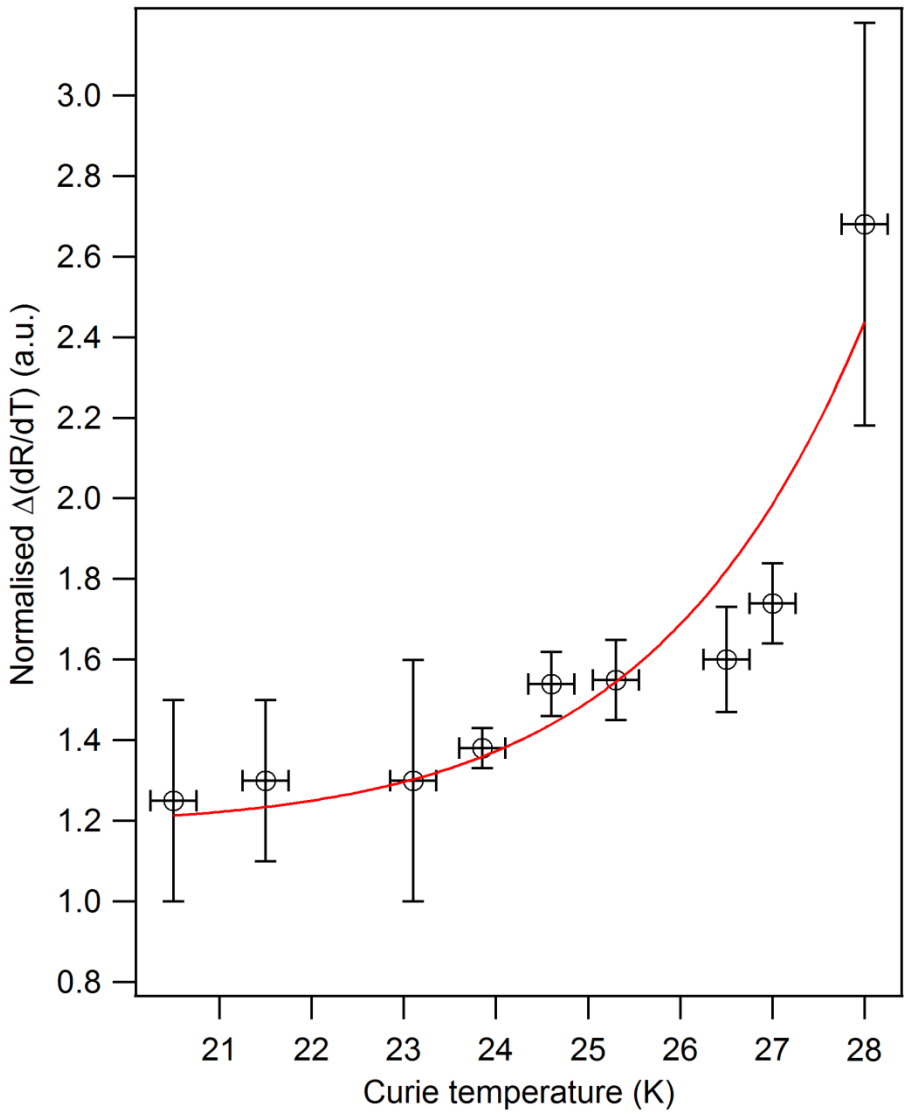

Figure 5.11 $\Delta(\frac{\partial R}{\partial T})$ at T_C in the pressure range between 0 GPa and 9 GPa. $\Delta(\frac{\partial R}{\partial T})$ is normalized by the average of $\frac{\partial R}{\partial T}$ in the vicinity of T_C. The error bar is determined by the level of noise in the temperature derivative of resistivity data. The red line is a

gauss fit to the data.

As can be seen in Figure 5.11, $\Delta(\frac{\partial R}{\partial T})$ increases with pressure. Since the quantity $\Delta(\frac{\partial R}{\partial T})/T$ gives the jump in C_m/T , ΔC_m/T at T_C increases with pressure.

5.5 Conclusions

Heat capacity measurement of an orthorhombic ferromagnet PrNi single crystal was performed in the temperature range of between 0.35 and 121 K by adiabatic calorimetry. A ferromagnetic transition at 20.5 K is confirmed by the heat capacity and resistivity measurement at zero pressure. High pressure up to 9 GPa resistivity study of the same single crystal (2 K < T < 300 K) was conducted in a diamond anvil cell. The critical transition temperature rises with the increasing pressure at a rate of 0.87 K per GPa. The quantity $\Delta(\frac{\partial \rho}{\partial T})$ increases with pressure.

5.6 References

1. G. Fillion *et al*., J. Magn. Magn. Mater. **44**, 173 (1984).

2. S. S. Saxena *et al*., Nature **406**, 587 (2000).

3. A. Demuer *et al*., J. Magn. Magn. Mater. **226-230**, 17-22 (2001).

4. S. MAŤAŠ *et al.*, Acta Phys. Pol. A **133**, 1 (2008).

5. M. E. Fisher *et al*., Phys. Rev. Lett. **20**, 13 (1986).

6. S. M. Stishov *et al*., J. Phys. Condens. Matter. **20**, 235222, (2008).

7. K. V. Kamenev *et al*., High Press. Res. **27**, 1 (2007).

8. Daphne 7373 is a trademark of Idemitsu and a mixture of several olefins.

9. A. Tari, The specific heat of matter at low temperatures, Imperial College Press, (2003).

10. C. Kittel, Introduction to Solid State Physics, 8th edition. Willey & Sons, New York (2005).

11. S. Blundell, Magnetism in Condensed Matter. Oxford University Press, Oxford. (2001).

12. E. S. Clementyev *et al*., Physica B. **350**, e83 (2004).

Chapter 6 Large volume high-pressure cell for inelastic neutron scattering

6.1 Introduction

Neutron scattering is one of the most important experimental techniques for studying magnetic structure and dynamics in condensed matter. Unlike X-rays, neutrons interact with the nuclei of atoms without Coulomb barrier to be overcome due to their neutral charge. Because of the energy of thermal neutrons that is of the same order as that of many excitations in condensed matter, when the neutron is inelastically scattered by the creation or annihilation of an excitation, the change in the energy of the neutron is a large fraction of its initial energy. Therefore, the energy change of the neutron can be calculated. Furthermore, since the neutron has a magnetic moment that can interact with the spins of electrons in magnetic atoms, inelastic magnetic neutron scattering can be used in measuring the energies of magnetic excitations and in studies of time-dependent spin correlations in the scattering system.[1]

In recent years, high pressure has become a popular technique for tuning properties of materials in a clean and controllable fashion. Under a limited pressure range between 1.0 and 1.6 GPa, the coexistence of superconductivity and ferromagnetism at a temperature below 1 K in UGe_2 was discovered by Saxena *et al*.[2] Measurement of electrical resistivity of UGe_2 under high pressure indicates an additional transition within the ferromagnetic state. The characteristic temperature of this transition, T_x, decreases with pressure and disappears at a pressure P_x close to the pressure at which the superconductivity is strongest.[3] Inelastic Neutron Scattering (INS) study on UGe_2

at ambient pressure has revealed that the uniform magnetization is not conserved in the magnetic excitation spectrum of UGe_2 and further INS measurements on UGe_2 have experimentally confirmed the prediction of dynamical critical phenomena for the kinetic Ising model with a non-conserved magnetization.[4,5] However, the nature of the transition at P_x is not clear. The pairing interaction could be predominantly spin based or phononic or due to the combined action of both mechanisms. Therefore, the INS study of UGe_2 at high pressure is required to clarify this.

In the following section, the major impediments to carrying out high pressure INS studies are discussed in detail.

6.2 Design challenges

Because of the nature of the INS technique, the energy of the incident neutron beam is very weak, which means it needs longer data collection times. Therefore, a large sample is usually preferred in order to reduce the data collection times but accommodating large samples in a high pressure cell is rather difficult since this would result in the increased thickness of the body of the pressure vessel. Thicker walls can absorb a large fraction of the energy of the neutron beam and the transmitted neutron beam is then too low to be measured. Thus, the major challenge of designing a high pressure cell for the INS studies is the limited size of the sample and the attenuation of the neutron beam passing through the wall of the cell.[6,7]

There are two types of high pressure devices: opposed anvil and piston-cylinder cells, which are used to generate pressure on the sample. Opposed anvil pressure cells such as those based on the Paris-Edinburgh press[8] that can achieve pressures of up to 10 GPa have been used in INS experiments.[9] However, the sample volume is limited to 10-25 mm^3 and a large background is produced by the anvils and gasket, which

makes low energy excitation in materials hard to be observed.

To accommodate large samples, high-pressure cells made of an aluminium alloy and based on piston-cylinder design are often used. Good transparency to neutrons is their advantage but the maximum pressure those cells can reach is limited by the low yield strength of the aluminium alloy. The INS pressure cell made of aluminium 7075-T6 alloy with a maximum sample volume of 3 cm^3 has been reported to achieve 0.4 GPa at 4 K in early 1975[10] and recently another INS pressure cell[11] made of high-strength aluminium alloy for studying the quantum fluids and magnetic phenomena has a substantial sample volume of 18 cm^3 but it can reach only 0.001 GPa around 100 mK. Although the pressure on the sample can be controlled with a high degree of accuracy in both pressure cells, the maximum pressure they can reach is under 0.5 GPa. High yield strength materials such as maraging steel, nickel-chromium-aluminium (Ni-Cr-Al or 40HNU-VI) alloy, copper-beryllium (Cu-Be) alloy and cobalt-nickel-chromium-molybdenum (Cr-Ni-Cr-Mo or MP35N) alloy have been used in construction of high pressure devices that are capable of reaching up to 4 GPa[12,13] but the thick wall of the cells and the large attenuation from those materials make them unsuitable for INS measurements.

To probe the nature of weak magnetic excitations, pressure cells should be built using materials such as Cu-Be alloy and Ni-Cr-Al alloy and thus to minimize the magnetic interference from the body of the devices. The *Clamp 04PCL150CB5* cell made of Cu-Be alloy available at the Institut Laue-Langevin (ILL, France) can accommodate a sample of 5 mm in diameter and 20 mm long has been claimed to reach 1.5 GPa at room temperatures.[14] Low temperature INS studies performed in this cell have been reported at a pressure of up to 1.2 GPa.[15,16] This pressure cell is close to our design criteria but the range of the pressure it can achieve does not cover the full pressure range between 1 GPa and 1.6 GPa where P_x could exist in UGe_2.

Taking into account the loss of pressure in the liquid pressure medium while cooling down to the base temperature of the cryogenic device, a device that is capable of reaching at least 1.8 GPa at room temperature is required.

Because of the narrow range of existence of P_x in UGe_2, the accuracy of the pressure measurement becomes crucial for our INS studies. In the pressure cells for neutron scattering, pressure is determined either by using reference materials with known equation of state such as sodium chloride (NaCl)[17] or using the known pressure dependence of the superconducting transition in lead (Pb), tin (Sn) or indium (In)[18]. The introduction of the reference materials usually takes up some of the sample space and contaminates the scattering pattern by introducing extra peaks in the spectrum, which would substantially affect the measurements of weakly scattering samples. In the case of using calibrated transition temperature of materials, the pressure can only be known at the transition temperature and is hard to estimate when the temperature of the sample is over or below that temperature.

So far there has not been a large volume high-pressure cell working to 1.8 GPa built for the INS studies that can also provide precise reading of pressure at any given temperature without disturbing the scattered pattern. In the following section, the design of a large volume two-layered piston-cylinder pressure cell with the safe working limit of 1.8 GPa and with transmission optimized for INS studies is presented.

6.3 Design of the pressure cell and material selection

6.3.1 Overview

The cross-sectional view of the pressure cell with its key dimensions is shown in

Figure 6.1. The cell is based on the design approach used in hybrid clamp cells.[12,13] Its main parts are a cylindrical body, a plug with electrical feed-through, a piston, a spacer and a locking nut. Because the cell is used to probe magnetic excitations of solids, all the parts of the cell are made of materials with low magnetic susceptibility.

Tungsten carbide (WC) due to its high compressive strength is often chosen to make the parts that are subjected to compressive stress. In our cell, the pusher, piston and spacer of the cell are made of non-magnetic binderless WC, Roctec 500 a product from *Kennametal Inc*.[19] High yield strength materials that retain good ductility at low temperature are used to fabricate the parts under tension thus the locking nut, the plug and the outer sleeve are made of fully hardened BERYLCO-25 alloy (yield strength = 1.4 GPa)[20] and the inner cylinder is composed of Cr-Ni-Al alloy[21] imported from Japan (yield strength = 2.1 GPa)[22]. MP35N alloy is not used here because its magnetic susceptibility is much higher than that of Cr-Ni-Al and Cu-Be alloys.[13] The body of the pressure cell is 44 mm in diameter and 130mm long making it suitable for use with most common cryostats, closed cycle refrigerators (CCR) and cryomagnets. The sample space is optimized and can accommodate a sample of 6 mm in diameter and 15 mm long which translates into approximately 425 mm^3 of volume. Like other clamped cells, the load is generated in a hydraulic press, from which it is transferred to a removable pusher and the pressure is locked by means of the locking nut.

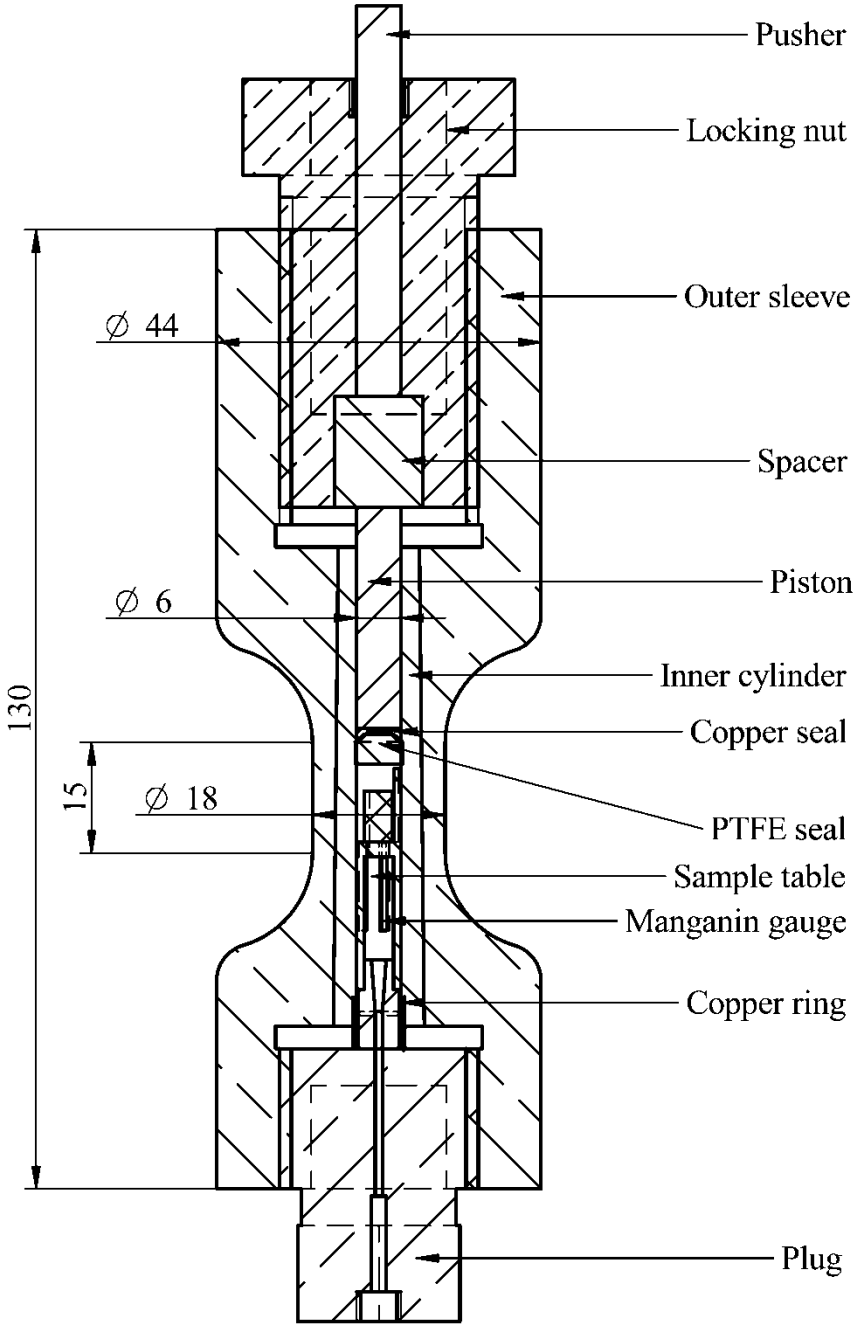

Figure 6.1 Cross-sectional view of the pressure cell assembly (dimensions are in mm).

6.3.2 Two layered body and neck optimization

Two layered pressure cell can generate higher pressure compared to what can be achieved by a single-cylinder device,[23] which makes it possible to reduce the overall thickness of the cell at the sample position by creating a neck on the outer cylinder to minimize the neutron attenuation without compromising the pressure limit of the cell. The body of the cell consists of two parts, the inner cylinder and the outer sleeve. The bore of the outer Cu-Be sleeve and the outer surface of the Ni-Cr-Al inner cylinder are machined with 1:50 taper and the inner cylinder press-fitted into the Cu-Be outer sleeve with a 0.05 mm interference fit. The interference fit for a double cylinder pressure cell made from materials that have close values of elastic modulus and Poisson's ratio can be expressed in an empirical equation:

$$\Delta = \frac{p\sqrt{ab}}{E} \tag{6.1}$$

where *a* is the radius of the bore and *b* is the outer radius of the outer cylinder. *E* is the elastic modulus of the material and *p* is the tangential (loop) stress at the bore's surface.[23]

The interface pressure for two-layer cylinder made from the same material is defined as:

$$p_c = \frac{E\Delta(c^2 - a^2)(b^2 - c^2)}{2c^3(b^2 - a^{2)}} \tag{6.2}$$

Figure 6.2 shows the stress distribution for unloaded and loaded two-layer cylinder.

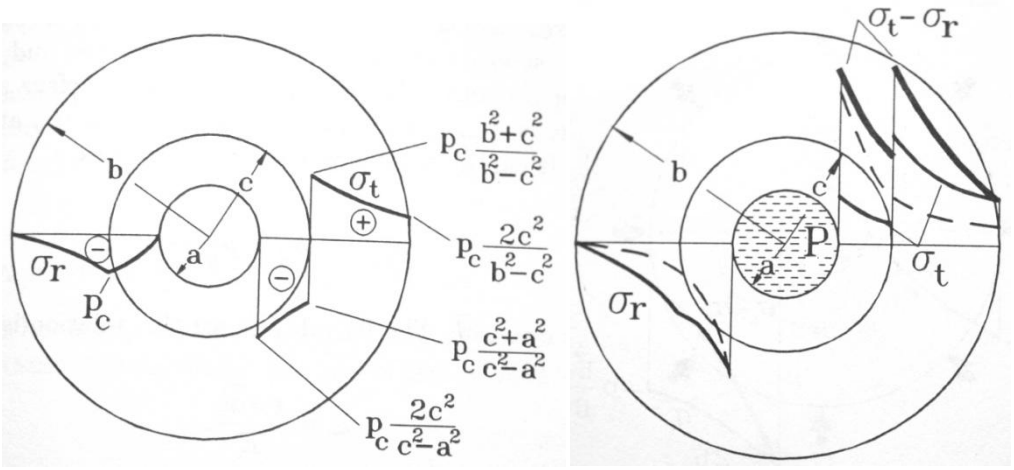

(a) (b)

Figure 6.2 (a) Stress distribution in an unloaded two-layer cylinder (b) Stress distribution in a two-layer cylinder loaded with internal pressure.[23]

The diameter of the bore (a = 3 mm) is the limit set by the size of the single crystal and the outer diameter of the inner cylinder (b = 5.5 mm) is the maximum acceptable attenuation and is also set by the size of the raw Ni-Cr-Al alloy. One can only use equation 6.1 when $c = \sqrt{ab}$. In this case, the materials used to build the body of the cell have slightly large difference of elastic modulus which means it might be unsuitable to use equation 6.1. However, when calculating the interference fit for the proposed design, for the safe operation of the cell, the lower elastic modulus is used. The value of the interference fit calculated based on equation 6.1 is applied in the following neck optimization. The calculated value of the outer diameter of the inner cylinder is 10.08 mm. from Equation 6.1 is a rough estimate since the provision to use this equation is that the two cylinders are the same materials. Therefore, the neck optimization through the FEA is needed to give accurate results.

In order to minimize the amount of the cell material in the neutron beam, ANSYS® finite element analysis (FEA) software[24] was used to optimize the diameter of the

neck of the outer sleeve for a fixed 11 mm outer diameter (OD) and 6mm inner diameter (ID) of the inner cylinder. Firstly, because of the flats cut on the cell for gripping it in the vice during the assembly of the pressure cell, the cell is not axisymmetrical. Therefore, 3D models of the two layered body created using Solid Edge computer aided design (CAD) software[25] were imported into ANSYS®. In the model, physical properties of BERYLCO-25 and Ni-Cr-Al alloy were assigned to outer and inner cylinders separately and flexible stiffness behaviour was chosen for both parts because they can be deformed subjected to the externally applied force. The connection between the two cylinders is defined as rough, which means the sliding is not permitted during contact. The mesh using fine element size of 1 mm was generated for the whole assembly in a slow transition and high smoothing mode. To obtain accurate results, additional mesh refinement at the neck of the cell has been provided in the model. A pressure of 2 GPa is applied to the bore surface of the neck and a fixed support is set at the bottom side of the outer sleeve shown in Figure 6.3.

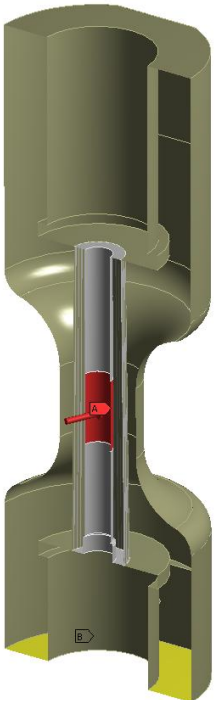

Figure 6.3 Definition of the static structural model

Maximum tensile stress along any direction was calculated for the two layered body with the diameter of the neck varying from 14 mm to 34 mm. The results of the FEA of the maximum stress as a function of the neck diameter for the fixed 6 mm bore of the cell are summarized in Figure 6.4.

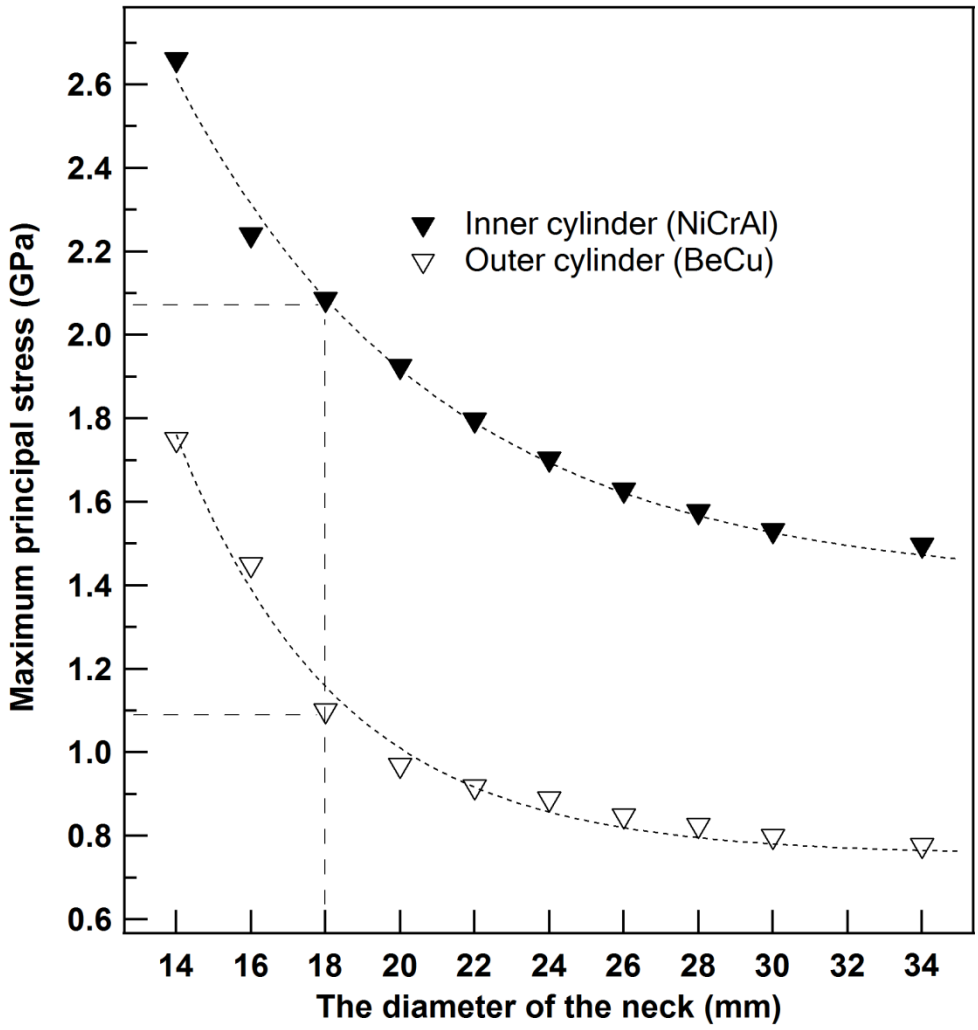

Figure 6.4 Calculated maximum stress in the inner Cr-Ni-Al cylinder (filled triangles) and in the outer BERYLCO-25 sleeve (open triangles) for pressure of 2.0 GPa applied to the sample volume.

It shows that for the neck diameter of 18 mm the maximum stress in the Cr-Ni-Al

cylinder is 2.09 GPa and that in BERYLCO-25 sleeve is 1.1 GPa. The stress of 2.1 GPa is matching the yield strength of Cr-Ni-Al alloy, while the stress of 1.1 GPa is some 20% lower than the yield strength of BERYLCO-25 alloy of which the outer sleeve is made (See Appendix for the material property data sheet). Therefore, a safety factor of 1.2 is applied to this pressure cell. Because the inner cylinder is made of relative fragile material, when it fails, a small crack will appear on the surface of the inner cylinder and the pressure will drop dramatically, which can be noticed during the loading of pressure cell. One of the functions of the outer sleeve is to ensure the safety of operators in case of the failure of the inner cylinder and, therefore, having the stress lower than the yield strength of the material contributes to the safety of the design of the pressure cell.

In this case, the radius of the outer cylinder, 9 mm, is smaller than the previously calculated 10.08 mm based on the empirical equation for materials with the same modulus and Poisson's ratio. The use of stronger inner material reduces the radius of the outer cylinder which benefits the INS measurement allowing for lower attenuation of the neutron beam. Figure 6.5 presents a section view of the body of the cell and shows the stress distribution for the ø18 mm neck at 2.0 GPa.

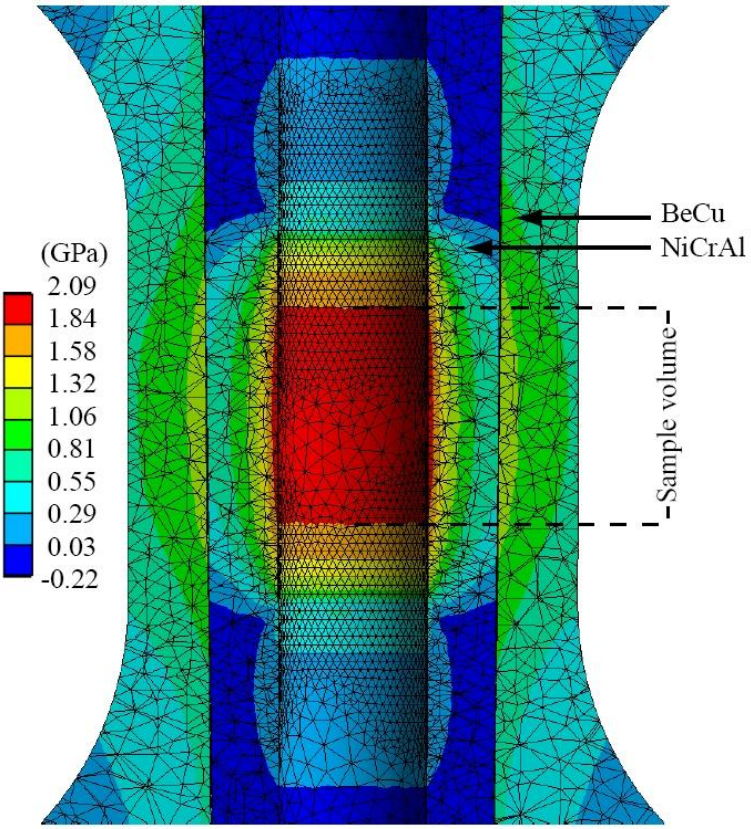

Figure 6.5 Section view of the 3D FEA model of the pressure cell body with the maximum principal stress distribution as calculated for the sample pressure of 2 GPa.

In order to estimate the suitability of the proposed design of the pressure cell for INS studies, neutron transmission is estimated as follows. The neutron transmission is defined by the equation below.

$$T = \frac{I_t}{I_i} = e^{-\mu t} \tag{6.3}$$

where I_t and I_i are the intensities of transmitted and incident neutron beams, respectively; t is the thickness of the material and μ is the total cross section per unit volume.[1]

From equation 6.2, in order to estimate the transmission of the pressure cell, the total cross section per unit volume is needed apart from knowing the thickness of the material. μ is equal to Σ_T that consists three parts shown in equation 6.4:

$$\Sigma_T = \Sigma_c + \Sigma_i + \Sigma_a \tag{6.4}$$

where Σ_c and Σ_i are the coherent and incoherent scattering cross sections, respectively, per unit volume (in units of cm^{-1}) and Σ_a is the absorption cross section per unit volume.[26]

The values for the scattering and absorption cross sections for warm neutrons at a speed of 2200 m/s are provided by the National Institute of Standards and Technology (NIST).[27] The total cross section per unit volume which is equal to the reciprocal of "the 1/e neutron length" (1/e length = $1/\Sigma_T$) depends on the density of the materials and wave-vectors of the neutron beam. "The 1/e neutron length" is the thickness of the material that will attenuate a neutron beam to 1/e (about 0.37) of its incident intensity. Due to the difficulty in calculating the total cross section per unit volume manually, a calculator provided at NIST website enables users to acquire the 1/e neutron length if the composition and density of compound and the wavelength of neutron beam are provided. Table 6.1 shows the data supplied to the NIST calculator[28] and the 1/e neutron length obtained.

Materials	Composition	Density	Wave-vector	The 1/e neutron length
BERYLCO-25 alloy	$Cu_{975}Be_{25}$	8.25 g/cm^3	1.141 $Å^{-1}$	0.6486 cm
			2.282 $Å^{-1}$	0.9164 cm
Ni-Cr-Al alloy	$Ni_{565}Cr_{400}Al_{35}$	7.85g/cm^3	1.141 $Å^{-1}$	0.4960 cm
			2.282 $Å^{-1}$	0.6578 cm

Table 6.1 The 1/e length of Cu-Be alloy and Ni-Cr-Al alloy for k =1.141 $Å^{-1}$and 2.28 $Å^{-1}$, respectively.

Therefore, the transmission of the pressure cell is calculated for k = 1.141 $Å^{-1}$ (cold neutrons) and k = 2.282 $Å^{-1}$ (warm neutrons) as 12.4% and 21.8%, respectively.

6.3.3 Piston seal design

Tungsten carbide is one of the best materials for making the piston of the pressure cell due to its high compressive strength. However, the material normally comes with Co- or Ni-binder which makes the piston magnetic. The non-magnetic binderless WC Roctec 500 in this design can be subjected to a compressive stress of over 2 GPa[19] but the difficulties with machining ceramics make it impossible to implement the conventional mushroom type seal. The conventional mushroom seal is based on the Bridgeman unsupported area principle which requires machining the insert into the piston to a mushroom shape and having it engaged into the hole in the piston with several soft and hard washers. The soft washers used in the mushroom seal are usually made of soft metals such as indium, lead or tin, all of which unfortunately become superconductive at low temperature. This can affect the INS measurement by disturbing the magnetic field at the sample position. Those soft metals also coat the bore of the cell and this can contribute to the neutron scattering pattern, which can make makes INS measurements on weakly scattering sample rather difficult. The solution for the above problem in earlier designs was to use a PTFE capsule enclosing the sample and a pressure transmitting medium.[12, 29] However, the use of the capsule takes up valuable sample space and neutron scattering from the PTFE can be significant when the low wave-vectors beam is used.[30] The problems discussed above were solved by removing the capsule and implementing the seal shown in Figure 6.6.

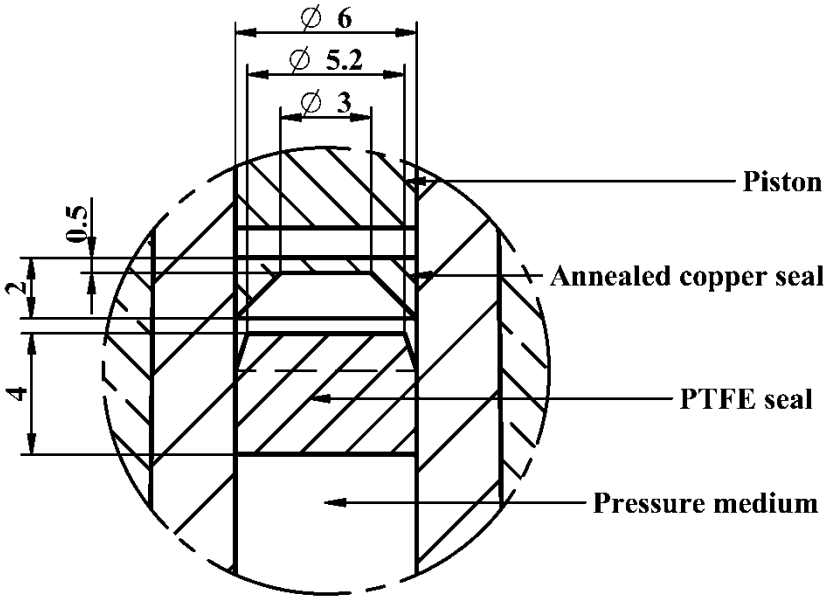

Figure 6.6 Piston and seals assembly (dimensions are in mm). The piston, copper and PTFE seals are shown in the initial position and are separated by small gaps for clarity.

The seal assembly of the piston consists of an oversized PTFE puck with a taper at one end for ease of inserting it into the bore and an annealed copper anti-extrusion ring with a trapezoid cut-out profile. The operation of the seal is based on the unsupported area principle with the initial gap between the top tip of the PTFE puck and the inner edge of the copper seal. This gap enables the PTFE puck to provide initial sealing at low pressures and generate enough force on the outer edge of the copper ring, which starts to seal at pressures above ~0.5 GPa. This novel piston seal design makes the full use of the 6 mm bore of the pressure cell for accommodating large single crystals.

Please note that this piston seal design requires high level of uniformity of the bore of the inner cylinder. Base on the experiments, the tolerance of the bore diameter should be within ±5 μm.

6.3.4 The plug with manganin gauges

The load applied to the piston is not fully converted into the pressure inside the cell because of the friction between the piston and the seals and the bore of the cell. In order to avoid any ambiguity with the pressure measurement at low temperature and the interference from the pressure reference samples, a single-piece electrical plug is used in this design (shown in Figure 6.7). The plug has 12 enamelled ø150 μm copper feed-through wires, of which 4 are used for measuring electrical resistivity of a pressure sensor. The copper wires are sealed into a 1 mm hole made in the plug with Stycast 2850 FT epoxy[31]. In order to prevent debonding of the epoxy due to different thermal coefficient from the plug material, fine diamond powder was mixed with the epoxy to decrease thermal coefficient of epoxy similarly to the approach used by Walker.[29] Another advantage of this approach is that the compressive strength of the epoxy is enhanced by the diamond powder. Before the epoxy was introduced into the bore of the plug, the plug was ultrasonically cleaned in acetone to degrease it and to remove any metallic dust left in the hole of the plug from the machining process. A vacuum pump was used to ensure that the epoxy goes down the hole and in between the wires as it was added into the bore of the plug. Once the epoxy emerges from the bottom of the plug, pumping can stop. The plug is then left for the epoxy to solidify.

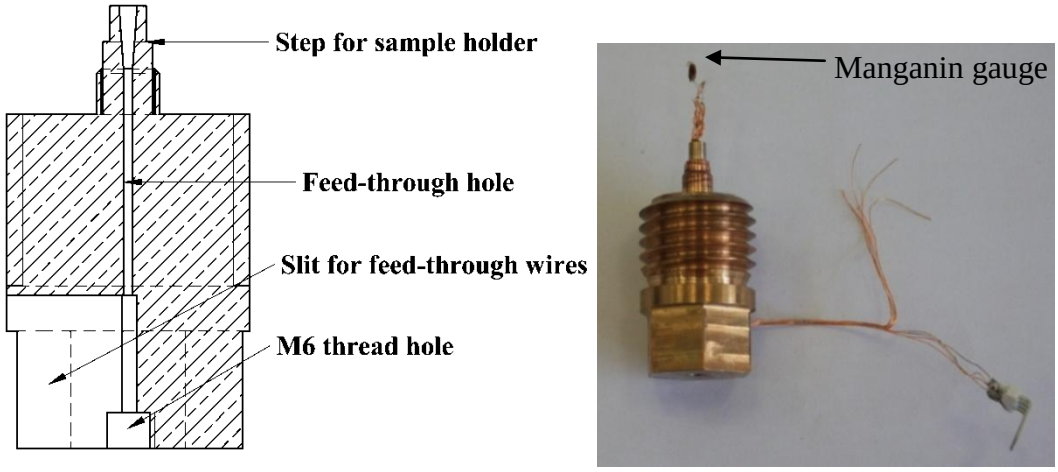

Figure 6.7 (a) Section view of the plug, (b) Single piece plug with a manganin gauge mounted.

The manganin, an alloy of 86% copper, 12% manganese, and 2% nickel, has a very low temperature coefficient of resistivity. Its electrical resistivity has also been well calibrated as a function of pressure at temperature wide range of temperatures.[33] In this design, the pressure gauge is made of a ø50 μm enamelled manganin wire supplied by the Scientific Wire Company. A manganin wire with the overall resistance of approximately 100 Ω is shaped into a coil by being wrapped around a 1 mm drill blank. The coil was coated with the GE-Varnish diluted with ethanol. Once the varnish is dry, the coil can be removed from the core used for winding. Prior to being used as a pressure gauge, further treatment is required for the manganin pressure gauge. Firstly, it is annealed at a temperature of 150 ℃ in a furnace for 24 hours. The coil is then repeatedly cycled between the temperatures of 300 K and 2 K to minimize the thermal hysteresis. Finally, high hydrostatic pressure is applied to the coil several times to stabilize the internal mechanical stress and reduce the hysteresis.

The resistance of the manganin pressure gauge is measured using a four-probe technique by means of a current source and a nano-voltmeter (Keithley Instruments Inc). Using this setup, it is possible to measure pressure with the accuracy better than

0.01 GPa when a manganin pressure gauge with a resistance of an order of 100 Ω is used.

The electrical plug is sealed in the body of the cell by using an annealed copper ring on the neck of the plug. The design of this plug eliminates the need for a tungsten carbide pressure retention pad that is commonly used in other piston cylinder cells[12,30], which avoids the machining of the tungsten carbide. A female M6 thread hole is made at the back of the plug for mounting the pressure cell in the cryogenic equipment.

6.4 Assembling and testing the pressure cell

6.4.1 The operation of the pressure cell

Prior to assembling the pressure cell, all the parts are cleaned in an ultrasonic bath using ethanol. The assembly of the high-pressure cell starts with engaging the piston into the bore of the cell and backing it up by the spacer and the locking nut. To avoid the friction originating from the contact between the spacer and the back of the piston, a small amount of vacuum grease is applied to the interface. The annealed copper seal with a trapezoid cut-out profile is inserted into the bore from the plug end of the cell with the flat end facing the piston from the other end of the cell as shown in Figure 6.1. The PTFE seal is slightly oversized (ø6.4 mm) compared to the bore of the cell (ø6.0 mm). Therefore, in order to insert it into the bore, a pusher (ø5.9 mm) and a hydraulic press are used. The cell is filled with pressure medium by using a syringe and the pressure medium is stirred by a wooden stick to ensure there are no air bubbles trapped in the fluid.

The next step is concerned with the preparation of the electrical plug and the single crystal to be measured. The copper ring is mounted on the neck of the electrical plug. The single crystal in the preferred orientation is mounted on the aluminium sample holder by means of ultrathin aluminium foil. The sample holder carrying the single crystal is mounted on the top of the electrical plug. To avoid the movement of the sample inside the pressure cell and with respect to the neutron beam, the sample holders is tightly mounted on the plug. While mounting the sample holder on the plug, one should be careful with the manganin pressure gauge that is the most delicate part of the whole assembly.

The last step of the assembly process is to screw the electrical plug into the body of the pressure cell. In order to engage the seal, the copper ring mounted on the plug needs to be crushed. This is done by tightening the plug while holding the body of the cell in a vice.

Once the cell is assembled, it is placed into a stainless steel safety shield and positioned between the piston and the anvil of a 20 tonne hydraulic press. The load is transferred to the piston through the pusher and the spacer and monitored by measuring the resistance of the manganin gauge. To minimize the effect of a sudden shock to the cell and the piston in case of the seal failure, the pressure is locked approximately every 0.1-0.2 GPa by means of the locking nut. When the required pressure is reached, the load is released and the loaded cell can be removed from the press.

6.4.2 Mechanical and thermal tests

To confirm the maximum operational pressure the cell can achieve safely, several mechanical loading tests were carried out. For these tests, the assembled pressure cell is placed in a hydraulic press (LCP20, Uni Press) and a short stainless steel rod used to mimic the sample and to displace oil is mounted on the sample table. This is

required in order to reduce the amount of energy released in case of the failure of the high-pressure cell as the amount of energy stored in a solid at a given pressure is much less than the energy stored in a liquid of the same volume. The pressure cell has survived several tests at a pressure of up to 1.8 GPa. The loading curve for the cell at room temperature is presented in Figure 6.8. The pressure and the load are measured using manganin gauge and the load gauge on the press, respectively. The error of the pressure is within 0.01 GPa and that of the load is ±0.15 kN. Solid line is the ideal loading curve calculated from the applied force over the area of the piston. Up to the pressure of 1 GPa, the piston seal behaves in almost frictionless fashion. At higher loads, small frictional effects become noticeable. At the maximum pressure of 1.8 GPa, the difference of 0.2 GPa is observed between the ideal loading curve and the measured pressure, which is comparable to the best pressure-load performance achieved with a PTFE capsule.[12] According to our experience, the friction effects can be reduced if we use shorter PTFE pucks for the piston seal assembly. However, shorter pucks do not seal as reliably as the standard ones.

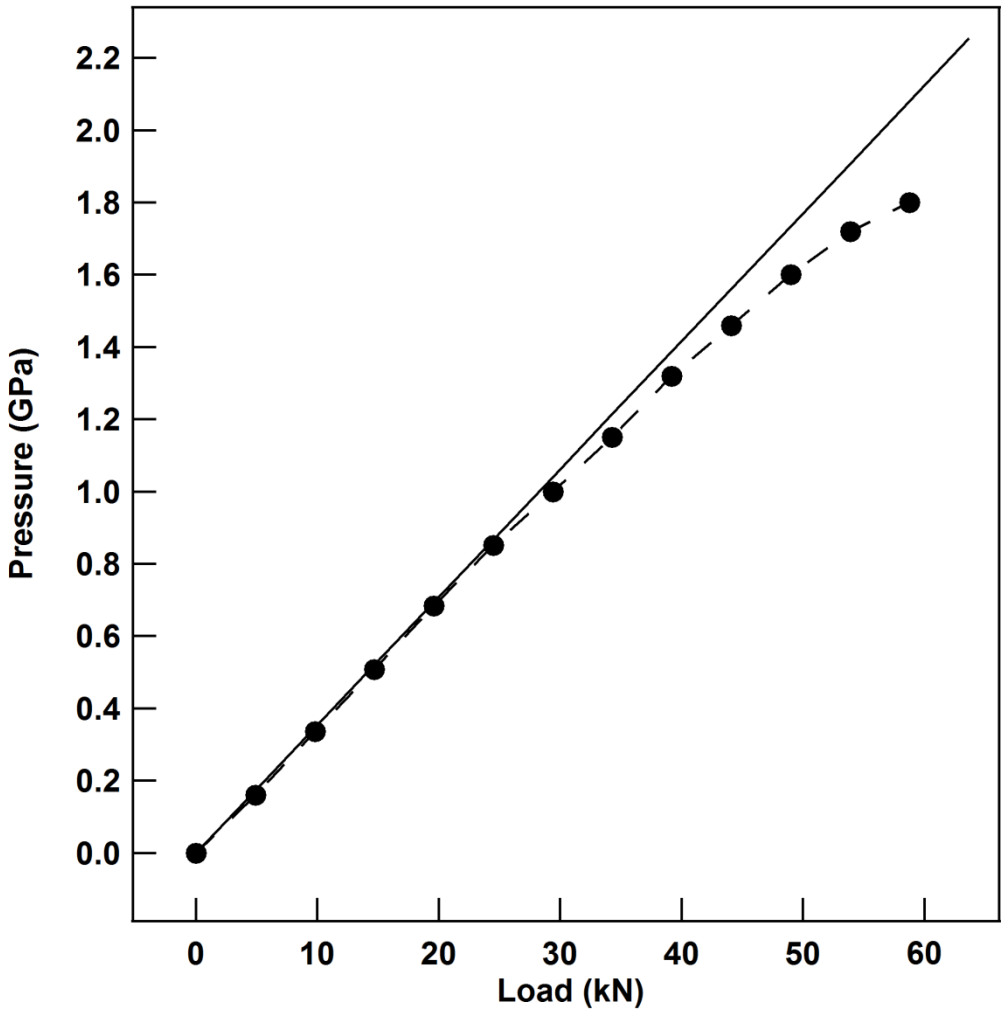

Figure 6.8 Pressure-load performance of the pressure cell. Solid symbols are experimental data. The error bars are smaller than the symbols.

The pressure in the cell at low temperature is usually lower than that at room temperature because the thermal expansion coefficient of the pressure cell is different from that of the pressure medium. However, the use of the manganin pressure gauge makes it possible to measure pressure at low temperature. The pressure at any given temperature below 352 K can be worked out from equation 6.5:

$$P(T) = \frac{R(P,T) - R(0,T)}{R(0,T) \times \alpha(T)} \tag{6.5}$$

where *P(T)* is the pressure at a given temperature, *R(P,T)* and *R(0,T)* is the resistance of the manganin pressure gauge at pressure *P* and at zero pressure, respectively, and *α(T)* is the pressure coefficient of the manganin wire at a given temperature. [32]

Therefore, to work out *P(T)*, one needs to know the value of *R(P,T)*, *R(0,T)* and *α(T)*. *R(P,T)* and *R(0,T)* data can be collected during temperature sweeps. The temperature dependence of the resistance of manganin pressure gauge was recorded using a data acquisition program prepared using Labview™. Figure 6.9 shows the temperature dependence of the resistance of manganin sensor for the pressure cell locked at 1.6 GPa at room temperature and a pressure cell cooled down at 0 GPa. A Lakeshore Cernox DT-470-Cu-12 thermometer was mounted on the outer sleeve close to the plug. Due to the size of the pressure cell, a temperature lag is expected during cooling or warming temperature sweeps. However, the cell was found to thermally equilibrate in reasonable time.

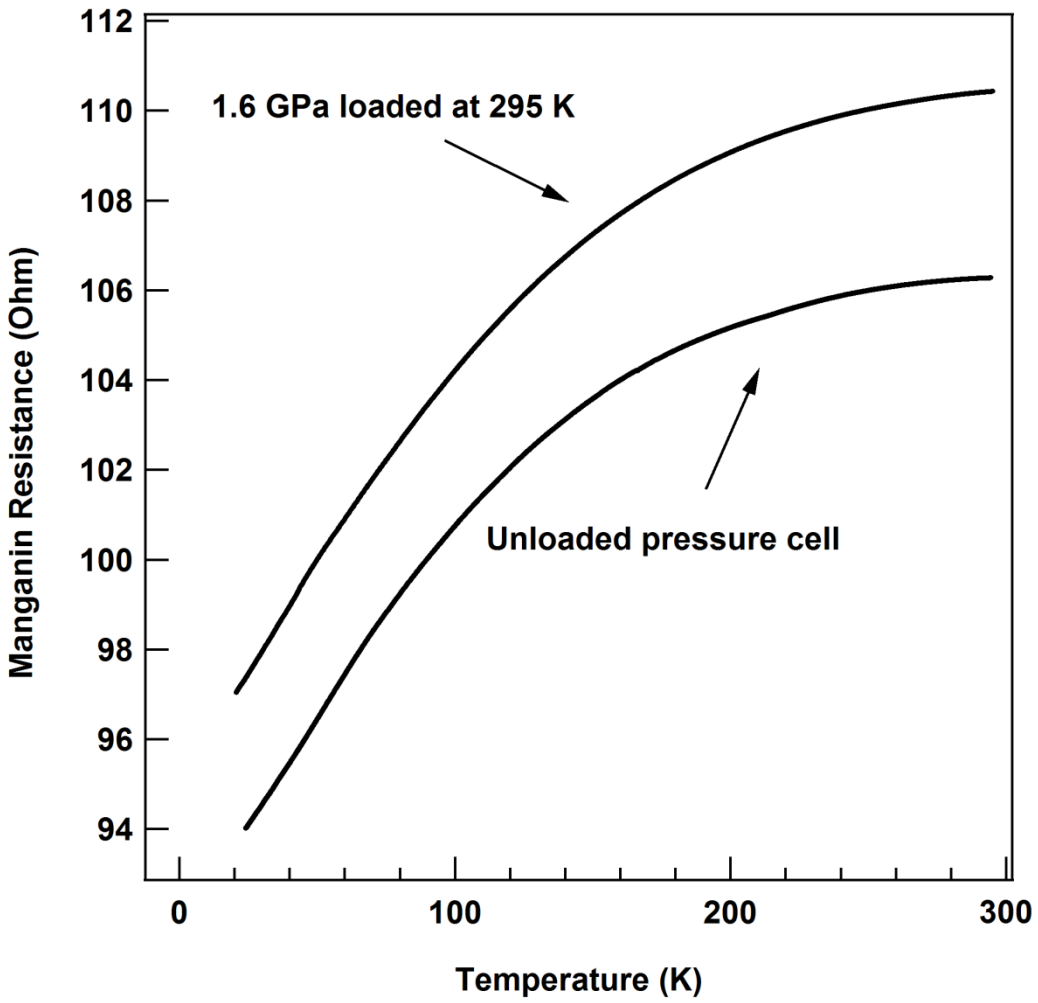

Figure 6.9 The electrical resistance of the manganin pressure gauge as a function of temperature for the pressurized and non-pressurized cell.

The temperature dependence of α is linear according to Dmowski and Litwin-Staszewska and can be expressed as:

$$\beta = \frac{\alpha(T)-\alpha(298K)}{\alpha(298K)\times(T-298K)} \tag{6.6}$$

where β is equal to -3.80×10^{-4} K^{-1} and 2.56×10^{-4} K^{-1} for temperature below and above 110 K, respectively.[33]

Several loading tests confirm α(298K) of our manganin pressure gauge is 0.0234 GPa^{-1} and $\alpha(T)$ for the base temperature can be calculated using equation 6.6. Knowing $R(P,T)$, $R(0,T)$ and $\alpha(T)$, the drop of the pressure at 20 K is estimated to be 0.15 GPa for Daphne 7373 oil and 0.20 GPa for the mixture of Fluorinert ™ 72 and 84 at a volume ratio of 1:1.

6.5 Neutron scattering experiments

INS measurements are commonly conducted using a neutron spectrometer such as the triple-axis-spectrometer or a backscattering spectrometer measuring the Bragg reflection from single crystals. In order to demonstrate the performance of the pressure cell, neutron scattering measurements were carried out on a single crystal of UGe_2 (RRR = 70, mosaic = 1.2 °) using the Panda cold three-axis spectrometer at the Forschungs-Neutronenquelle Heinz Maier-Leibnitz (FRMII), Germany. The single crystal was oriented with the a axis vertical. Hydrogen-free pressure medium, a mixture of Fluorinert™ 72 and 84 (volume ratio 1:1), was used as the pressure transmitting medium, which is a substitute of the mixture of Fluorinert™ 87 and 84 (volume ratio 1:1) since 3M does not supply Fluorinert™ 87 anymore that provides the sample with the best possible quasi-hydrostatic conditions over the whole range of pressures and temperatures.[33]

An open collimation was set up for the spectrometer to optimize the flux. Cooled beryllium filter was placed in the incident momentum side. The pressure cell was mounted on the cold plate of a standard 2 K close cycle refrigerator (CCR) and temperature was measured by a Cernox™ thermometer.

A rocking curve of the single crystal of UGe_2 (Figure 6.10) measured outside the pressure cell and under pressure of 1.4 GPa at room temperature at k = 2.282 $Å^{-1}$ was

used to determine the neutron transmission of the pressure cell for the thermal neutrons. The fullwidth at half maximum (FWHM) of the crystal broadening to 1.5 degree from 1.2 degree under pressure was observed. Once the pressure is released, the FWHM of the crystal is back to 1.2 degree, which indicates the change of the FWHM is pressure dependent. The ratio of the integrated intensities between 1.4 GPa and ambient pressure at Q = (0,0,1) is approximately 0.28 indicating a rather high neutron transmission for thermal neutrons. Q is defined in the reciprocal lattice unit (r.l.u) here and after.

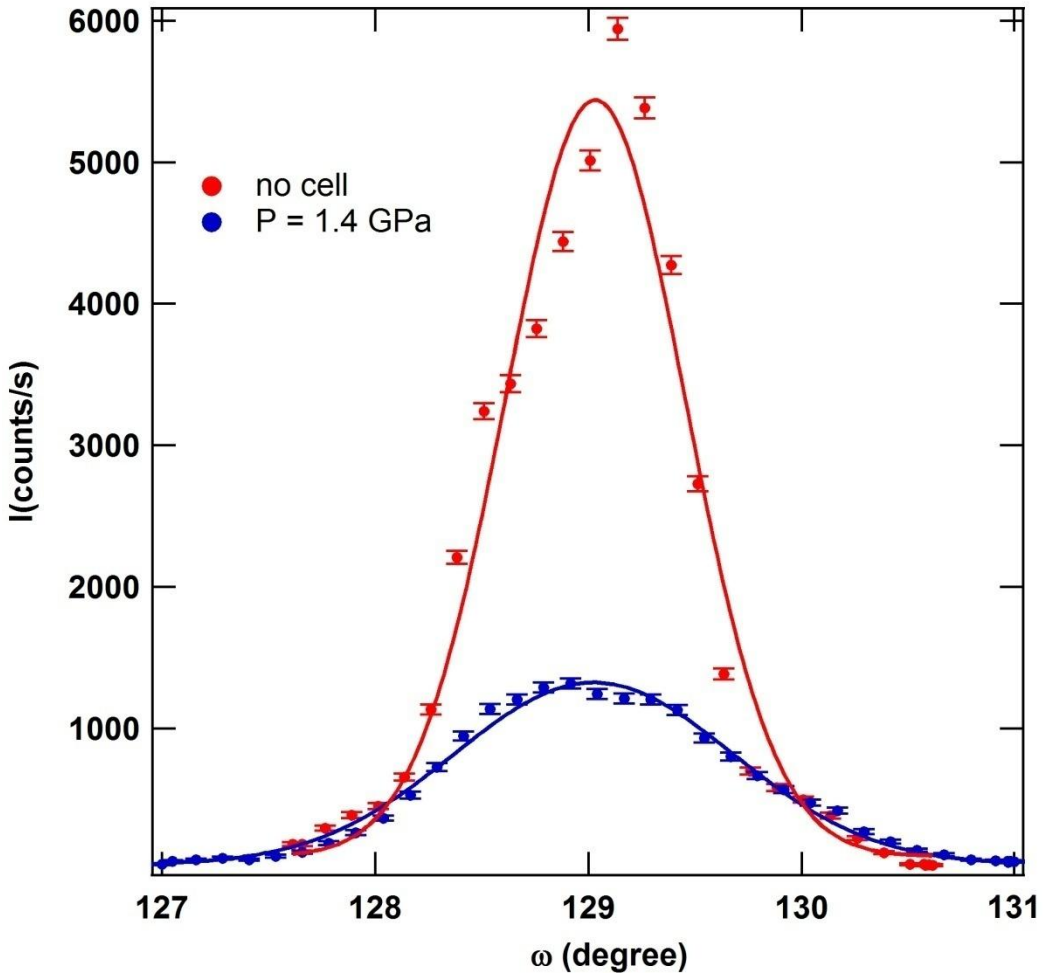

Figure 6.10 Rocking curve of UGe_2 at Q = (0,0,1), collected at T = 297 K at ambient pressure, no cell (empty circles) and at P = 1.4 GPa (filled circles). Transmission of the cell is 0.28.

The ratio of the integrated intensities for k = 1.141 Å^{-1} was also measured and the transmission for cold neutrons is approximately 0.09, which makes the collection times for inelastic experiments feasible.

In order to measure the temperature dependence of the magnetic wave-vector and to investigate the reciprocal space within the first Brillouin Zone near Q = (0,0,1), a series of elastic neutron scattering measurements were carried out. Longitudinal elastic scans through Q = (0,0,L) were conducted at temperatures between 3 K and 60 K.

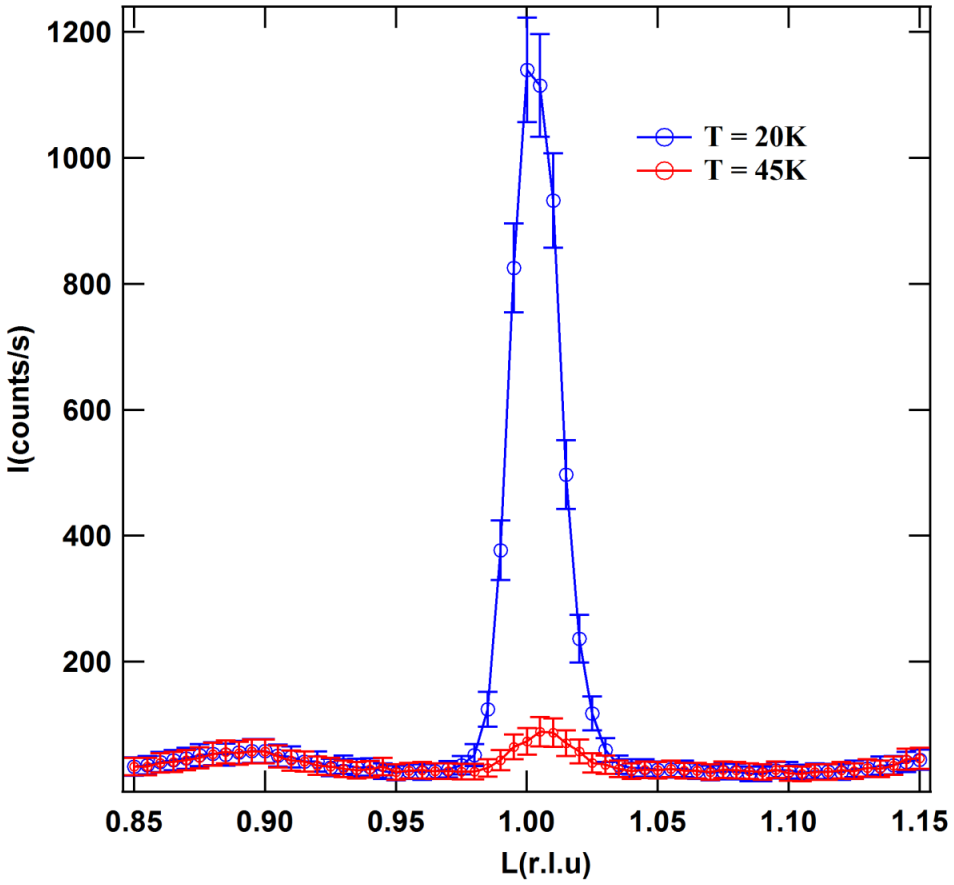

Figure 6.11 Elastic longitudinal scan at k_f = 1.141 Å^{-1} through Q = (0,0,L) in UGe_2 collected at temperatures above and below the Curie temperature (T_C = 37 K, at P = 1.1 GPa). Broad incommensurate features at L = (0,0,0.9) and L = (0,0,1.15) are powder rings most likely from Ni-Cr-Al alloy.

A higher temperature (60 K above the T_C) was used to measure the background. Figure 6.10 shows an increase of the intensity at (0,0,1) position in the reciprocal space indicates the onset of ferromagnetism in UGe_2. Much higher neutron intensity at 20 K is due to magnetic ordering which is expected. Due to a finite structure factor for (0,0,1), a small residual intensity at 45 K can be seen on the graph. Two broad features at Q = (0,0,0.85) and Q = (0,0,1.15) do not change with temperature. Rocking curves collected at Q = (0,0,0.85) and Q = (0,0,1.15) indicates these features were independent from the rotation of the UGe_2 single crystal. The source of these power rings were most likely from the CrNiAl alloy used to build the inner cylinder of the pressure cell.

The inelastic neutron scattering data collected at a pressure of 1.1 GPa is shown in Figure 6.12, which is a good illustration of the statistics that can be obtained during about 45 minutes data collection. The T_C of UGe_2 is reduced to 37 K, at which the magnetic scattering was expected to reach the maximum. The energy scans at Q = (0, 0. 1 - δ) at temperatures below and above T_C were plotted together with the data collected at T_C = 37 K.

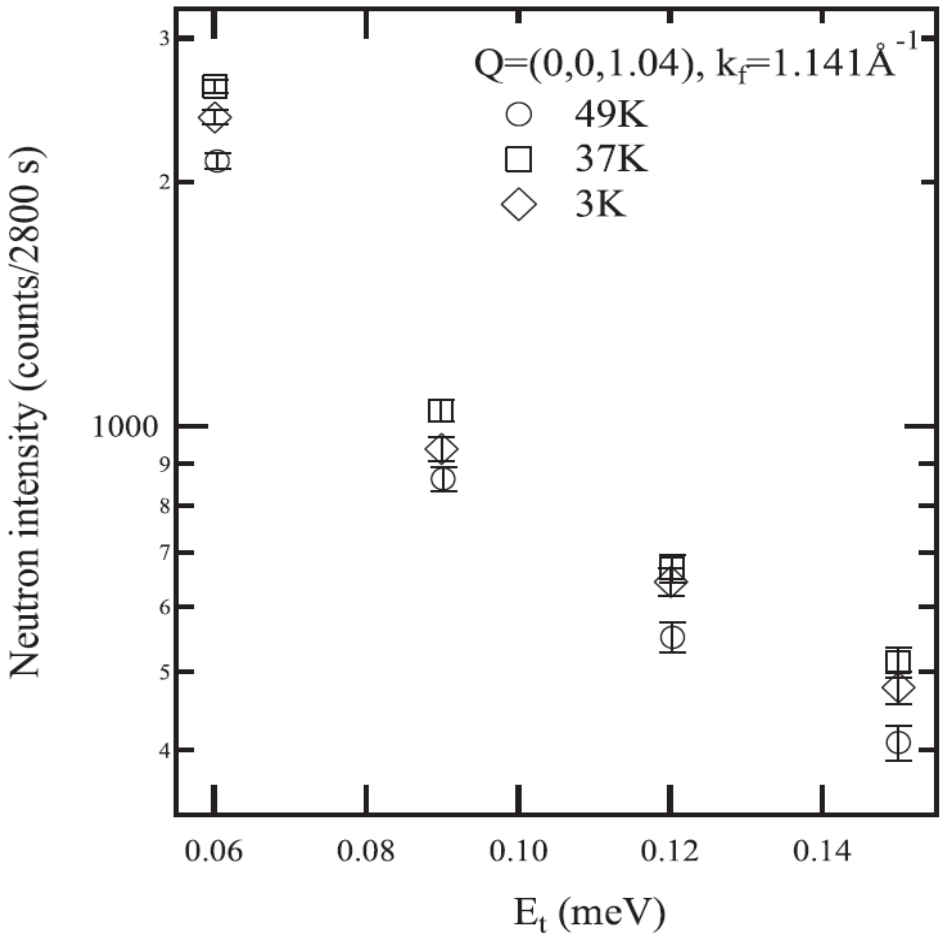

Figure 6.12 Magnetic critical scattering in UGe_2 under pressure. Energy scans performed at 1.1 GPa at Q = (0, 0. 1 - δ) at temperatures above and below T_C (T_C = 37 K).

6.6 Conclusions and future works

A pressure cell for inelastic neutron scattering measurements has been designed, manufactured and tested. The safe maximum pressure it can achieve is 1.8 GPa at room temperature, which covers the whole superconducting (P, T) phase diagram of UGe_2, providing access to the transition at P_x. The novel piston seal design eliminates the need in a PTFE capsule and makes use of the full bore diameter thus speeding up the data collection times. The manganin pressure gauge provides

accurate reading of pressure at any given temperature up to 352 K and eliminates the need in a pressure reference material present in the beam. The neutron scattering measurements at FRMII verified the results of the transmission calculation for warm neutrons and cold neutrons which is 0.28 and 0.09, respectively. The data collection times for INS experiment look reasonable.

Due to the limited beam time at FRMII, there is no more data to present. However, in order to probe the mechanism of the superconductivity, another INS measurement is proposed to carry out at the Rutherford Appleton Laboratory, Oxford, United Kingdom. In order to confirm the hypothesis that fluctuations associated with the critical end point of the first-order transition T_x within the ferromagnetic state play the crucial role in producing the superconductivity in UGe_2, the measurements of the relaxation rate and the inverse correlation length of these magnetic fluctuations will be carried out..

This research has led to the following publication:

W. Wang, D. A. Sokolov, A. D. Huxley and K. V. Kamenev, Rev. Sci. Instrument. **82**, 073903 (2011),

6.7 References

1. G. L. Squires, Introduction to the Theory of Thermal Neutron Scattering (Dover, 1997).

2. S. S. Saxena *et al.*, Nature **406**, 587 (2000).

3. A. Huxley *et al.*, Phys. Rev. B. **63**, 144519 (2001).

4. A. D. Huxley *et al.*, Phys. Rev. Lett. **91**, 207201 (2003).

5. S. Raymond *et al*., Physica B **350**, 33 (2004).

6. T. Hong *et al.*, Phys. Rev. B. **78**, 224409 (2008).

7. C. Pfleiderer *et al.*, J. Phys.: Condens. Matter **17**, S3111 (2005).

8. S. Klotz *et al.*, High Pressure Res. **14**, 249 (1996).

9. S. Klotz *et al.*, Hyperfine Interact. **128**, 245 (2000).

10. J. Paureau *et al*., Rev. Sci. Instrum. **46**, 11 (1975).

11. R. Done *et al.*, Rev. Sci. Instrum. **79**, 26107 (2008).

12. H. Taniguchi *et al.*, Rev. Sci. Instrum. **81**, 033903 (2010).

13. Y. Uwatoko *et al.*, J. Phys.: Condens. Matter **14**, 11291 (2002).

14. *ILL Clamped Cell 04PCL150CB5*; web-site: http://www.ill.eu/.

15. A. Sieber *et al.*, Phys. Rev. B: Condens. Matter **70**, 172413 (2004).

16. A. Sieber *et al*., Angew, Chem. Int. Ed. **44**, 4339 (2005).

17. D. L. Decker, J. Appl. Phys. **36**, 1 (1965).

18. A. Eiling *et al*., J. Phys. F: Met. Phys. **11**, 623 (1981).

19. *Kennametal Inc*.; web-site: http://www.kennametal.com/.

20. *NGK Berylco U.K. Ltd*.; web-site: http://www.ngkberylco.co.uk/.

21. Ni-Cr-Al alloy purchased from *R&D Support Co., Ltd*., in Japan (e-mail: rdsinfo@innocent-green.com).

22. B. V. Motovilov, *Precision Alloys*. (Moscow, 1983).

23. M. Eremets, High Pressure Experimental Methods. (Oxford, 1996).

24. *ANSYS*®, Inc.; web-site: http://www.ansys.com/.

25. *Solid Edge*; web-site: http://www.solidedge.com/.

26. *The equation of the total cross section per unit volume*. web-site: http://www.ncnr.nist.gov/resources/sldcalc.html

27. V.F. Sears, Neutron News, **3**, No. 3, pp. 29-37 (1992).

28. The 1/e neutron length calculator supplied by National Institute of Standards and Technology; web-site: http://www.ncnr.nist.gov/resources/sldcalc.html

29. I. R. Walker, Rev. Sci. Instrum. **70**, 8 (2000).

30. S. E. McLain *et al.*, e-print arXiv:condmat/0509194v1.

31. *Stycast 2850 FT and Catalyst 24 LV*; made by Emerson & Cumming Ltd.

32. L. H. Dmowski *et al*., Meas. Sci. Technol. **10**, 343 (1999).

33. V. A. Sidorov *et al*., J. Phys. Condens. Matter. **17**, S3005 (205).

Chapter 7 Conclusions and future prospects

The common theme of this work was the development of specialized instruments for studies of exotic superconductors such as UGe_2 and URhGe in which superconductivity coexists with ferromagnetism. There was a number of constrains imposed by the thermodynamic conditions as well as the sample dimensions that needed to be overcome in order to meet the objectives of this research. In the course of this research the following has been achieved:

- A two-axis rotating stage for use at sub-Kelvin temperatures and in high magnetic fields was designed, tested and used for studies of quantum oscillations in URhGe. The study has shown that the phase formation in the vicinity of the quantum critical point is enabled by the appearing of a Lifshitz transition. The next step to progress with this research is to couple the pressure cell with the rotating stage and study materials, such as UGe_2, in which QCP occurs at high pressure. The extra weight of the cell might require another development which would reduce the friction and replace the pivot with a sapphire jewel.

- A miniature turnbuckle diamond anvil cell for magnetisation and resistivity measurements at pressures of up to 10 GPa in various low-T and high-H systems and a gearbox for loading both cryogenic liquid and gas pressure medium are designed and tested. The pressure cell can be used in the MPMS, PPMS, and because of its small size can be adapted for the two-axis rotator.

- A two-layered piston cylinder high-pressure cell with pressure up to 2 GPa for inelastic neutron scattering measurements is designed and tested. The cell demonstrates the holistic approach to design of the sample environment. The sample space available inside the cell is designed for a large single crystal of UGe_2 available for studies. The wall thickness of the body of the cell was then made such that the cell can achieve the target pressure of 2 GPa needed to cover the important features on the pressure-temperature phase diagram, but the thickness of the walls of the cell were kept to the minimum to reduce the beam absorption by the cell.

- The resistivity of a PrNi single crystal studied under high-pressure up to 9 GPa shows The critical transition temperature rises with the increasing pressure at a rate of 0.87 K per GPa. The quantity $\Delta(\frac{\partial \rho}{\partial T})$ was found to increase with pressure.

Appendix

Appendix A Technical drawings

A1 The two-axis rotating stage

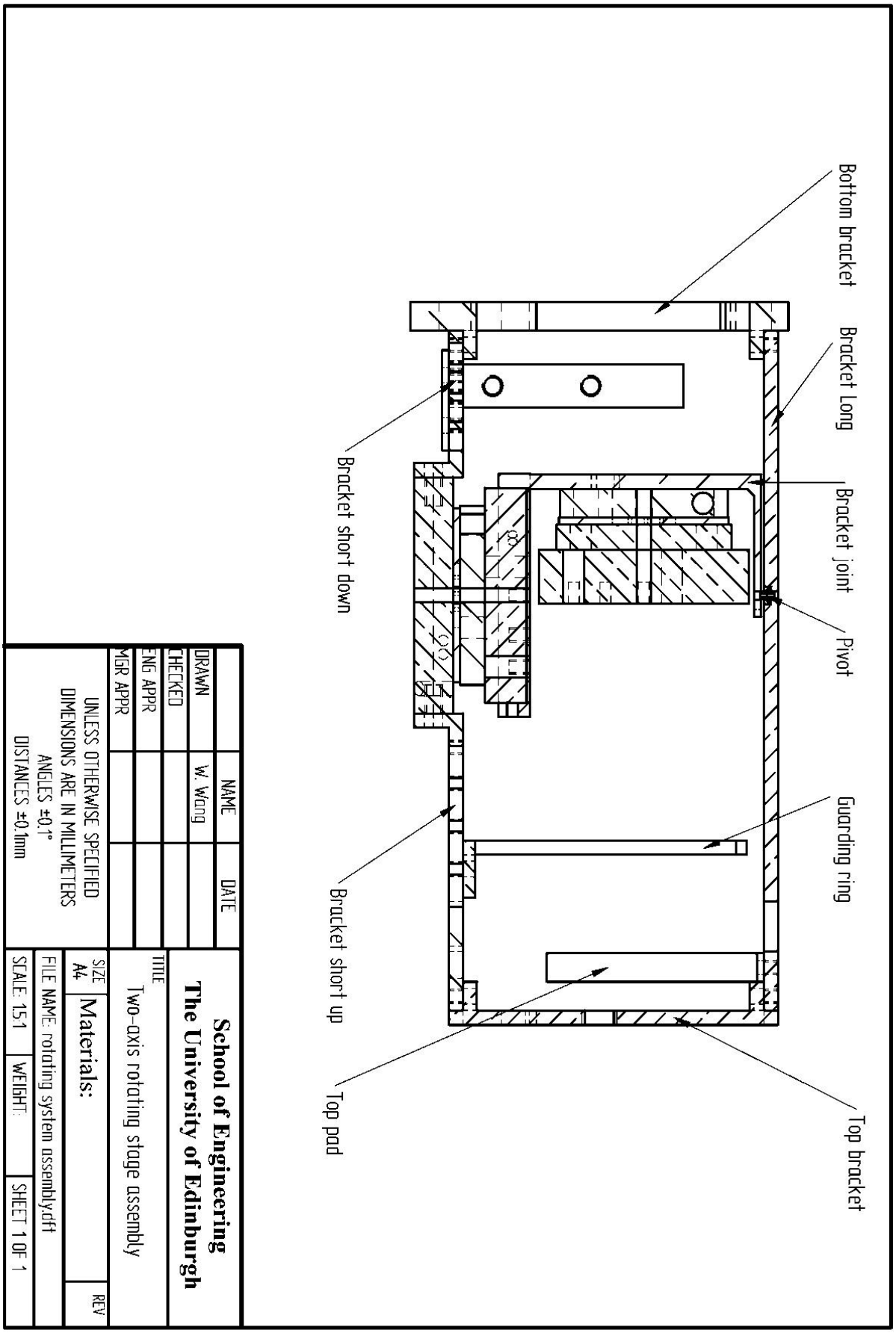
Bottom bracket
Bracket Long
Bracket joint
Pivot
Guarding ring
Top bracket
Bracket short down
Bracket short up
Top pad
NAME
DATE
DRAWN
W. Wang
CHECKED
ENG APPR
MGR APPR
UNLESS OTHERWISE SPECIFIED
DIMENSIONS ARE IN MILLIMETERS
ANGLES ±0.1°
DISTANCES ±0.1mm
School of Engineering
The University of Edinburgh
TITLE
Two-axis rotating stage assembly
SIZE
A4
Materials:
REV
FILE NAME: rotating system assembly.dft
SCALE: 1:5:1
WEIGHT:
SHEET 1 OF 1

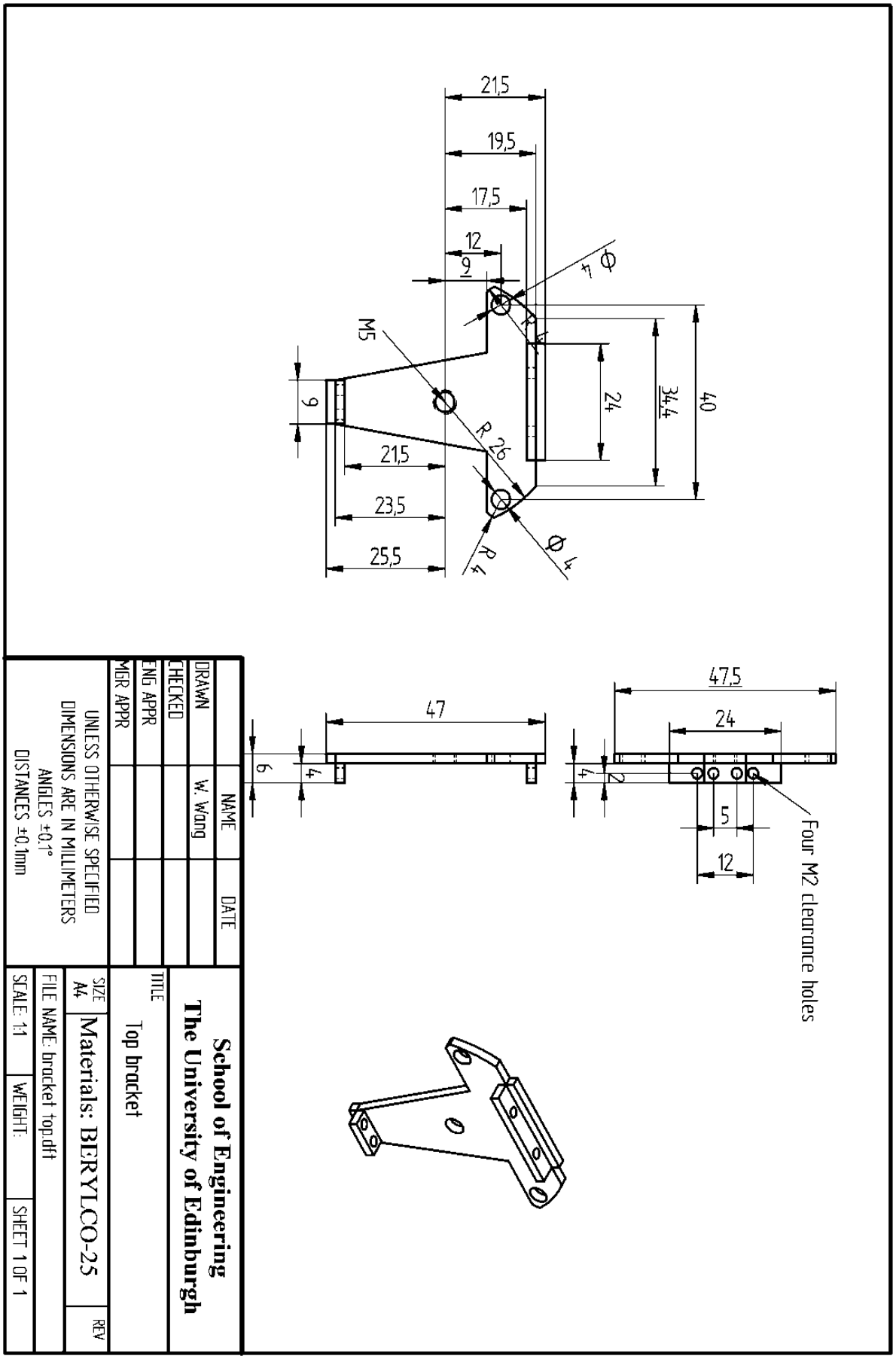
21,5
19,5
17,5
12
9
Φ 4
R 4
M5
9
R 26
21,5
23,5
25,5
R 4
Φ 4
24
34,4
40
47
6
4
47,5
24
4
2
5
12
Four M2 clearance holes
School of Engineering
The University of Edinburgh
NAME
DATE
DRAWN
W. Wang
CHECKED
ENG APPR
MGR APPR
UNLESS OTHERWISE SPECIFIED
DIMENSIONS ARE IN MILLIMETERS
ANGLES ±0.1°
DISTANCES ±0.1mm
TITLE
Top bracket
SIZE
A4
Materials: BERYLCO-25
REV
FILE NAME: bracket top.dft
SCALE: 1:1
WEIGHT:
SHEET 1 OF 1

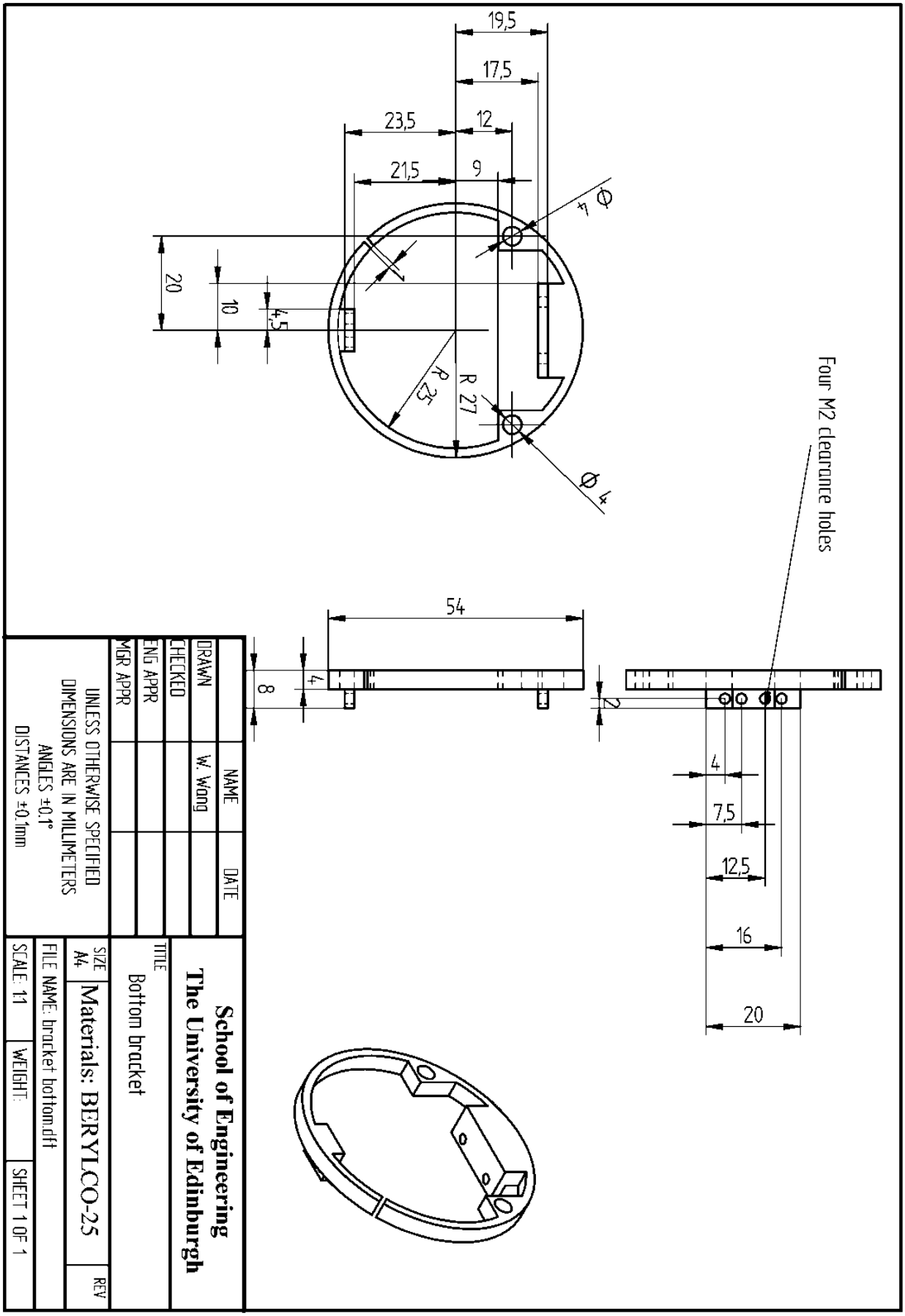
19,5
17,5
23,5
12
21,5
9
Ø 4
20
10
4,5
R 23
R 27
Ø 4
Four M2 clearance holes
54
8
4
2
4
7,5
12,5
16
20
School of Engineering
The University of Edinburgh
DRAWN
W. Wong
CHECKED
ENG APPR
MGR APPR
NAME
DATE
UNLESS OTHERWISE SPECIFIED
DIMENSIONS ARE IN MILLIMETERS
ANGLES ±0.1°
DISTANCES ±0.1mm
TITLE
Bottom bracket
SIZE
A4
Materials: BERYLCO-25
REV
FILE NAME: bracket bottom.dft
SCALE: 11
WEIGHT:
SHEET 1 OF 1

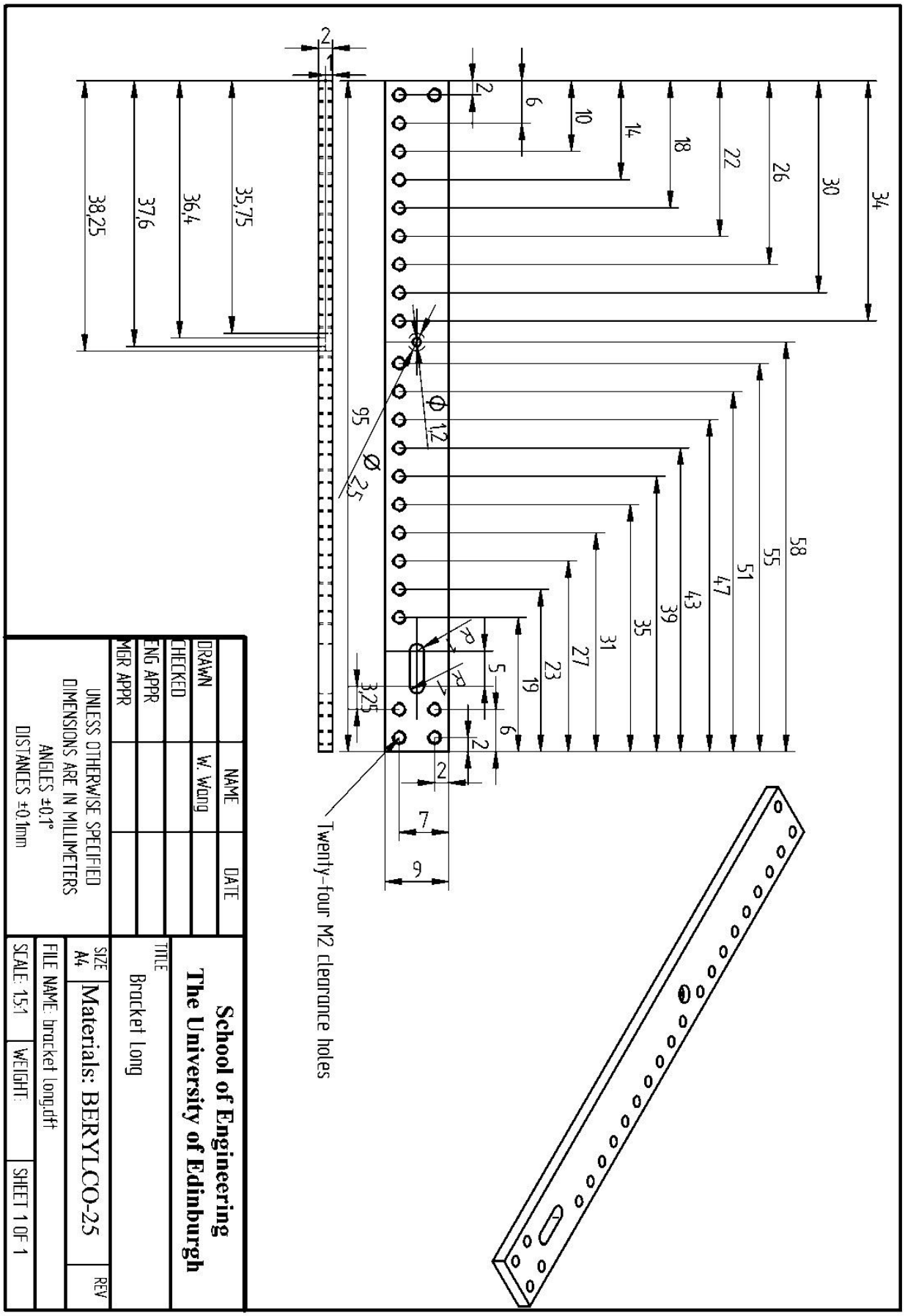
Twenty-four M2 clearance holes
Ø 12
Ø 25
95
38,25
37,6
36,4
35,75
34
30
26
22
18
14
10
6
2
58
55
51
47
43
39
35
31
27
23
19
7
9
3,25
5
NAME
DATE
DRAWN
W. Wang
CHECKED
ENG APPR
MGR APPR
UNLESS OTHERWISE SPECIFIED
DIMENSIONS ARE IN MILLIMETERS
ANGLES ±0.1°
DISTANCES ±0.1mm
School of Engineering
The University of Edinburgh
TITLE
Bracket Long
SIZE
A4
Materials: BERYLCO-25
REV
FILE NAME: bracket long.dft
SCALE: 1:1
WEIGHT:
SHEET 1 OF 1

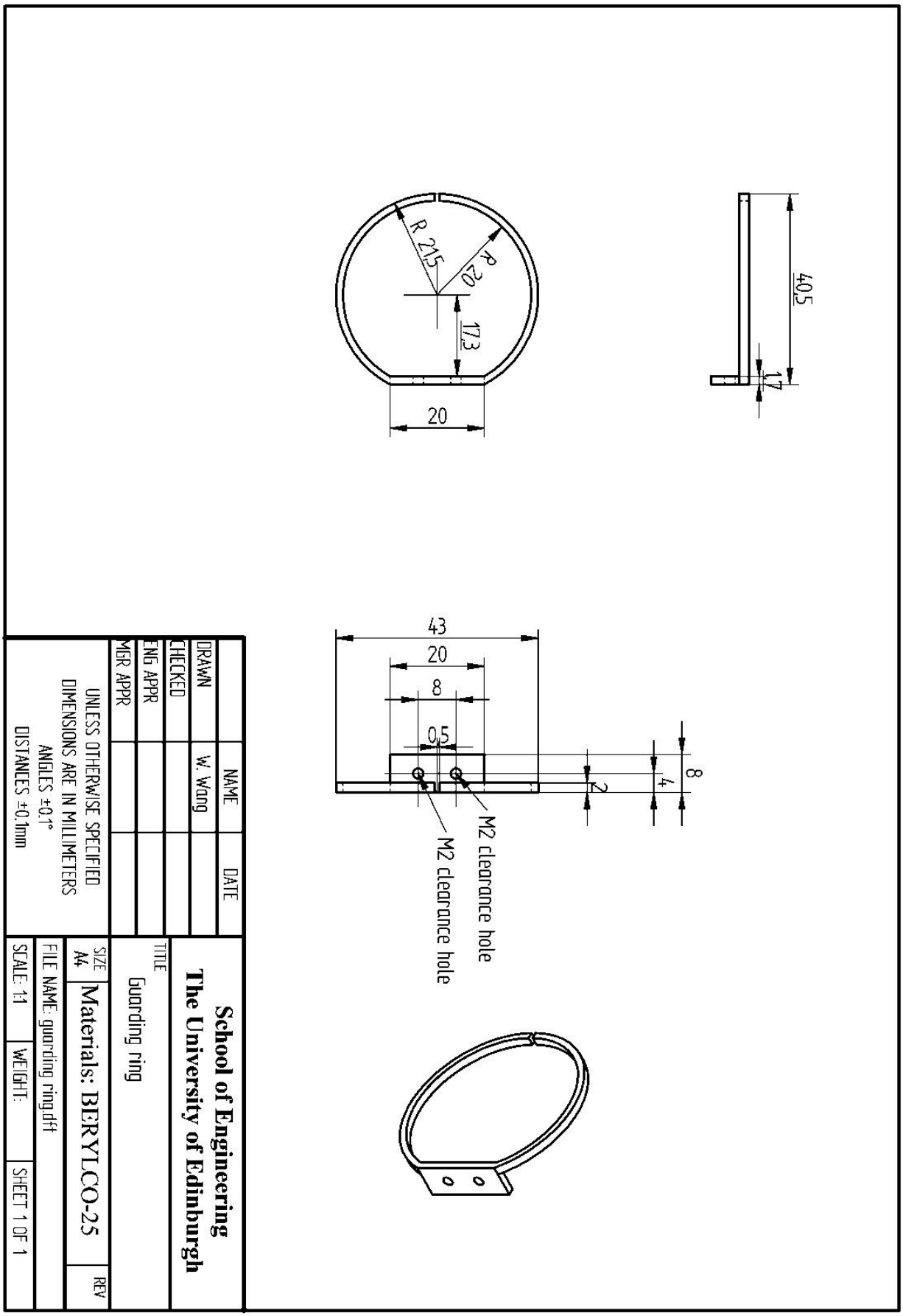
40.5
17
R 21.5
R 20
17.3
20
43
20
8
0.5
2
4
8
M2 clearance hole
M2 clearance hole
School of Engineering
The University of Edinburgh
NAME
DATE
DRAWN
W. Wang
CHECKED
ENG APPR
MGR APPR
UNLESS OTHERWISE SPECIFIED
DIMENSIONS ARE IN MILLIMETERS
ANGLES ±0.1°
DISTANCES ±0.1mm
TITLE
Guarding ring
SIZE
A4
Materials: BERYLCO-25
REV
FILE NAME: guarding ring.dft
SCALE: 1:1
WEIGHT:
SHEET 1 OF 1

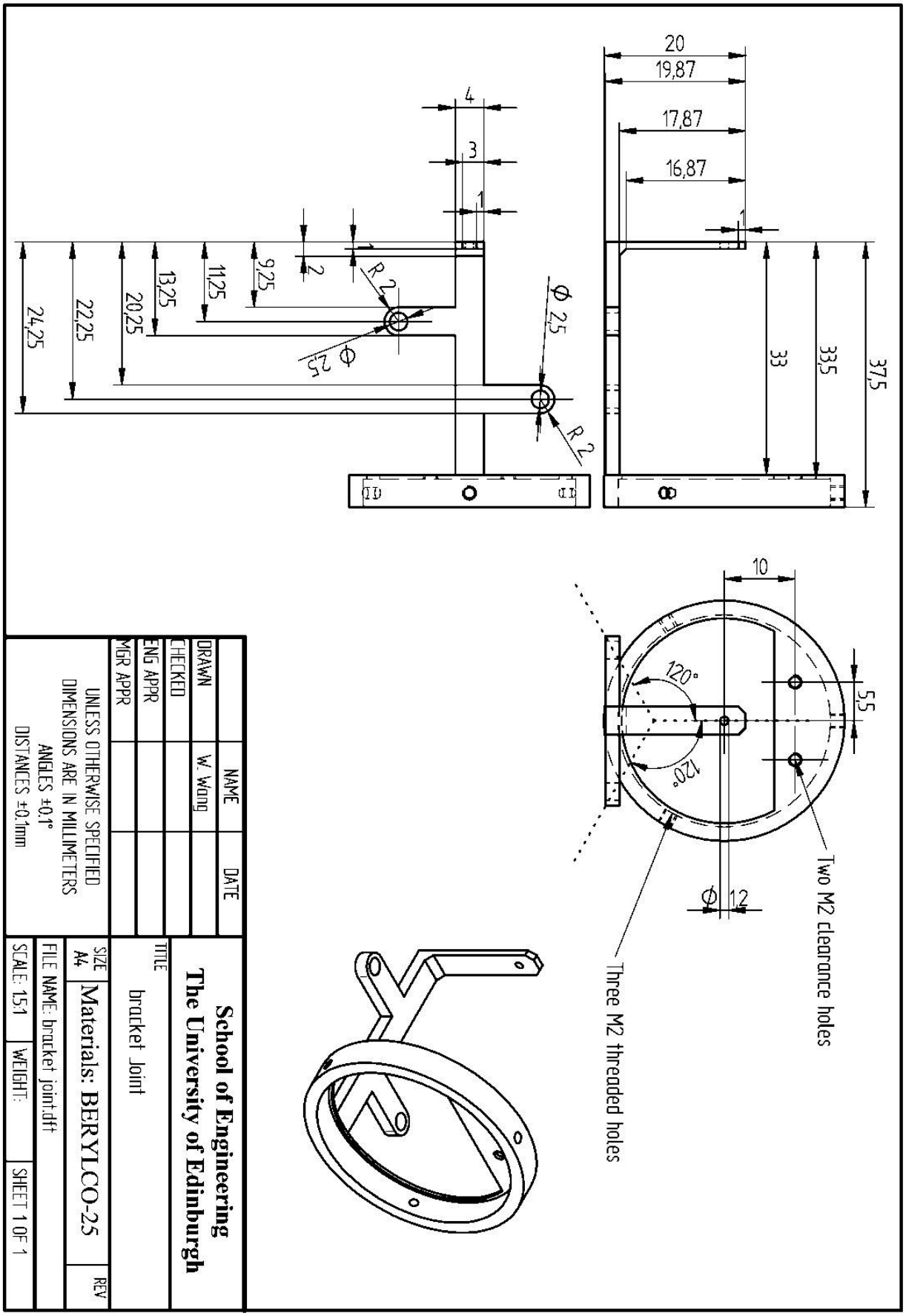
20
19,87
17,87
16,87
4
3
1
33
33,5
37,5
24,25
22,25
20,25
13,25
11,25
9,25
2
R 2
Φ 25
Φ 12
10
120°
5,5
Two M2 clearance holes
Three M2 threaded holes
School of Engineering
The University of Edinburgh
NAME
DATE
DRAWN
W. Wang
CHECKED
ENG APPR
MGR APPR
UNLESS OTHERWISE SPECIFIED
DIMENSIONS ARE IN MILLIMETERS
ANGLES ±0.1°
DISTANCES ±0.1mm
TITLE
bracket Joint
SIZE
A4
Materials: BERYLCO-25
REV
FILE NAME: bracket joint.dft
SCALE: 1:1
WEIGHT:
SHEET 1 OF 1

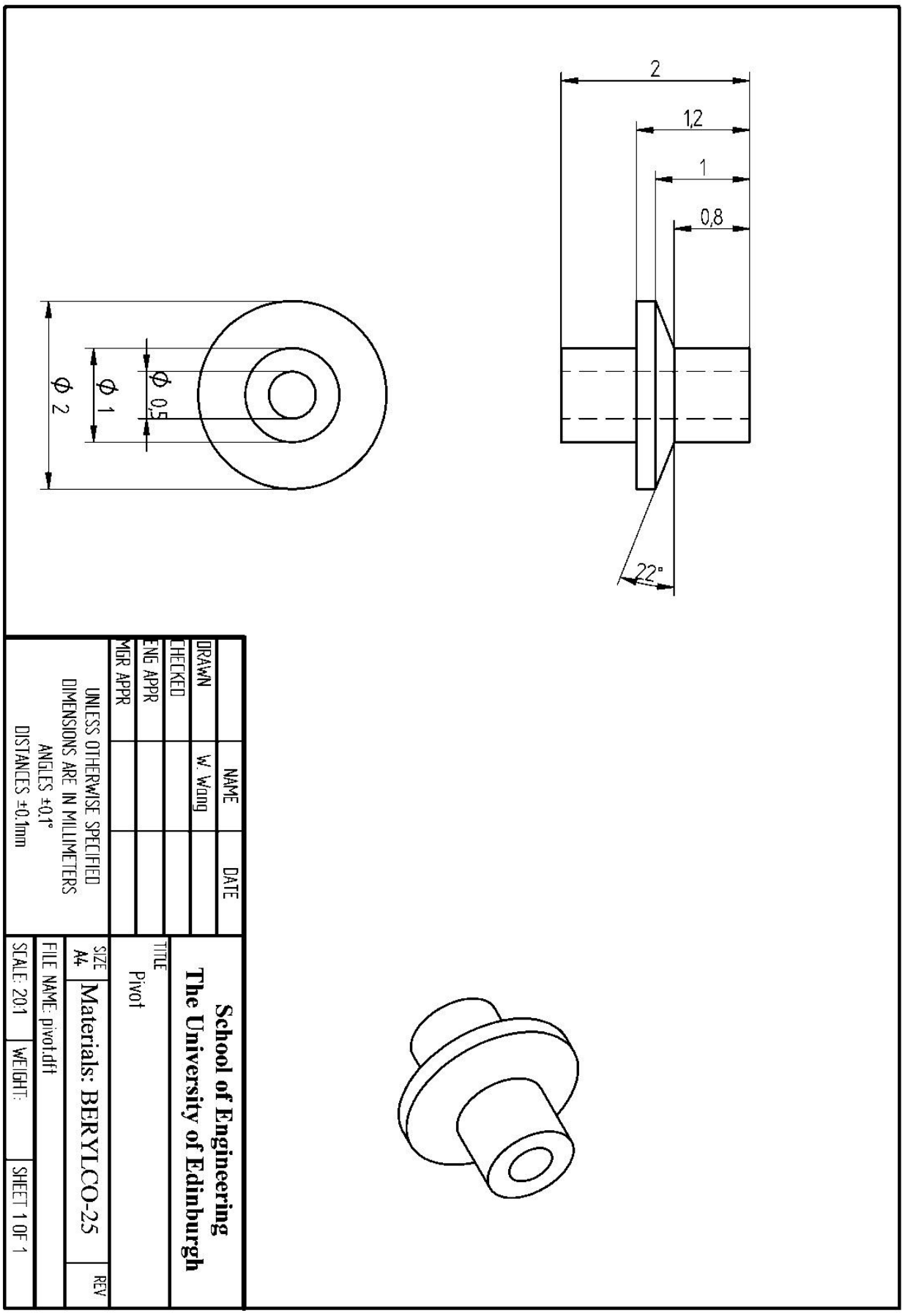
2
1,2
1
0,8
22°
ϕ 2
ϕ 1
ϕ 0,5
School of Engineering
The University of Edinburgh
NAME
DATE
W. Wang
DRAWN
CHECKED
ENG APPR
MGR APPR
UNLESS OTHERWISE SPECIFIED
DIMENSIONS ARE IN MILLIMETERS
ANGLES ±0.1°
DISTANCES ±0.1mm
TITLE
Pivot
SIZE
A4
Materials: BERYLCO-25
REV
FILE NAME: pivot.dft
SCALE: 20:1
WEIGHT:
SHEET 1 OF 1

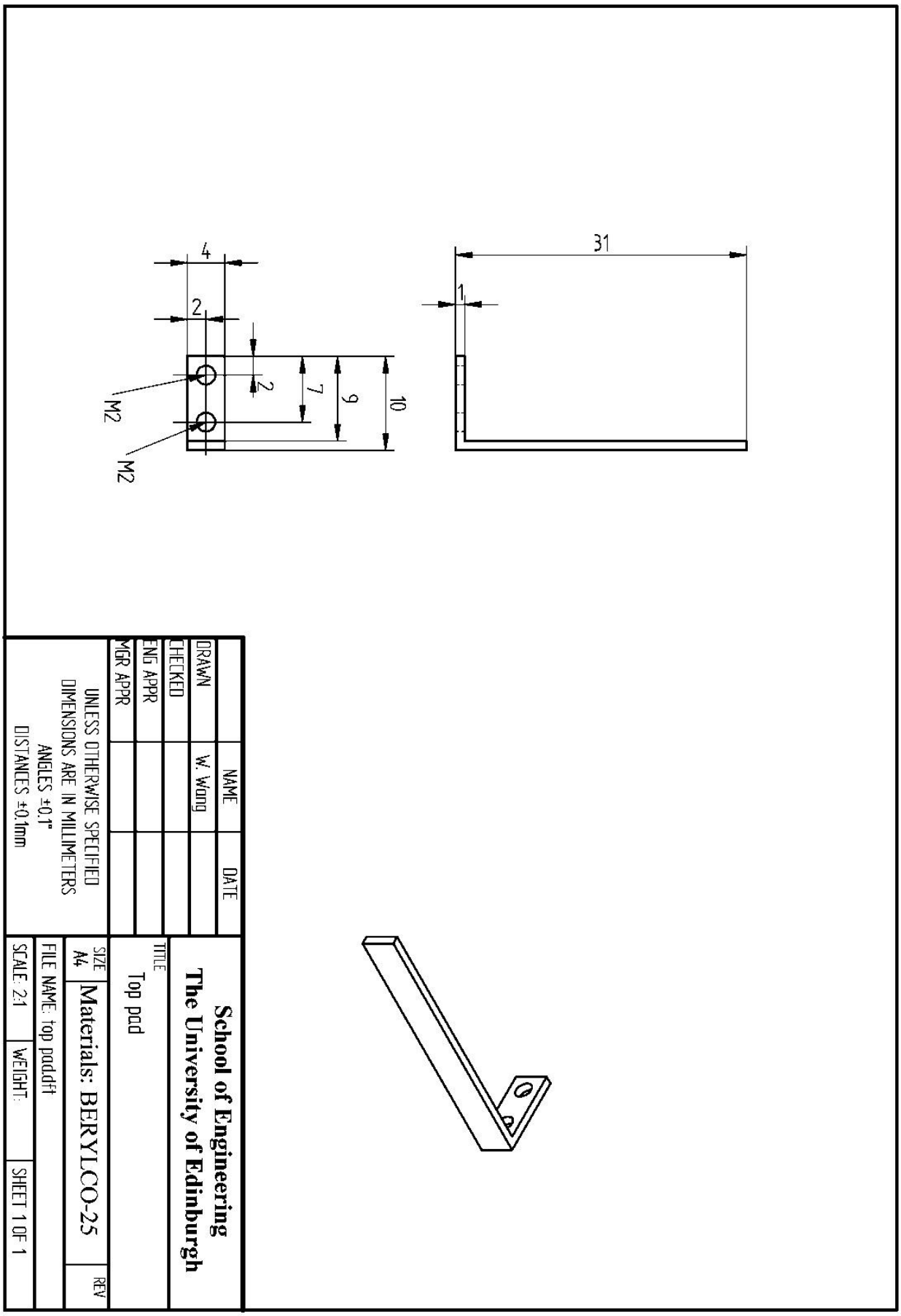
4
2
2
7
9
10
M2
M2
31
1
School of Engineering
The University of Edinburgh
NAME
DATE
DRAWN
W. Wong
CHECKED
ENG APPR
MGR APPR
UNLESS OTHERWISE SPECIFIED
DIMENSIONS ARE IN MILLIMETERS
ANGLES ±0.1°
DISTANCES ±0.1mm
TITLE
Top pad
SIZE
A4
Materials: BERYLCO-25
REV
FILE NAME: top pad.dft
SCALE: 2:1
WEIGHT:
SHEET 1 OF 1

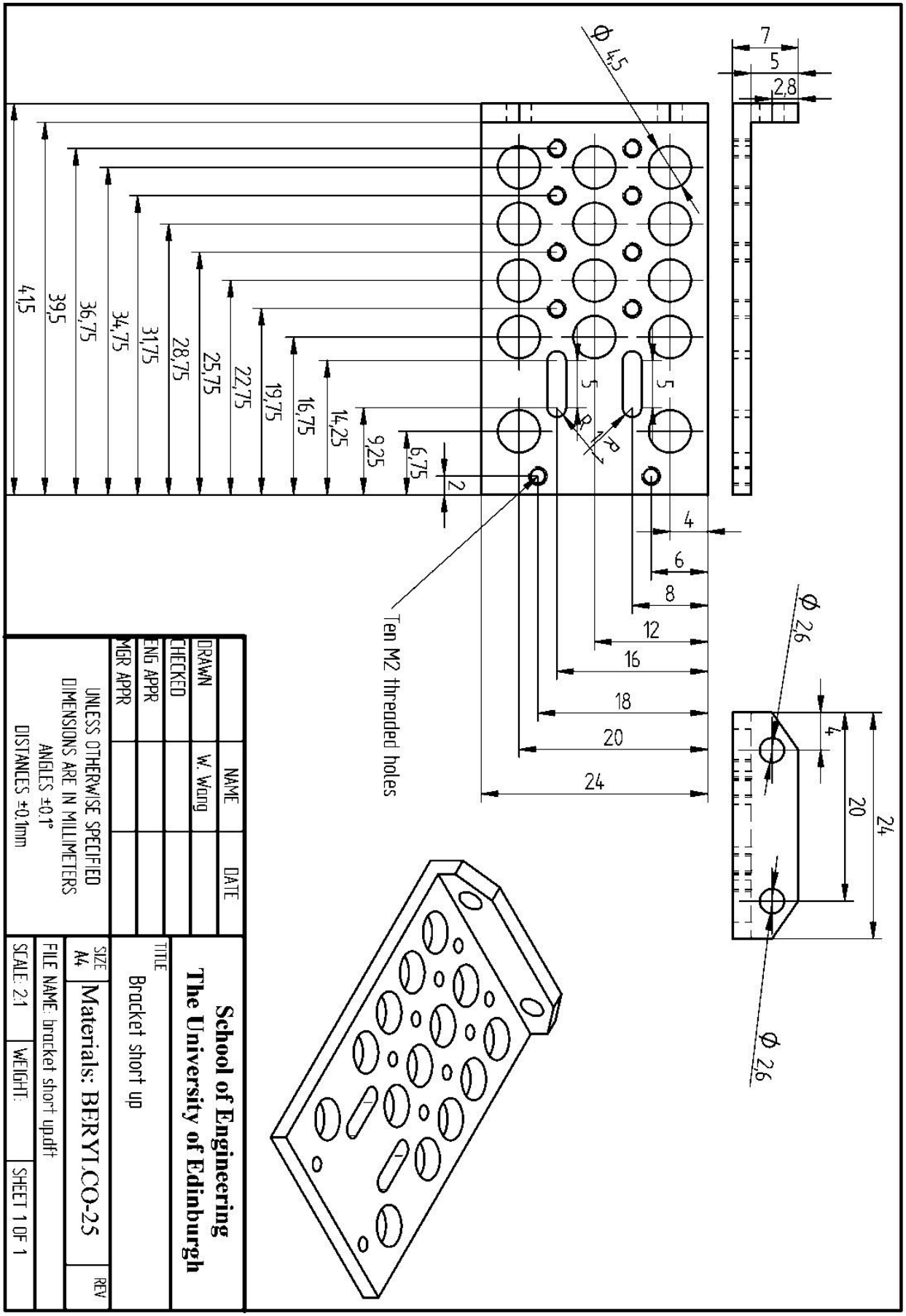
Ø 4,5
7
5
2,8
41,5
39,5
36,75
34,75
31,75
28,75
25,75
22,75
19,75
16,75
14,25
9,25
6,75
2
5
5
8
R
4
6
8
12
16
18
20
24
Ten M2 threaded holes
Ø 26
4
20
24
Ø 26
DRAWN
W. Wong
CHECKED
ENG APPR
MGR APPR
NAME
DATE
UNLESS OTHERWISE SPECIFIED
DIMENSIONS ARE IN MILLIMETERS
ANGLES ±0.1°
DISTANCES ±0.1mm
School of Engineering
The University of Edinburgh
TITLE
Bracket short up
SIZE
A4
Materials: BERYLCO-25
REV
FILE NAME: bracket short up.dft
SCALE: 2:1
WEIGHT:
SHEET 1 OF 1

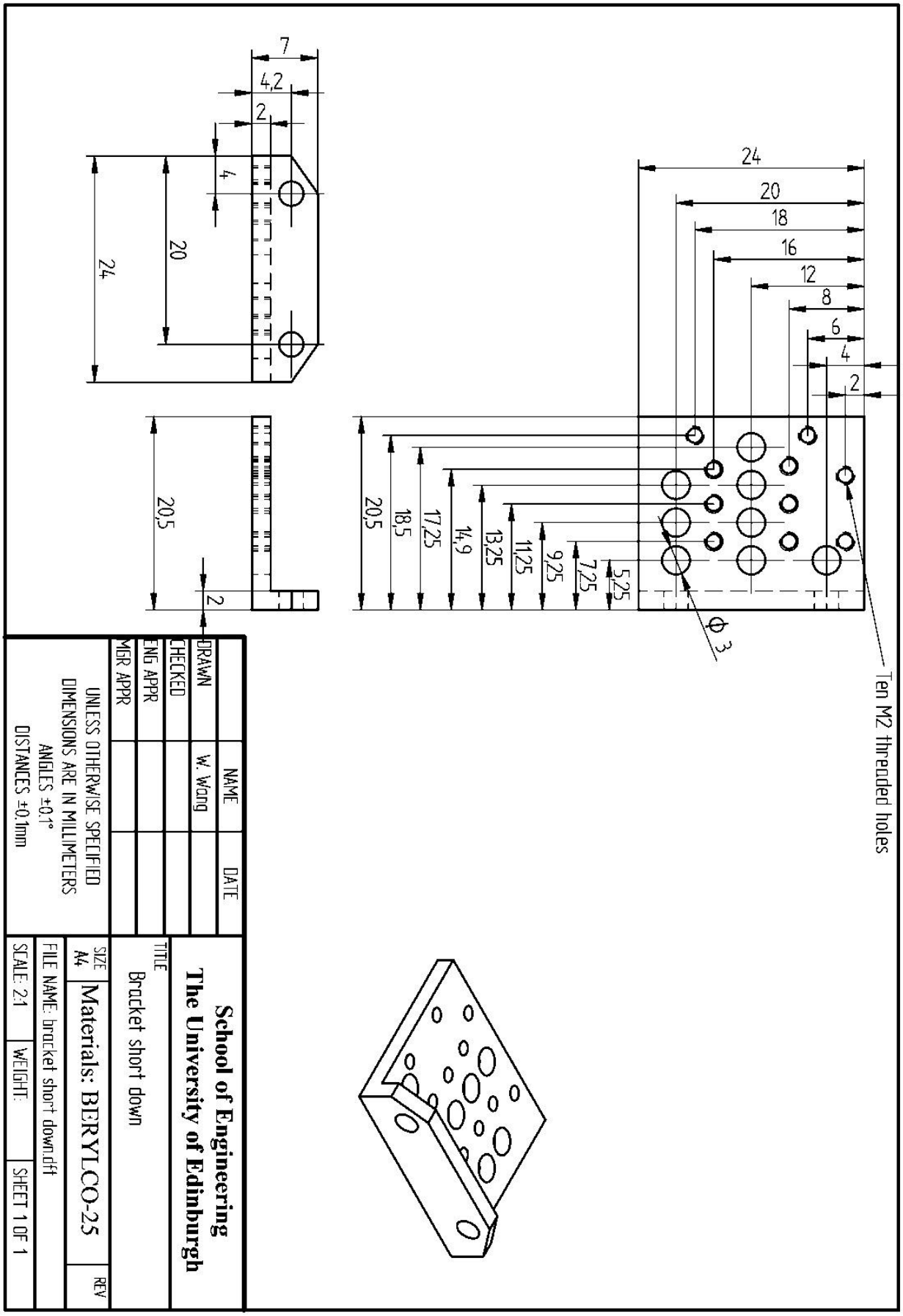
7
4,2
2
4
20
24
20,5
2
24
20
18
16
12
8
6
4
2
20,5
18,5
17,25
14,9
13,25
11,25
9,25
7,25
5,25
ϕ 3
Ten M2 threaded holes
School of Engineering
The University of Edinburgh
NAME
DATE
DRAWN
W. Wang
CHECKED
ENG APPR
MGR APPR
UNLESS OTHERWISE SPECIFIED
DIMENSIONS ARE IN MILLIMETERS
ANGLES ±0.1°
DISTANCES ±0.1mm
TITLE
Bracket short down
SIZE
A4
Materials: BERYLCO-25
REV
FILE NAME: bracket short down.dft
SCALE: 2:1
WEIGHT:
SHEET 1 OF 1

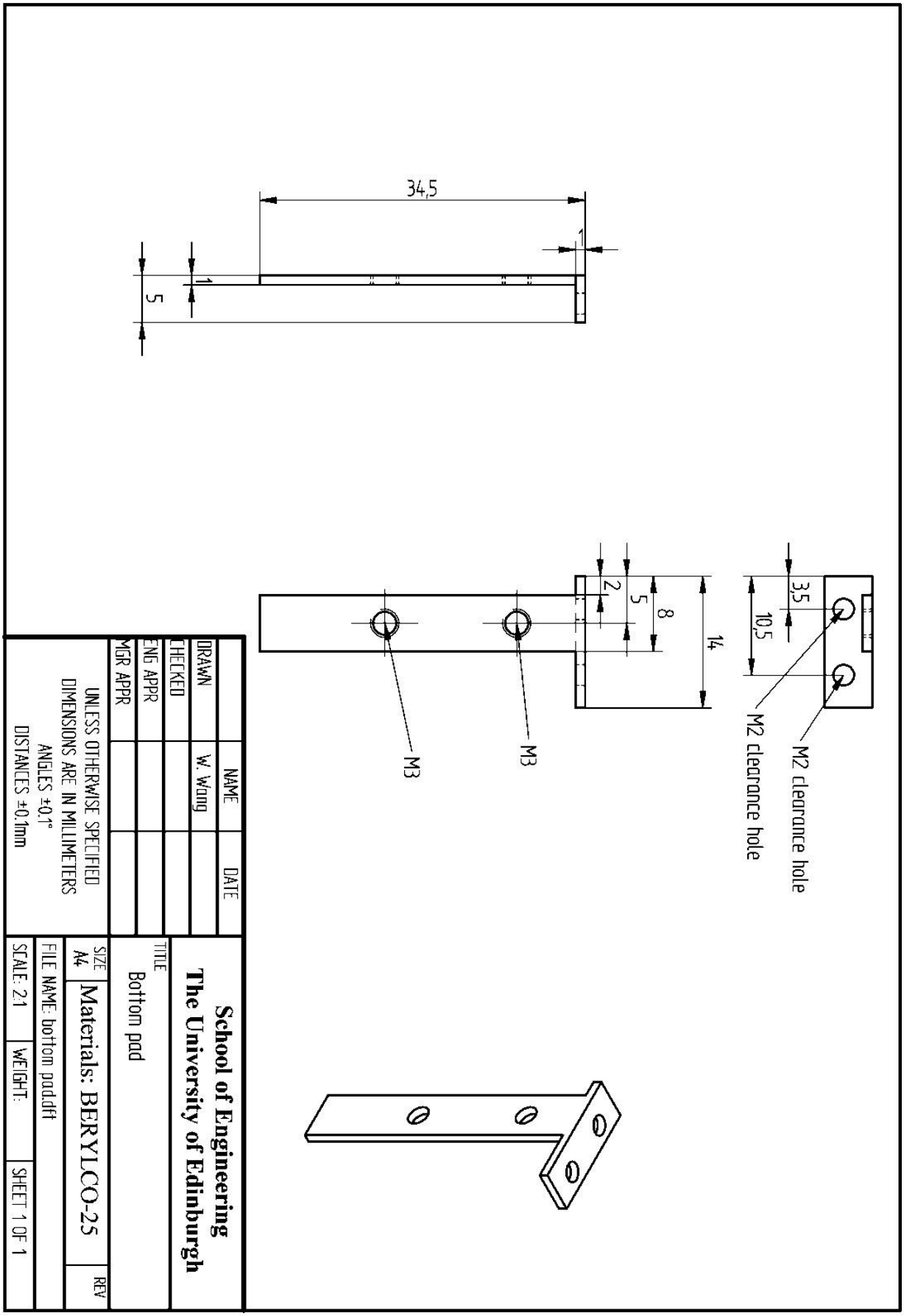

	NAME	DATE
DRAWN	W. Wang	
CHECKED		
ENG APPR		
MGR APPR		

UNLESS OTHERWISE SPECIFIED
DIMENSIONS ARE IN MILLIMETERS
ANGLES ±0.1°
DISTANCES ±0.1mm

School of Engineering
The University of Edinburgh

TITLE
Bottom pad

SIZE A4 | Materials: BERYLCO-25 | REV

FILE NAME: bottom pad.dft

SCALE: 2:1 | WEIGHT: | SHEET 1 OF 1

A2 The turnbuckle diamond anvil cell and gearbo

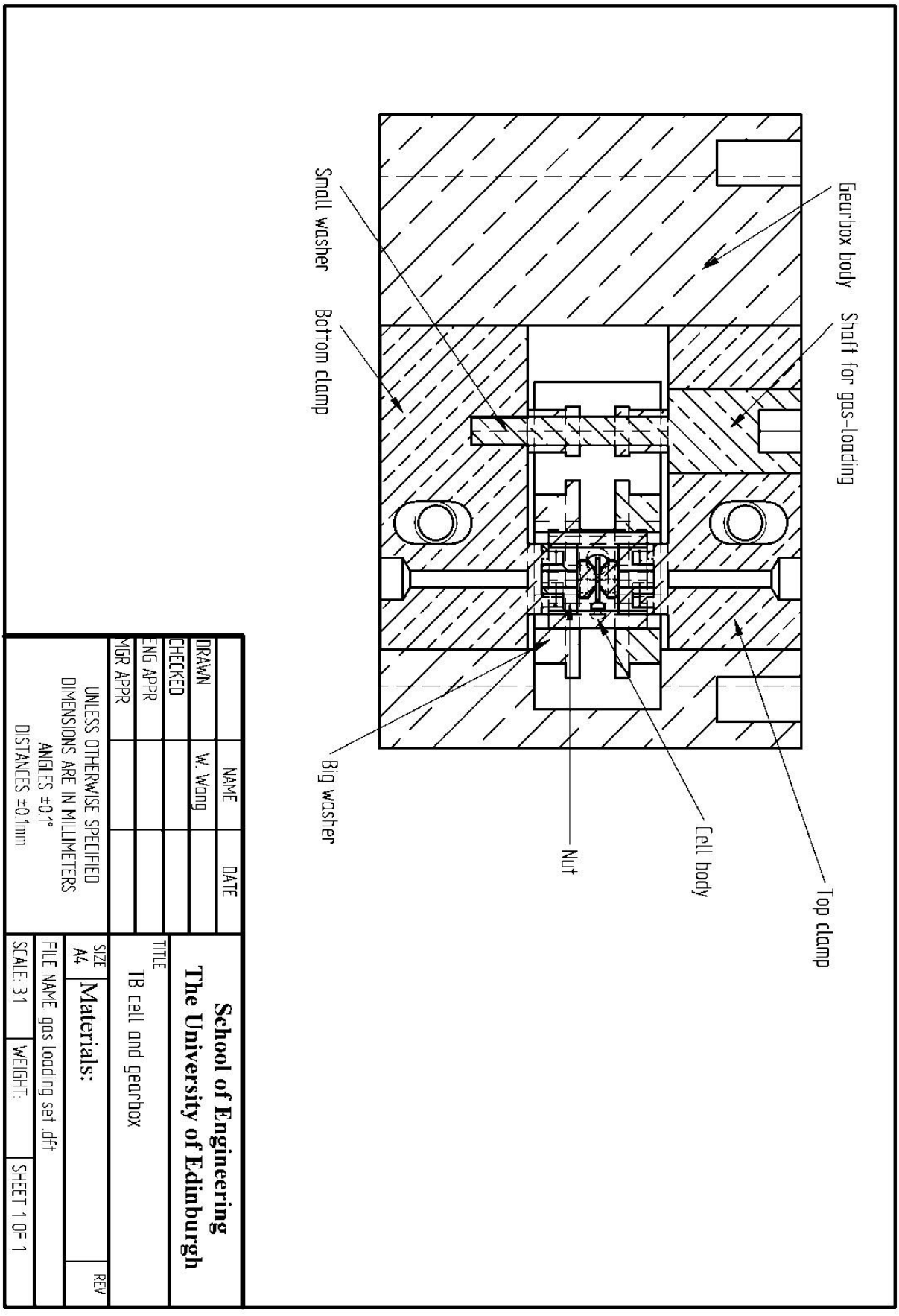
Gearbox body
Shaft for gas-loading
Small washer
Bottom clamp
Big washer
Nut
Cell body
Top clamp
NAME
DATE
DRAWN
W. Wang
CHECKED
ENG APPR
MGR APPR
UNLESS OTHERWISE SPECIFIED
DIMENSIONS ARE IN MILLIMETERS
ANGLES ±0.1°
DISTANCES ±0.1mm
School of Engineering
The University of Edinburgh
TITLE
TB cell and gearbox
SIZE
A4
Materials:
REV
FILE NAME gas loading set dft
SCALE: 3:1
WEIGHT:
SHEET 1 OF 1

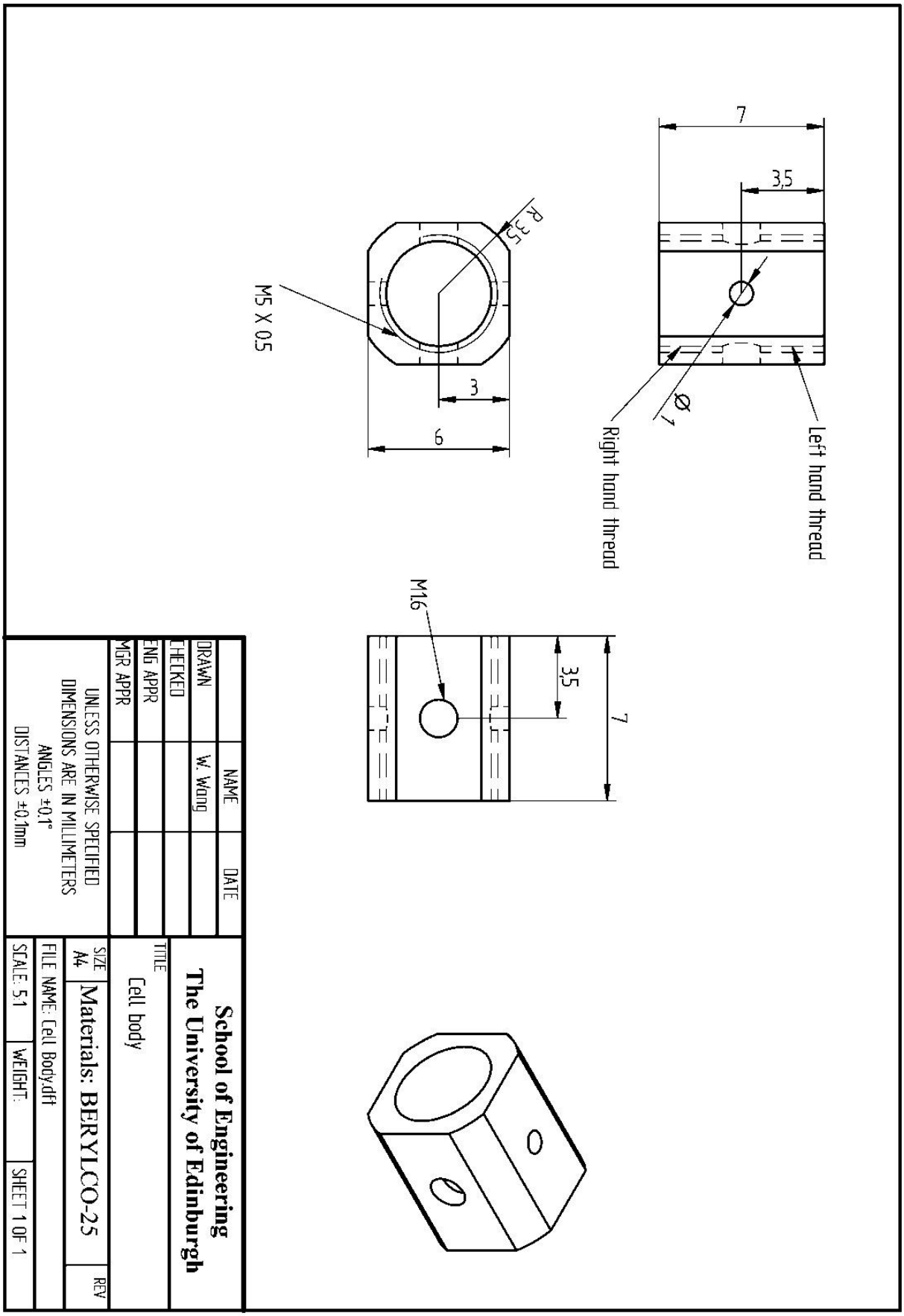
7
3,5
Right hand thread
Left hand thread
M5 X 0.5
3
6
M16
3,5
7
School of Engineering
The University of Edinburgh
NAME
DATE
DRAWN
W. Wang
CHECKED
ENG APPR
MGR APPR
UNLESS OTHERWISE SPECIFIED
DIMENSIONS ARE IN MILLIMETERS
ANGLES ±0.1°
DISTANCES ±0.1mm
TITLE
Cell body
SIZE
A4
Materials: BERYLCO-25
REV
FILE NAME: Cell Body.dft
SCALE: 5:1
WEIGHT:
SHEET 1 OF 1

2 OFF

One is machined with left hand thread, the other machined with right hand thread.

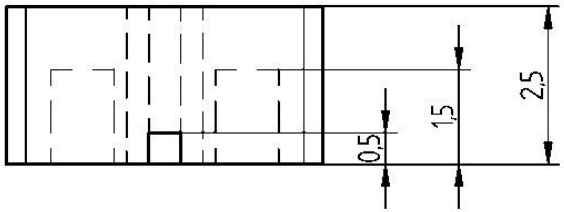

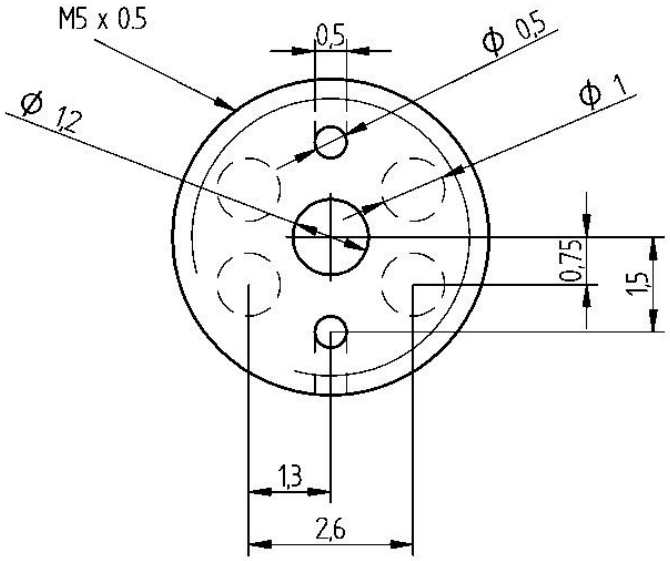

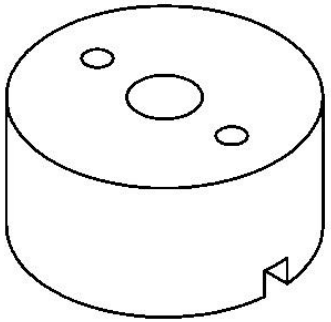

	NAME	DATE
DRAWN	W. Wang	
CHECKED		
ENG APPR		
MGR APPR		

UNLESS OTHERWISE SPECIFIED
DIMENSIONS ARE IN MILLIMETERS
ANGLES ±0.1°
DISTANCES ±0.1mm

School of Engineering
The University of Edinburgh

TITLE
Nut

SIZE A4 | Materials: BERYLCO-25 | REV

FILE NAME: nut.dft

SCALE: 10:1 | WEIGHT: | SHEET 1 OF 1

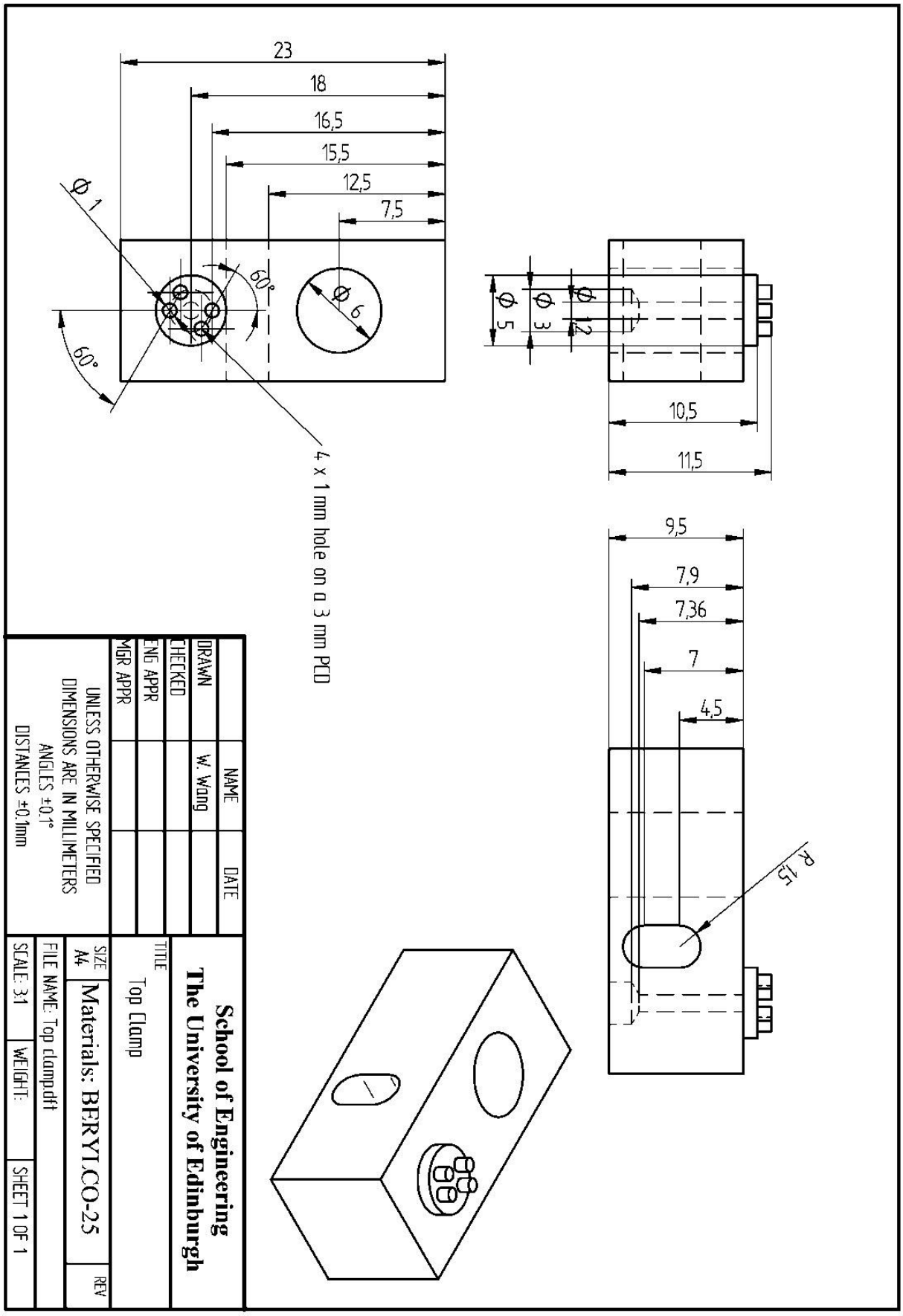
23
18
16,5
15,5
12,5
7,5
Φ 1
60°
60°
Φ 6
4 x 1 mm hole on a 3 mm PCD
Φ 5
Φ 3
Φ 1,2
10,5
11,5
9,5
7,9
7,36
7
4,5
R 15
School of Engineering
The University of Edinburgh
NAME
DATE
DRAWN
W. Wang
CHECKED
ENG APPR
MGR APPR
UNLESS OTHERWISE SPECIFIED
DIMENSIONS ARE IN MILLIMETERS
ANGLES ±0.1°
DISTANCES ±0.1mm
TITLE
Top Clamp
SIZE
A4
Materials: BERYLCO-25
REV
FILE NAME: Top clamp.dft
SCALE: 3:1
WEIGHT:
SHEET 1 OF 1

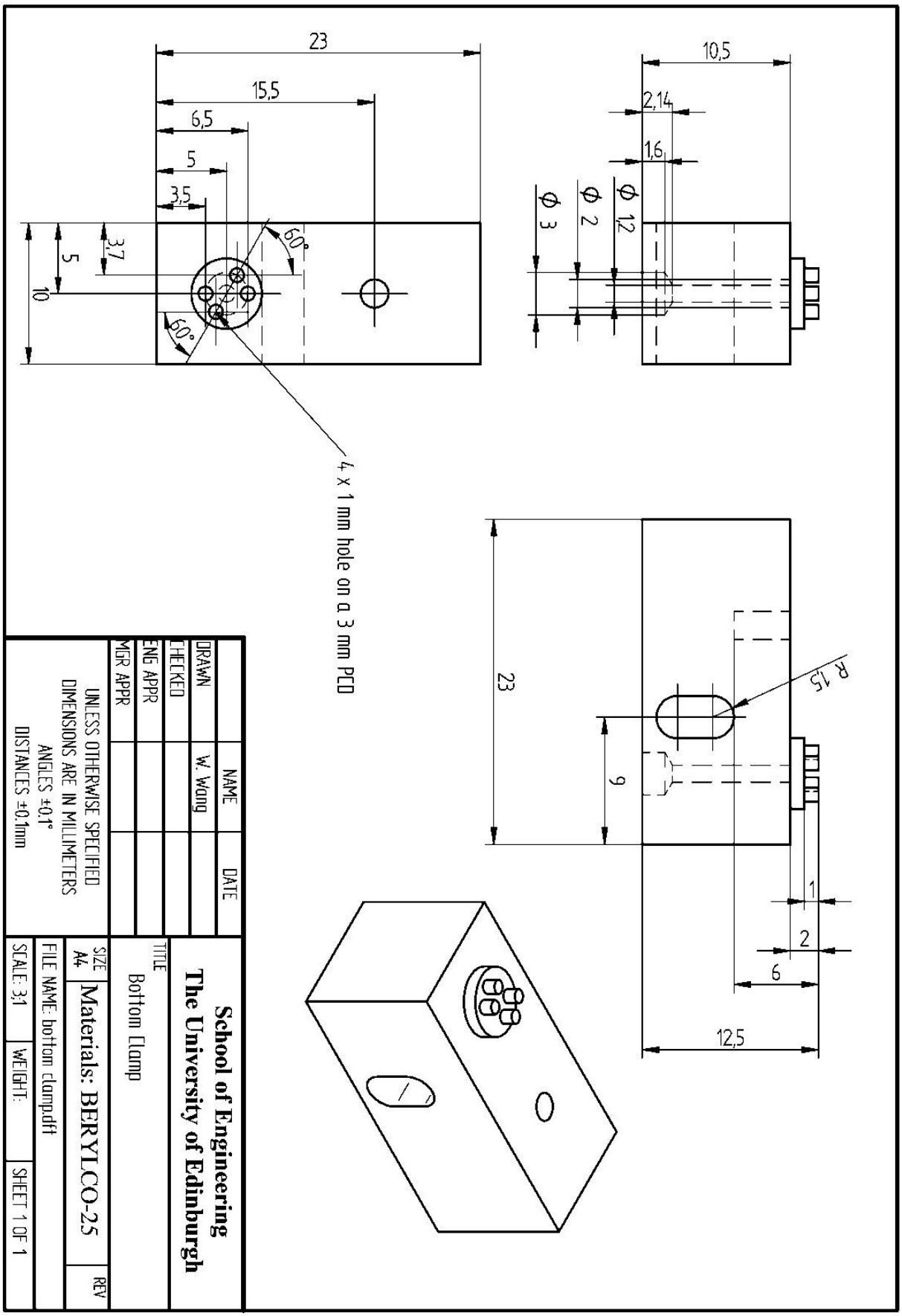
23
15,5
6,5
5
3,5
3,7
5
10
60°
60°
4 x 1 mm hole on a 3 mm PCD
10,5
2,14
1,6
ϕ 3
ϕ 2
ϕ 12
23
9
R 15
1
2
6
12,5
School of Engineering
The University of Edinburgh
NAME
DATE
DRAWN
W. Wang
CHECKED
ENG APPR
MGR APPR
UNLESS OTHERWISE SPECIFIED
DIMENSIONS ARE IN MILLIMETERS
ANGLES ±0.1°
DISTANCES ±0.1mm
TITLE
Bottom Clamp
SIZE
A4
Materials: BERYLCO-25
REV
FILE NAME: bottom clamp.dft
SCALE: 3:1
WEIGHT:
SHEET 1 OF 1

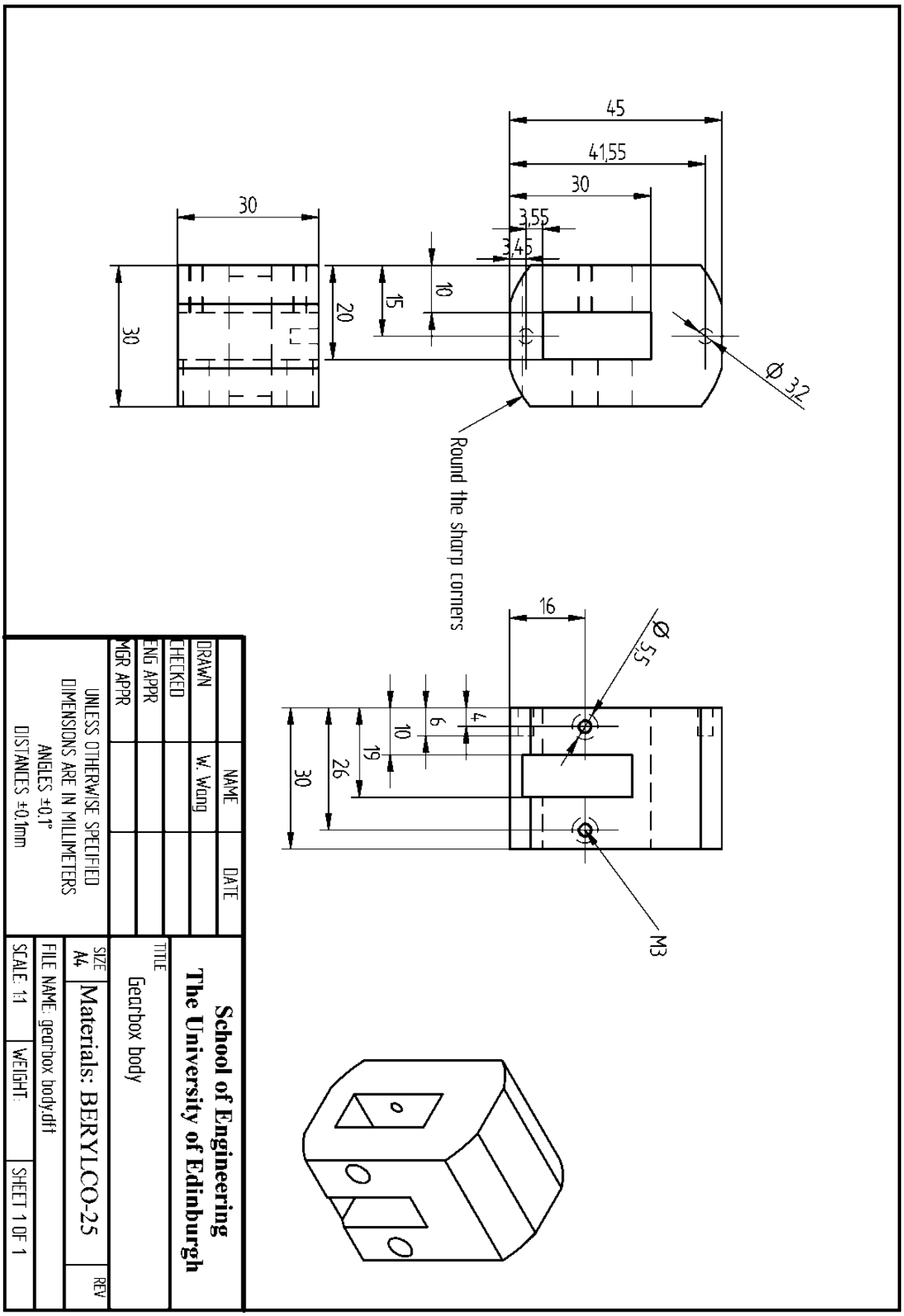
45
41,55
30
3,55
3,45
30
30
20
15
10
Ø 32
Round the sharp corners
16
Ø 5,5
4
6
10
19
26
30
M3
School of Engineering
The University of Edinburgh
DRAWN
W. Wang
CHECKED
ENG APPR
MGR APPR
NAME
DATE
UNLESS OTHERWISE SPECIFIED
DIMENSIONS ARE IN MILLIMETERS
ANGLES ±0.1°
DISTANCES ±0.1mm
TITLE
Gearbox body
SIZE
A4
Materials: BERYLCO-25
REV
FILE NAME: gearbox body.dft
SCALE: 1:1
WEIGHT:
SHEET 1 OF 1

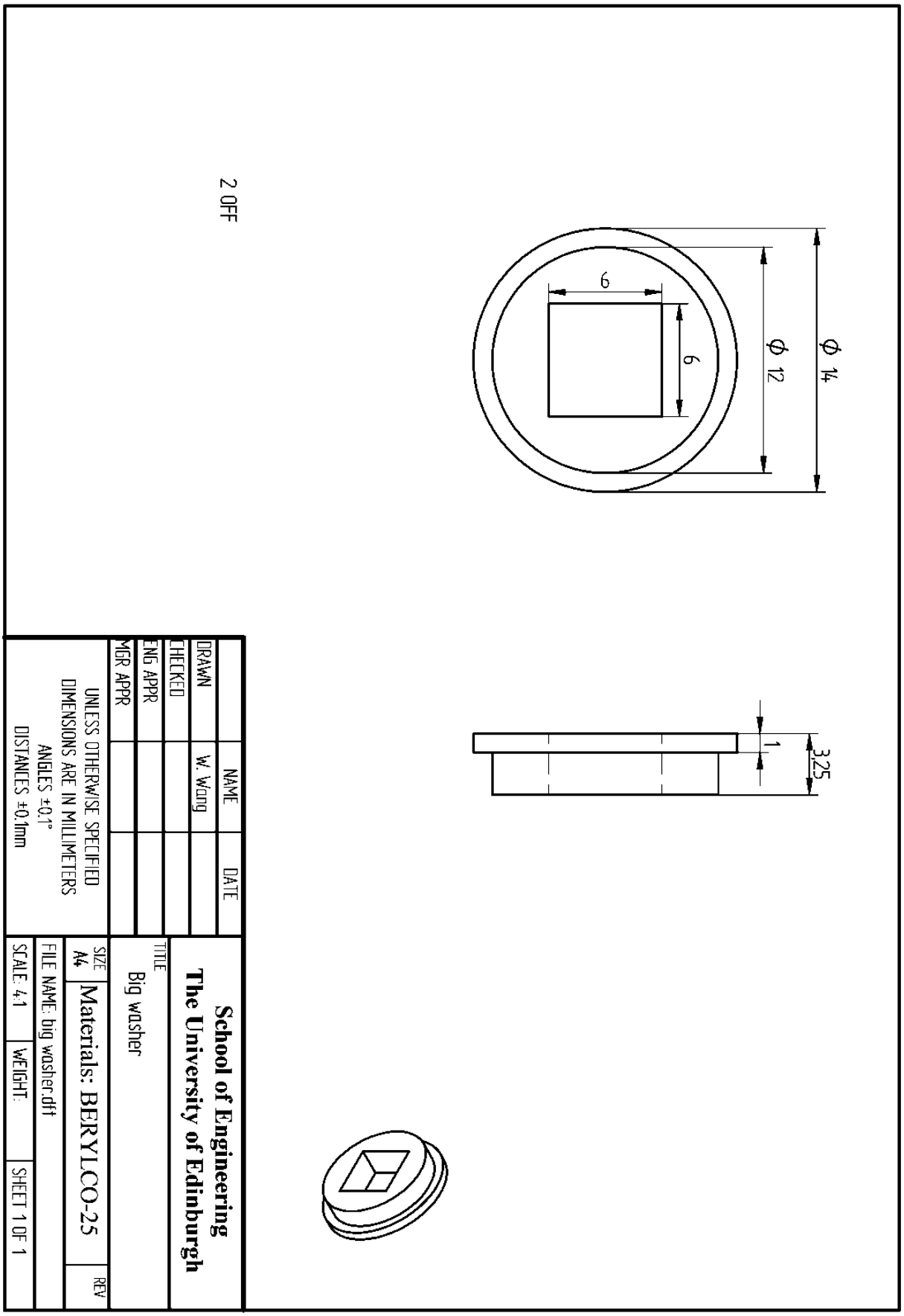
2 OFF
6
6
ϕ 12
ϕ 14
1
3.25
NAME
DATE
DRAWN
W. Wang
CHECKED
ENG APPR
MGR APPR
UNLESS OTHERWISE SPECIFIED
DIMENSIONS ARE IN MILLIMETERS
ANGLES ±0.1°
DISTANCES ±0.1mm
School of Engineering
The University of Edinburgh
TITLE
Big washer
SIZE
A4
Materials: BERYLCO-25
REV
FILE NAME: big washer.dft
SCALE: 4:1
WEIGHT:
SHEET 1 OF 1

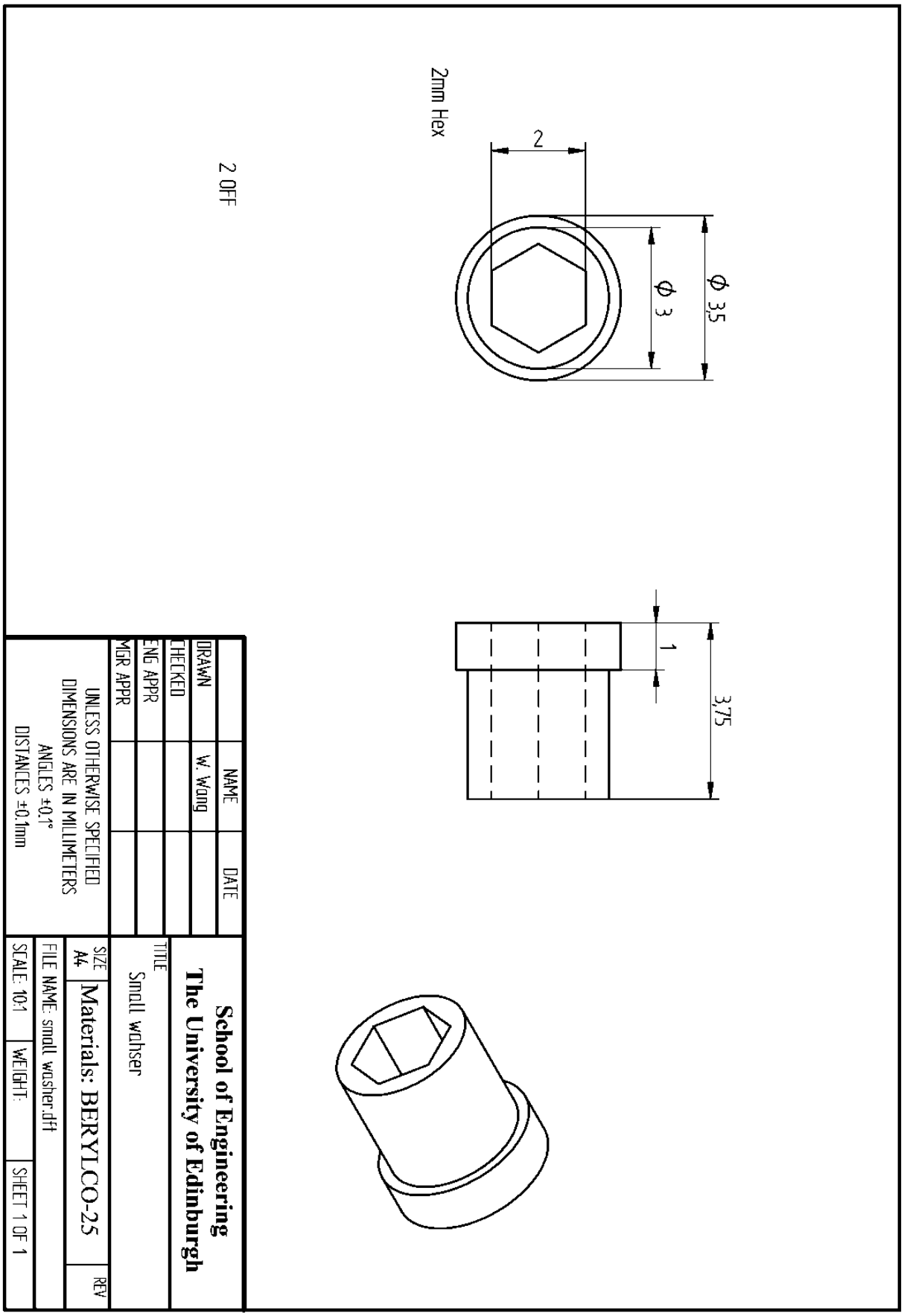
2mm Hex
2 OFF
2
ϕ 3,5
ϕ 3
1
3,75
NAME
DATE
DRAWN
W. Wong
CHECKED
ENG APPR
MGR APPR
UNLESS OTHERWISE SPECIFIED
DIMENSIONS ARE IN MILLIMETERS
ANGLES ±0.1°
DISTANCES ±0.1mm
School of Engineering
The University of Edinburgh
TITLE
Small washer
SIZE
A4
Materials: BERYLCO-25
REV
FILE NAME: small washer.dft
SCALE: 10:1
WEIGHT:
SHEET 1 OF 1

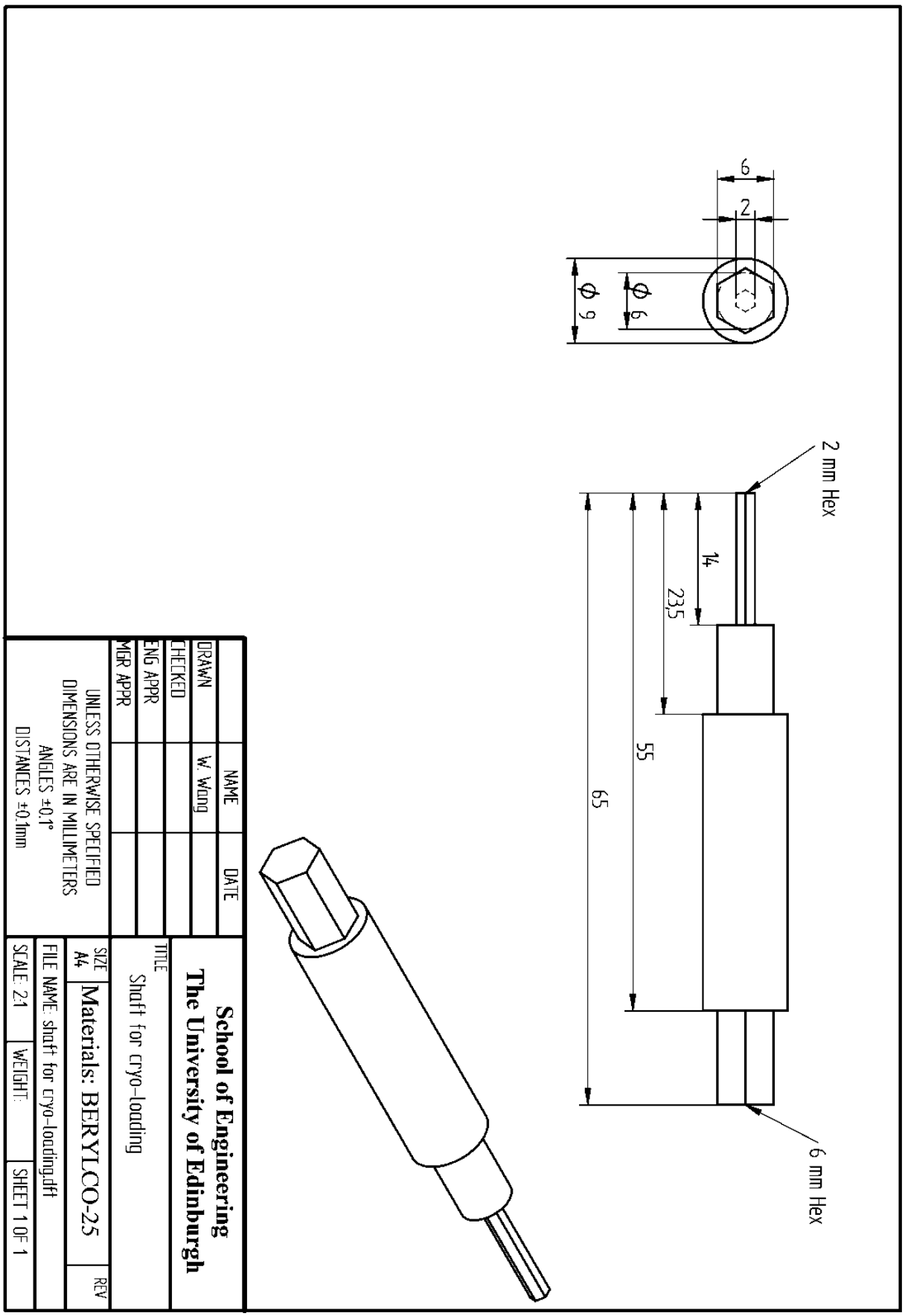

	NAME	DATE
DRAWN	W. Wang	
CHECKED		
ENG APPR		
MGR APPR		

UNLESS OTHERWISE SPECIFIED
DIMENSIONS ARE IN MILLIMETERS
ANGLES ±0.1°
DISTANCES ±0.1mm

School of Engineering
The University of Edinburgh

TITLE
Shaft for cryo-loading

SIZE A4 | **Materials: BERYLCO-25** | REV

FILE NAME: shaft for cryo-loading.dft

SCALE: 2:1 | WEIGHT: | SHEET 1 OF 1

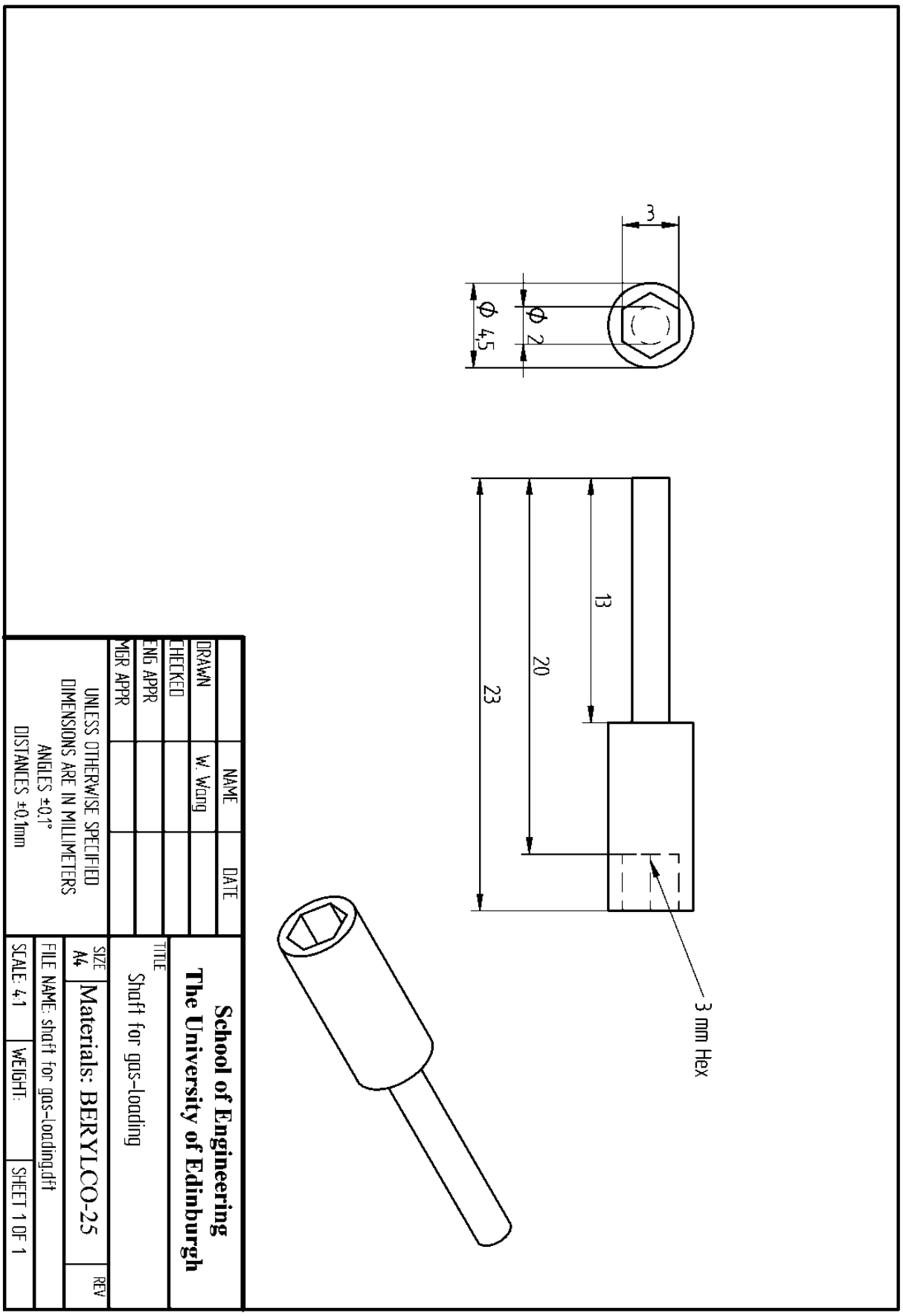

	NAME	DATE
DRAWN	W. Wang	
CHECKED		
ENG APPR		
MGR APPR		

UNLESS OTHERWISE SPECIFIED
DIMENSIONS ARE IN MILLIMETERS
ANGLES ±0.1°
DISTANCES ±0.1mm

School of Engineering
The University of Edinburgh

TITLE
Shaft for gas-loading

SIZE A4 | **Materials: BERYLCO-25** | REV

FILE NAME: shaft for gas-loading.dft

SCALE: 4:1 | WEIGHT: | SHEET 1 OF 1

A3 The high-pressure cell for INS measurement

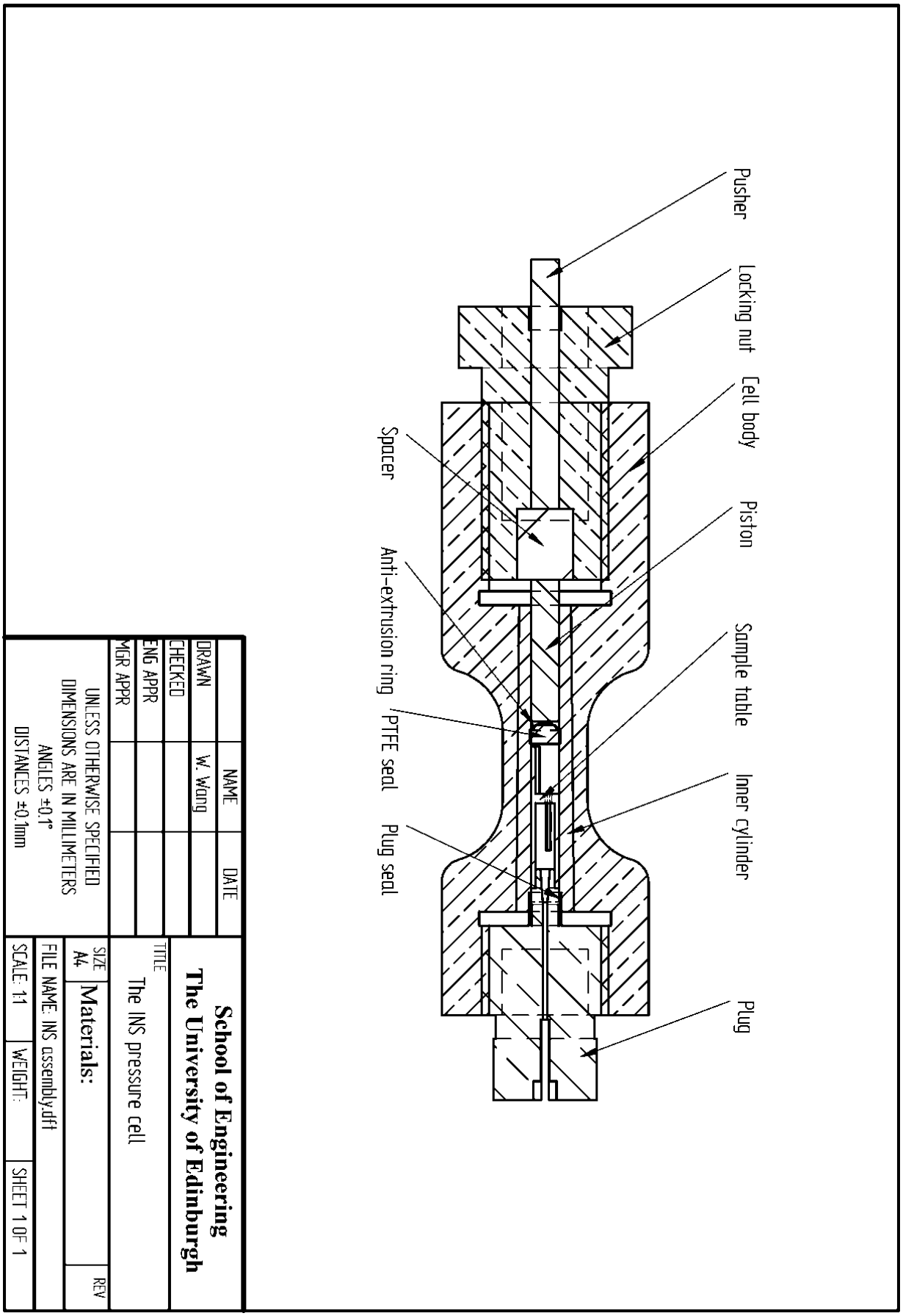
Pusher
Locking nut
Cell body
Piston
Sample table
Inner cylinder
Plug
Spacer
Anti-extrusion ring
PTFE seal
Plug seal
School of Engineering
The University of Edinburgh
NAME
DATE
DRAWN
W. Wang
CHECKED
ENG APPR
MGR APPR
UNLESS OTHERWISE SPECIFIED
DIMENSIONS ARE IN MILLIMETERS
ANGLES ±0.1°
DISTANCES ±0.1mm
TITLE
The INS pressure cell
SIZE
A4
Materials:
REV
FILE NAME: INS assembly.dft
SCALE: 1:1
WEIGHT:
SHEET 1 OF 1

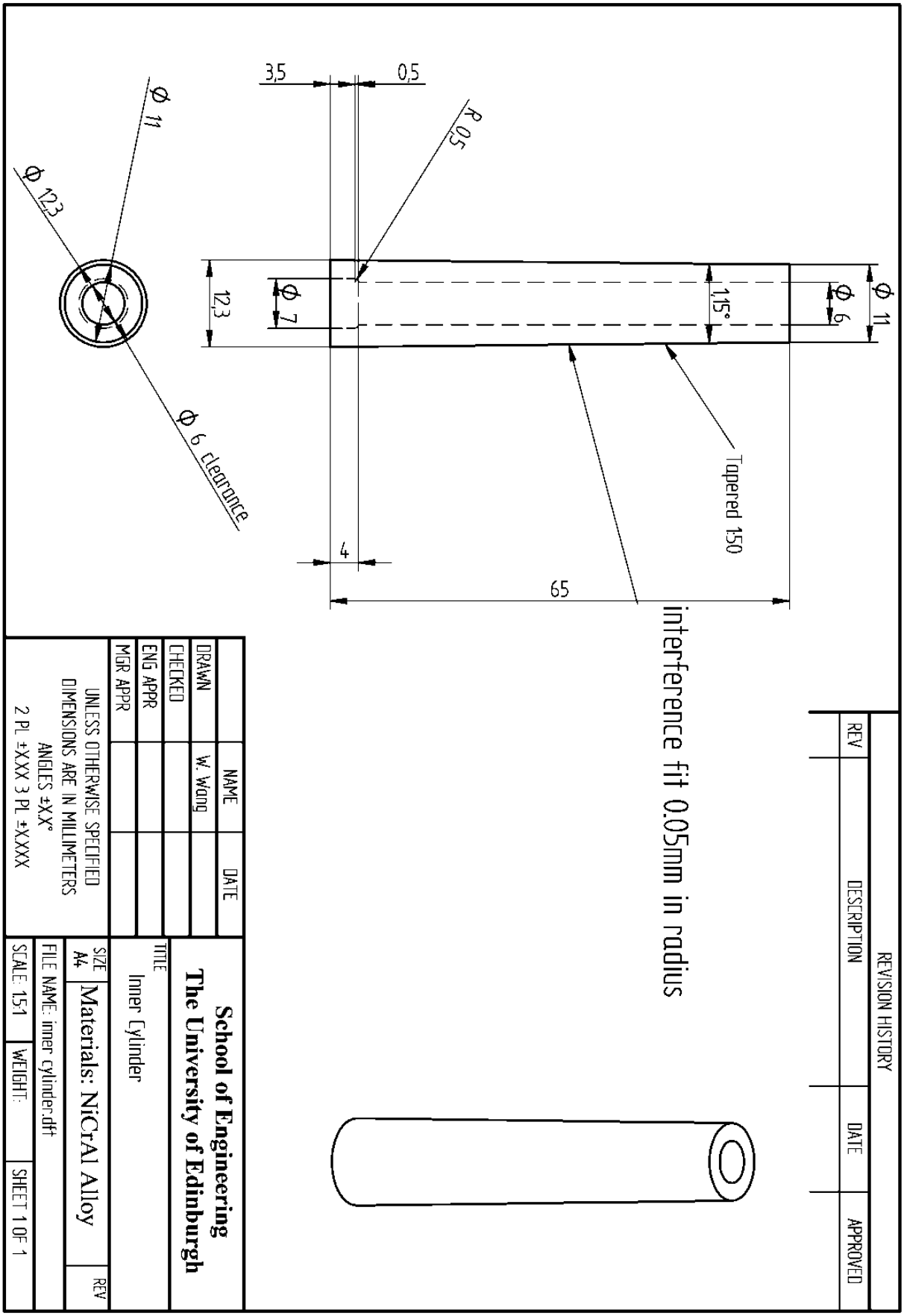
3,5
0,5
R 0,5
Ø 11
Ø 12,3
12,3
Ø 7
1,15°
Ø 6
Ø 11
Ø 6 clearance
Tapered 150
4
65
interference fit 0.05mm in radius
REVISION HISTORY
REV
DESCRIPTION
DATE
APPROVED
NAME
DATE
DRAWN
W. Wang
CHECKED
ENG APPR
MGR APPR
UNLESS OTHERWISE SPECIFIED
DIMENSIONS ARE IN MILLIMETERS
ANGLES ±X.X°
2 PL ±XXX 3 PL ±X.XXX
School of Engineering
The University of Edinburgh
TITLE
Inner Cylinder
SIZE
A4
Materials: NiCrAl Alloy
REV
FILE NAME: inner cylinder.dft
SCALE: 1:1
WEIGHT:
SHEET 1 OF 1

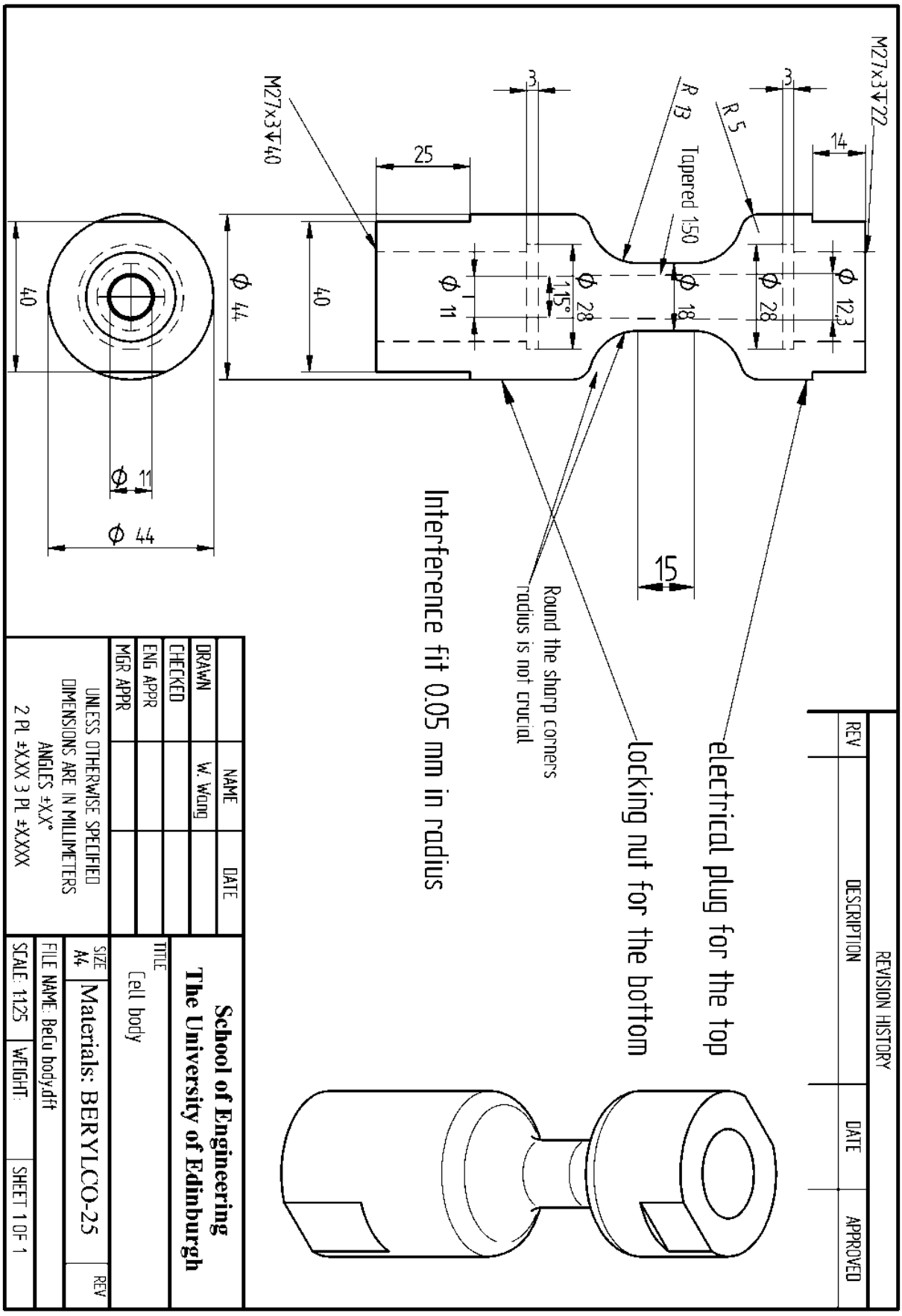
M27x3↓22
M27x3↓40
R 13
Tapered 150
R 5
14
25
3
3
Φ 12.3
Φ 28
Φ 18
Φ 28
Φ 11
115°
40
Φ 44
40
Φ 11
Φ 44
15
Round the sharp corners
radius is not crucial
Interference fit 0.05 mm in radius
electrical plug for the top
locking nut for the bottom
REVISION HISTORY
REV
DESCRIPTION
DATE
APPROVED
NAME
DATE
DRAWN
W. Wang
CHECKED
ENG APPR
MGR APPR
UNLESS OTHERWISE SPECIFIED
DIMENSIONS ARE IN MILLIMETERS
ANGLES ±X.X°
2 PL ±X.XX 3 PL ±X.XXX
School of Engineering
The University of Edinburgh
TITLE
Cell body
SIZE
A4
Materials: BERYLCO-25
REV
FILE NAME: BeCu body.dft
SCALE: 1:1.25
WEIGHT:
SHEET 1 OF 1

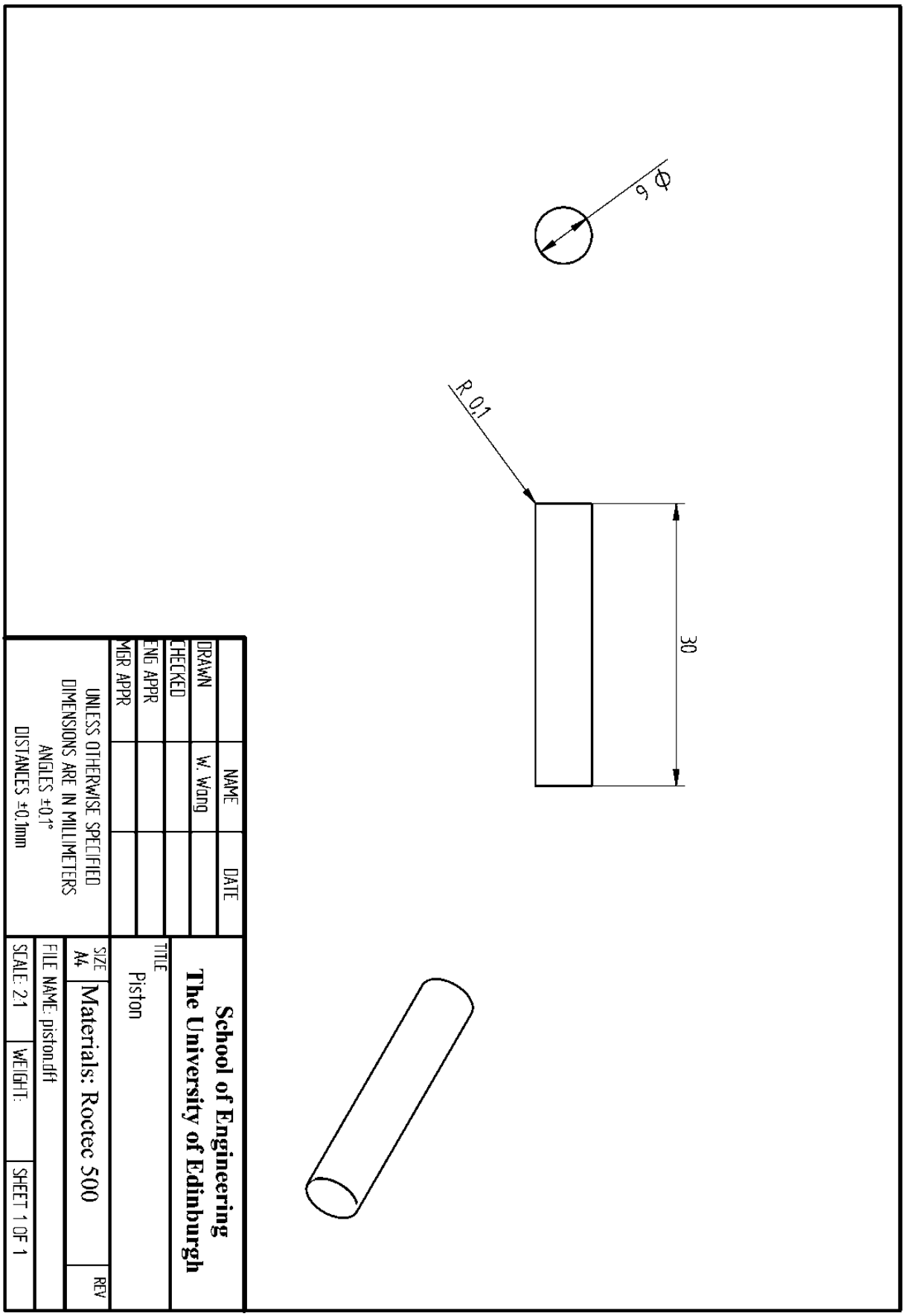
Φ 5
R 0.1
30
School of Engineering
The University of Edinburgh
NAME
DATE
DRAWN
W. Wang
CHECKED
ENG APPR
MGR APPR
UNLESS OTHERWISE SPECIFIED
DIMENSIONS ARE IN MILLIMETERS
ANGLES ±0.1°
DISTANCES ±0.1mm
TITLE
Piston
SIZE
A4
Materials: Roctec 500
REV
FILE NAME: piston.dft
SCALE: 2:1
WEIGHT:
SHEET 1 OF 1

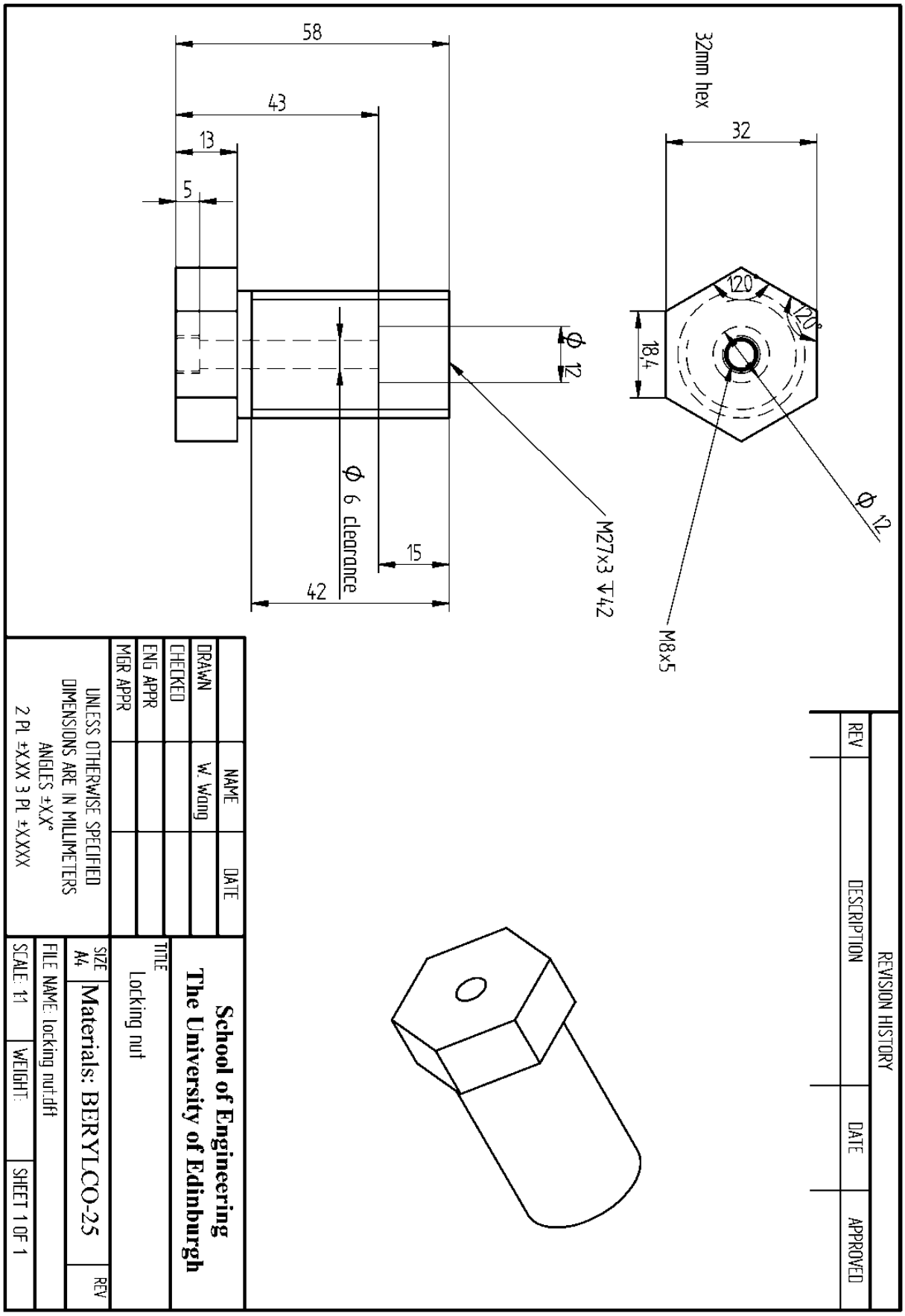
58
43
13
5
32mm hex
32
120
120°
18.4
Φ 12
Φ 6 clearance
M27x3 ↧42
15
42
M8x5
Φ 12
REVISION HISTORY
REV
DESCRIPTION
DATE
APPROVED
NAME
DATE
DRAWN
W. Wang
CHECKED
ENG APPR
MGR APPR
UNLESS OTHERWISE SPECIFIED
DIMENSIONS ARE IN MILLIMETERS
ANGLES ±X.X°
2 PL ±XXX 3 PL ±XXXX
School of Engineering
The University of Edinburgh
TITLE
Locking nut
SIZE
A4
Materials: BERYLCO-25
REV
FILE NAME: locking nut.dft
SCALE: 1:1
WEIGHT:
SHEET 1 OF 1

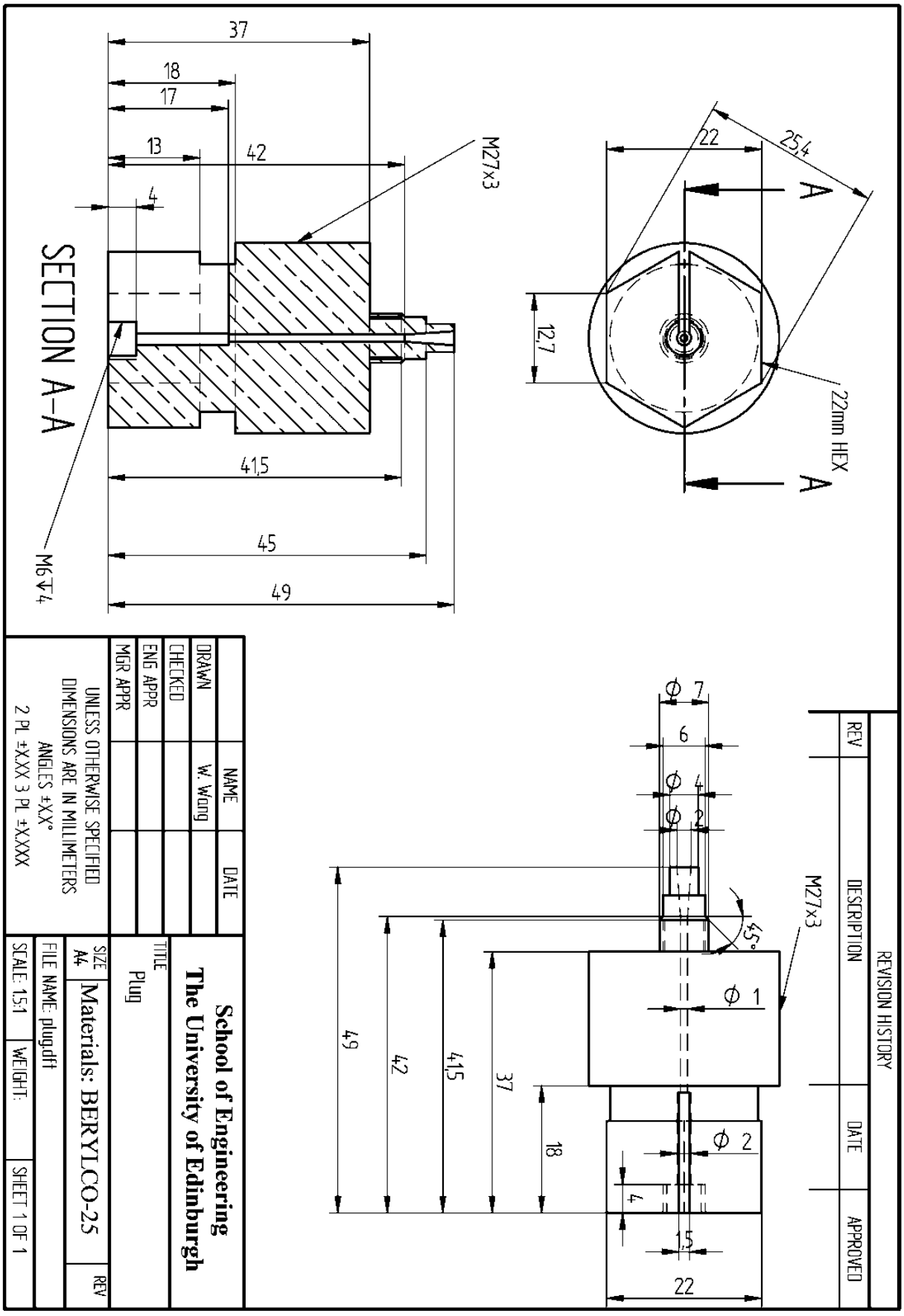
SECTION A-A
37
18
17
13
42
4
M27x3
41,5
45
49
M6 ↧4
22
25,4
12,7
22mm HEX
A
A
REVISION HISTORY
REV
DESCRIPTION
DATE
APPROVED
Ø 7
6
Ø 4
Ø 2
M27x3
45°
Ø 1
49
42
41,5
37
18
Ø 2
4
15
22
NAME
DATE
DRAWN
W. Wong
CHECKED
ENG APPR
MGR APPR
UNLESS OTHERWISE SPECIFIED
DIMENSIONS ARE IN MILLIMETERS
ANGLES ±X.X°
2 PL ±X.XX 3 PL ±X.XXX
School of Engineering
The University of Edinburgh
TITLE
Plug
SIZE
A4
Materials: BERYLCO-25
REV
FILE NAME: plug.dft
SCALE: 1:1
WEIGHT:
SHEET 1 OF 1

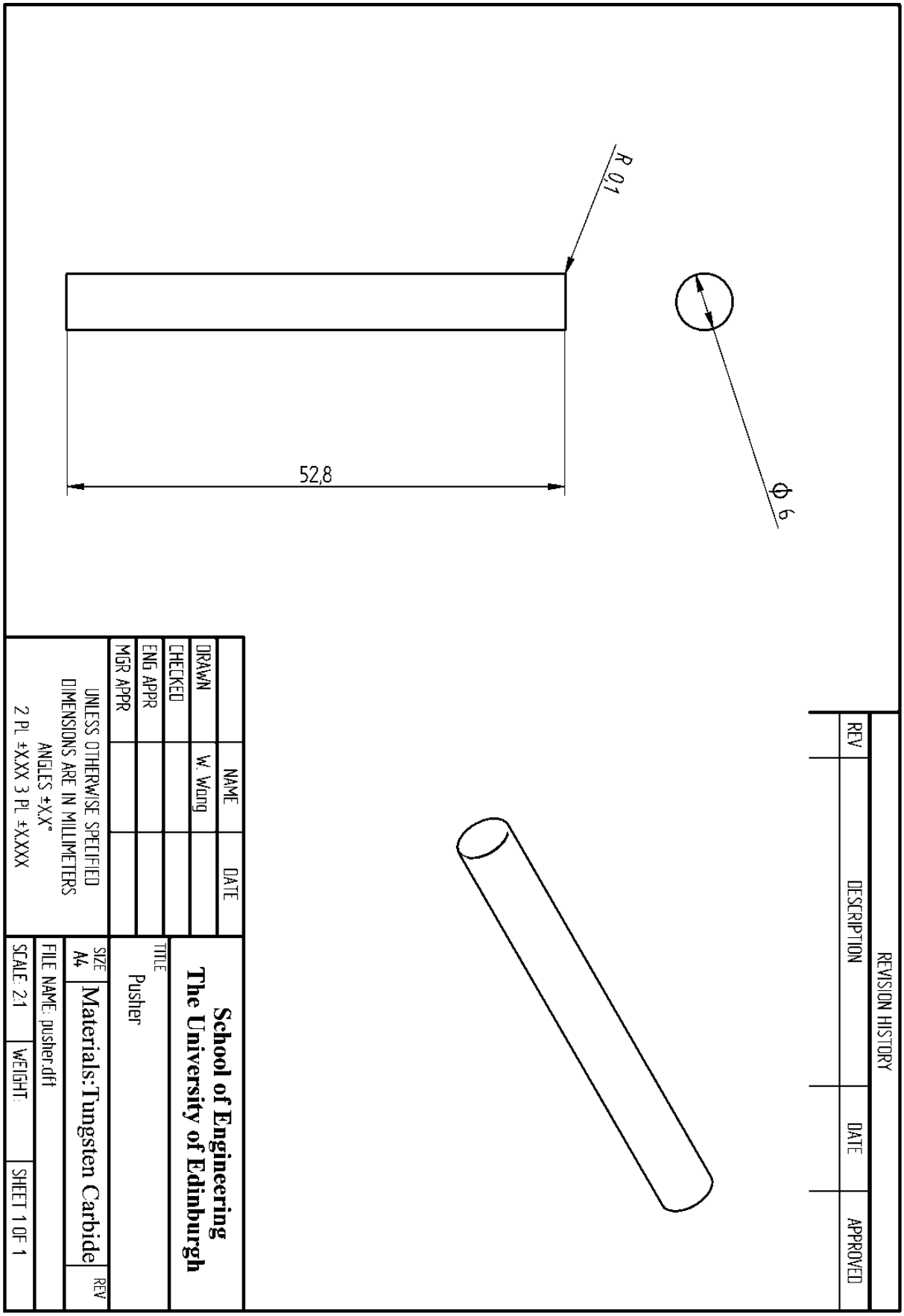
R 0.1
52.8
ϕ 6
REVISION HISTORY
REV
DESCRIPTION
DATE
APPROVED
NAME
DATE
DRAWN
W. Wang
CHECKED
ENG APPR
MGR APPR
UNLESS OTHERWISE SPECIFIED
DIMENSIONS ARE IN MILLIMETERS
ANGLES ±X.X°
2 PL ±X.XX 3 PL ±X.XXX
School of Engineering
The University of Edinburgh
TITLE
Pusher
SIZE
A4
Materials: Tungsten Carbide
REV
FILE NAME: pusher.dft
SCALE: 2:1
WEIGHT:
SHEET 1 OF 1

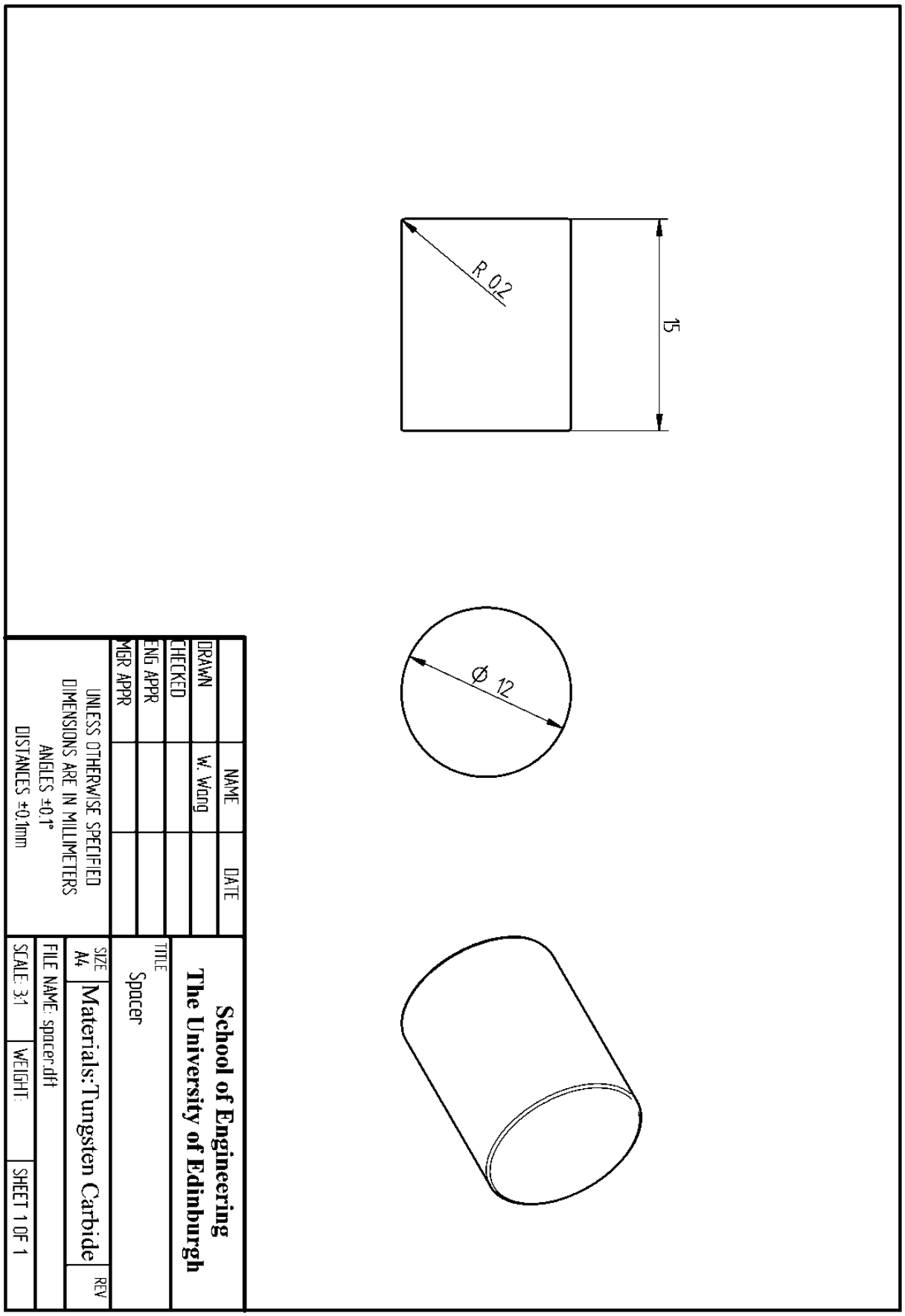
R 02
15
Ø 12
School of Engineering
The University of Edinburgh
NAME
DATE
DRAWN
W. Wang
CHECKED
ENG APPR
MGR APPR
UNLESS OTHERWISE SPECIFIED
DIMENSIONS ARE IN MILLIMETERS
ANGLES ±0.1°
DISTANCES ±0.1mm
TITLE
Spacer
SIZE
A4
Materials:Tungsten Carbide
REV
FILE NAME: spacer.dft
SCALE: 3:1
WEIGHT:
SHEET 1 OF 1

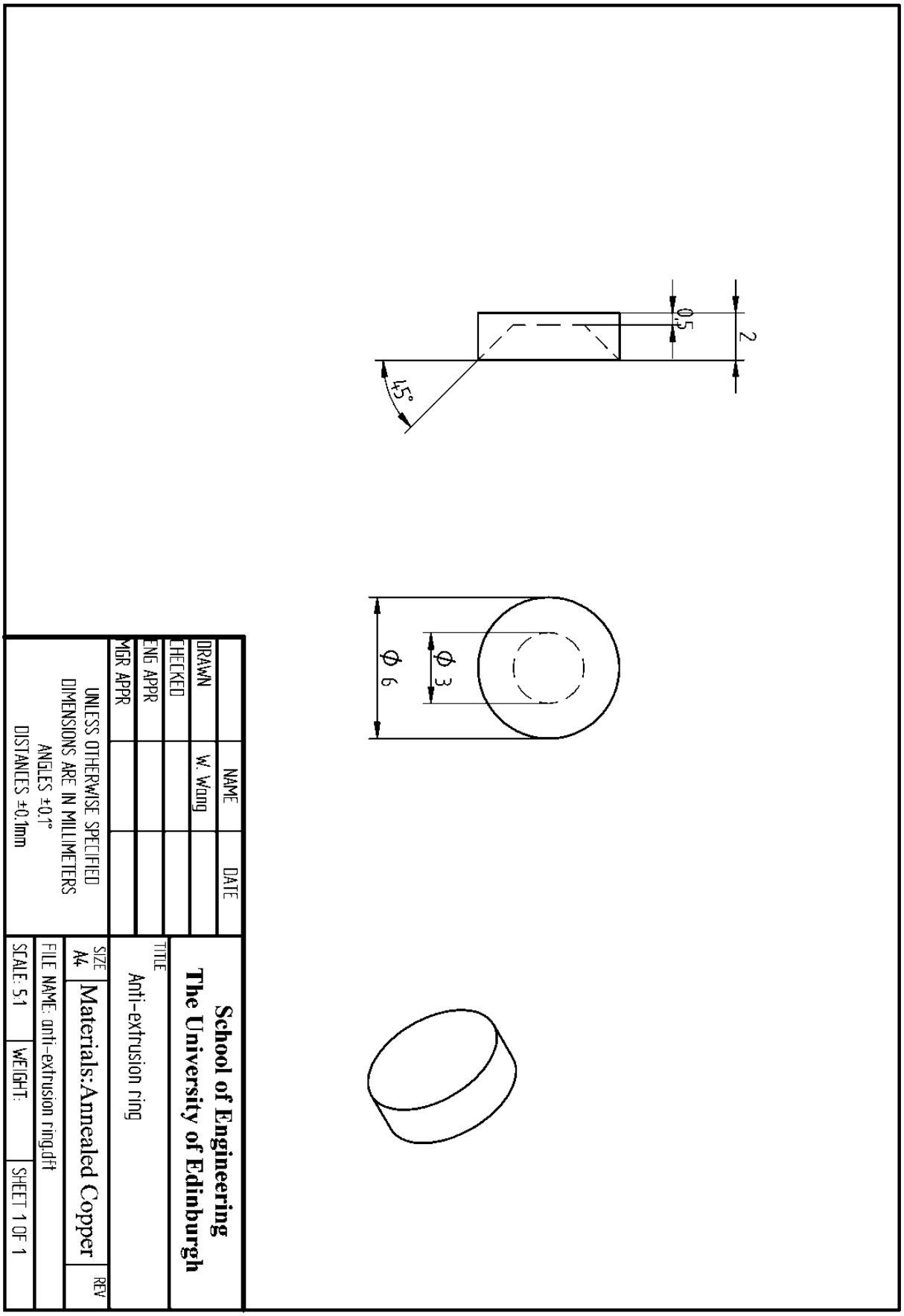
0.5
2
45°
ϕ 6
ϕ 3
School of Engineering
The University of Edinburgh
NAME
DATE
DRAWN
W. Wang
CHECKED
ENG APPR
MGR APPR
UNLESS OTHERWISE SPECIFIED
DIMENSIONS ARE IN MILLIMETERS
ANGLES ±0.1°
DISTANCES ±0.1mm
TITLE
Anti-extrusion ring
SIZE
A4
Materials:Annealed Copper
REV
FILE NAME: anti-extrusion ring.dft
SCALE: 5:1
WEIGHT:
SHEET 1 OF 1

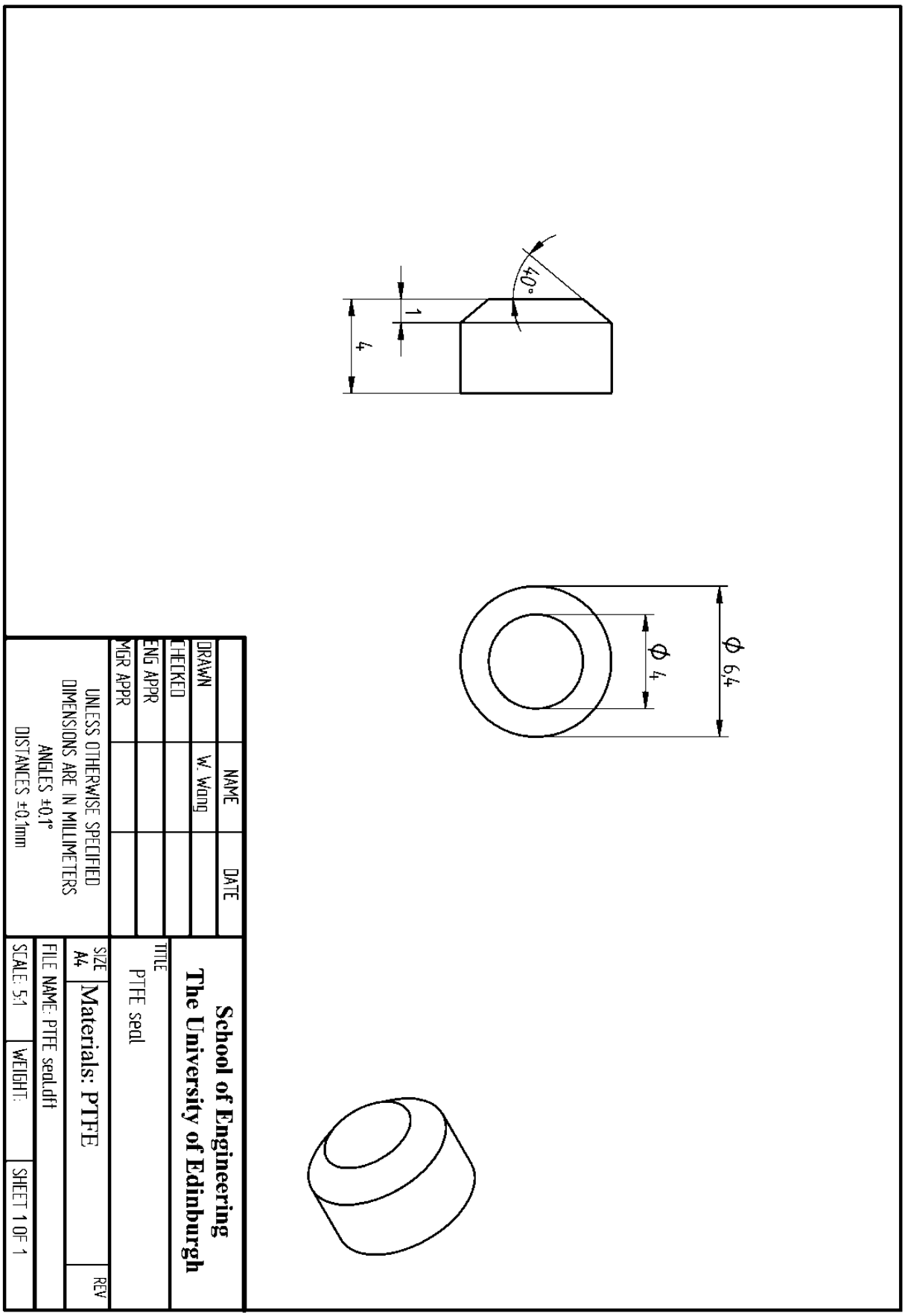
40°
1
4
ϕ 6.4
ϕ 4
NAME
DATE
DRAWN
W. Wang
CHECKED
ENG APPR
MGR APPR
UNLESS OTHERWISE SPECIFIED
DIMENSIONS ARE IN MILLIMETERS
ANGLES ±0.1°
DISTANCES ±0.1mm
School of Engineering
The University of Edinburgh
TITLE
PTFE seal
SIZE
A4
Materials: PTFE
REV
FILE NAME: PTFE seal.dft
SCALE: 5:1
WEIGHT:
SHEET 1 OF 1

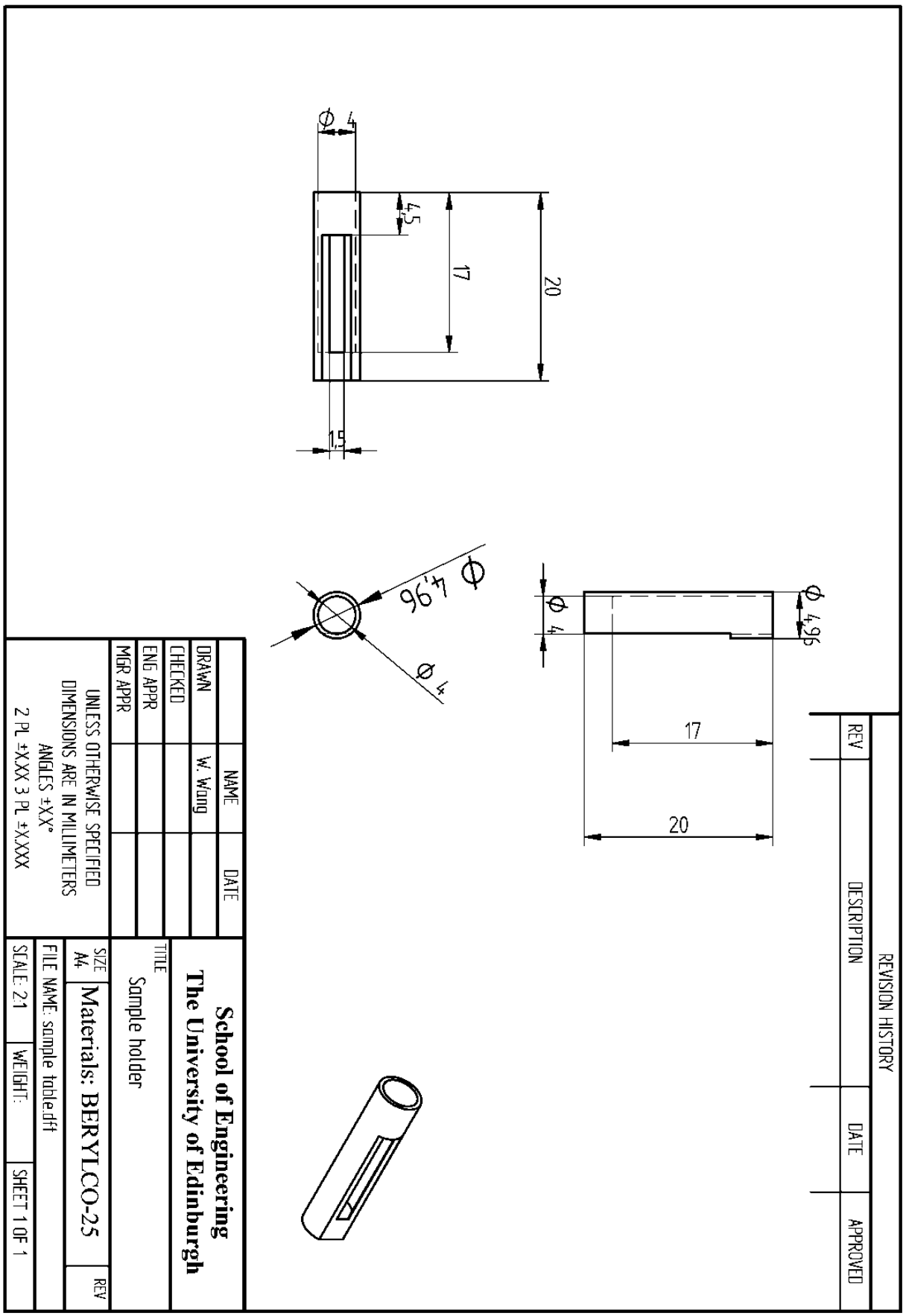
REVISION HISTORY
REV
DESCRIPTION
DATE
APPROVED
Ø 4
4,5
17
20
1,5
Ø 4,96
Ø 4
Ø 4,96
Ø 4
17
20
NAME
DATE
DRAWN
W. Wang
CHECKED
ENG APPR
MGR APPR
UNLESS OTHERWISE SPECIFIED
DIMENSIONS ARE IN MILLIMETERS
ANGLES ±XX°
2 PL ±X.XX 3 PL ±X.XXX
School of Engineering
The University of Edinburgh
TITLE
Sample holder
SIZE
A4
Materials: BERYLCO-25
REV
FILE NAME: sample table.dft
SCALE: 2:1
WEIGHT:
SHEET 1 OF 1

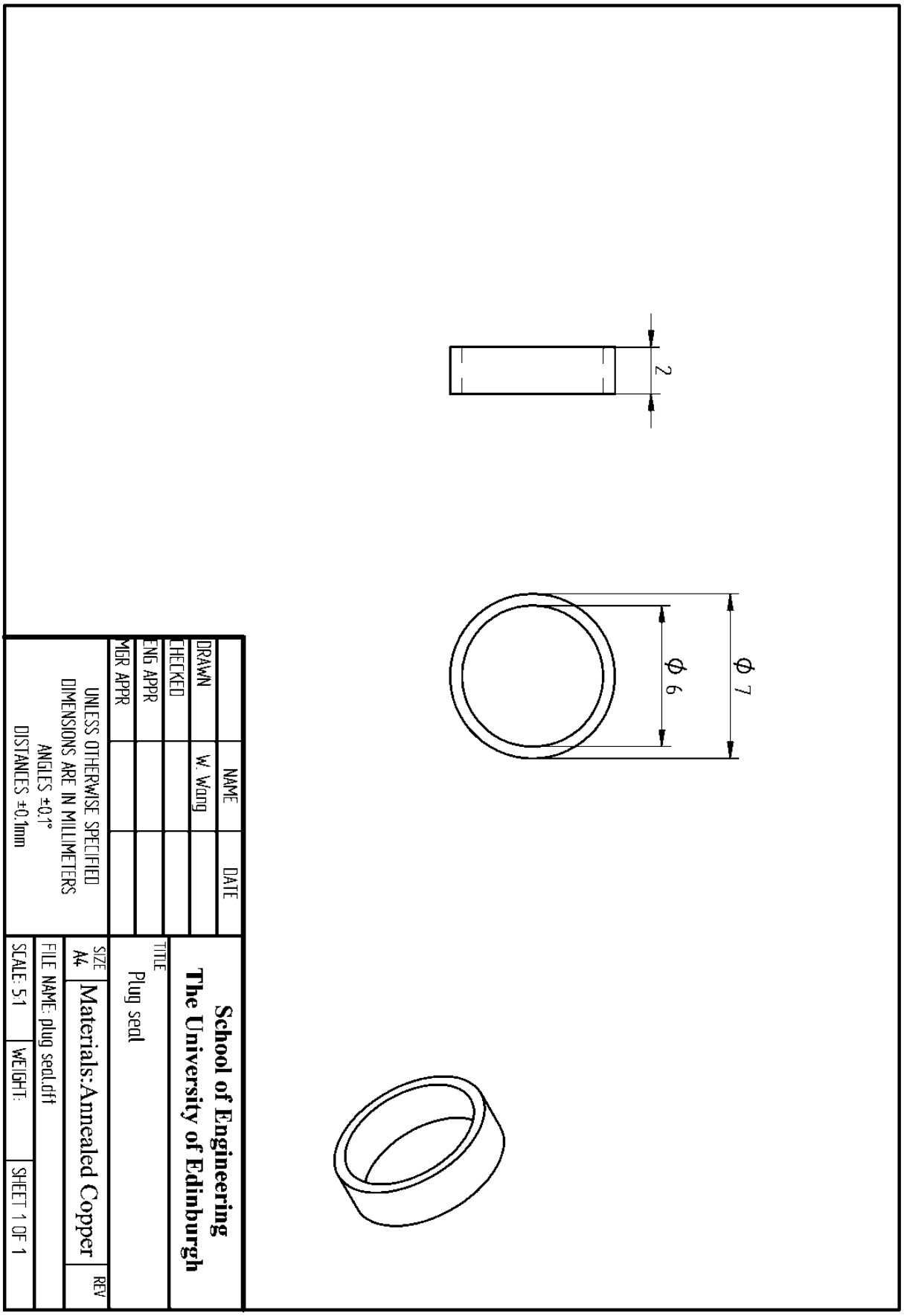
2
ϕ 7
ϕ 6
School of Engineering
The University of Edinburgh
NAME
DATE
DRAWN
W. Wang
CHECKED
ENG APPR
MGR APPR
UNLESS OTHERWISE SPECIFIED
DIMENSIONS ARE IN MILLIMETERS
ANGLES ±0.1°
DISTANCES ±0.1mm
TITLE
Plug seal
SIZE
A4
Materials:Annealed Copper
REV
FILE NAME: plug seal.dft
SCALE: 5:1
WEIGHT:
SHEET 1 OF 1

Appendix B Materials Data sheet

BERYLCO-25 Data sheet

Date:15/ 4/08

Invoice to :-
THE UNIVERSITY OF EDINBURGH
FINANCE DEPARTMENT
9-16 CHAMBERS STREET
EDINBURGH
EH1 1HT
PHONE 0131 650 5312

FULL CERTIFICATE OF CONFORMITY

Deliver to :-
PHYSI)WORKSHOP
UNIVERSITY OF EDINBURGH
JAMES CLERK MAXWELL BUILDING
THE KING'S BUILDING
EDINBURGH EH9 3JZ
PHONE

NGK BERYLCO U.K. LTD.
HOUSTON PARK, MONTFORD STREET, SALFORD, M50 2RP
Telephone: 0161-745 7162
Fax: 0161-745 7520
VAT No: 457 4017 48
Reg. No: 2085285
Email: enquiries@ngkberylco.co.uk
Website: www.ngkberylco.co.uk

NGK BERYLCO

BSI Approved
Registration No. RS 33181
ISO 9001:2000
AS 9120:2002

Metal supplied by NGK Berylco U.K. Limited complies with RoHS 2002/95/EC

Certified that the supplies detailed hereon, are covered by the source's Certificate of Conformity or Test Certificate referenced hereon and have been subject to our BS EN ISO 9001:2000/AS9120:2002 Registered Stockists - Cert. No. RS 33181 (Quality Assured products with lot traceability)
Certified that the whole of the materials and/or parts covered by this certificate have been received under cover of the relevant certificates quoted hereon, in the same condition as when received and are released in accordance with the requirements of B.Ae./AGS/QC/SC1 Part 2. (ISSUED UNDER B.Ae. APPROVAL No. [illegible])
~~BAE/AGS/2370/AERO) also meeting requirements of AMS4640B-2 (APPROVAL NO. - NAFSS/PART2/0637).~~
Certified that the whole of the supplies detailed hereon have been inspected, tested and unless stated above, conform in all respects with the requirements of the contract or order.

Del. Qty	Size Details	Description	Text
5.80 Kgs	40.00mm	BERYLCO 25 / C17200 (F.H.T. = RC 36/42) BAR	
		101.6mm Diameter x 40.00mm Thick (2 off)	
Batch :	NP174952 Cast :	A62870 Cert :	A3455-5247
Subcontract:	502706-A Hardness test:	HV Value:	402.00 Be. content : 1.820

Beryllium	Cobalt	Nickel	Iron	Silicon	Aluminium	Copper
1.820%	0.241%	0.009%	0.030%	0.015%	0.030%	97.855%

Tensile Str.	Yield	Elongation %	Hardness Type	Result
1241.00 Mpa	1110.00 Mpa	3.00	HV	402.00

Sales Order No :- Customer Reference :-
D3736 EE 14943
150494 OUR C43606

Signed :- 15-4-08

Serial Number:0322183

NiCrAl alloy Data sheet